DISSERTATION

OBSERVATIONS OF AEROSOL PARTICLES AND DEEP CONVECTIVE UPDRAFTS AND THE MODELING OF THEIR INTERACTIONS

Submitted by

Peter James Marinescu

Department of Atmospheric Science

In partial fulfillment of the requirements

For the Degree of Doctor of Philosophy

Colorado State University

Fort Collins, Colorado

Spring 2020

Doctoral Committee:

Advisor: Susan C. van den Heever
Co-Advisor: Sonia M. Kreidenweis

Michael M. Bell
Richard Eykholt

ABSTRACT

OBSERVATIONS OF AEROSOL PARTICLES AND DEEP CONVECTIVE UPDRAFTS AND THE MODELING OF THEIR INTERACTIONS

Within cloud updrafts, cloud droplets form on aerosol particles that serve as cloud condensation nuclei (CCN). Varying the concentrations of CCN alters the concentrations of cloud droplets, which in turn modifies subsequent microphysical processes within clouds. In this dissertation, both observational and modeling studies are presented that reduce the uncertainties associated with these aerosol-induced feedback processes in deep convective clouds.

In the first study, five years of observations of aerosol particle size distributions from central Oklahoma are compared, and useful metrics are provided for implementing aerosol size distributions into models. Using these unique, long-term observations, power spectra analyses are also completed to determine the most relevant cycles (from hours to weeks) for different aerosol particle sizes. Diurnal cycles produce the strongest signals in every season, most consistently in the accumulation mode and the smallest (diameters < 30 nm) particles. The latter result suggests that these smallest particles may play a more important role in the CCN budget than previously thought. Ultimately, in understanding which, when and why different aerosol particles are present in the atmosphere, we can better assess the impacts that they have on clouds.

The types and number of aerosol particles that can serve as CCN depend on the amount of supersaturation, and thus the magnitude of the cloud updraft vertical velocities. However, in situ updraft observations in deep convective clouds are scarce, and other vertical velocity estimates often have uncertainties that are difficult to characterize. In the next study, novel, in

situ observations of deep convective updraft vertical velocities from targeted radiosonde launches during the CSU Convective Cloud Outflows and Updrafts Experiment (C^3LOUD-Ex) are presented. Vertical velocities of over 50 m s^{-1} are estimated from radiosonde observations taken in Colorado. Radar data are used to contextualize the radiosonde measurements and to provide an independent estimate of the updraft magnitudes for comparison. These observations are valuable in that they: 1) contribute novel estimates of the vertical velocities within deep convective clouds, 2) demonstrate that in situ observations of vertical velocities complement estimates from other platforms and 3) will allow for better assessments of the supersaturation magnitudes, and thus the amount of CCN that are present within deep convective clouds.

While the first two studies focus on observing aerosol particles and updrafts separately, the third study within this dissertation presents simulations of their interactions from an international model intercomparison project. Seven models from different institutions simulated the same case study of isolated deep convective clouds with both high and low CCN concentrations. The range of the responses in updrafts to varying CCN concentrations are calculated for this model suite. Despite the various physical parameterizations that these models utilize, all the models simulate stronger updrafts in the High-CCN simulations from near cloud base through ~8 km AGL, with diverging results above this altitude. The vertical velocity tendency equation is analyzed to explain which processes are causing the consistent and inconsistent updraft responses to varying CCN concentrations amongst the models.

The three studies in this dissertation each reduce the uncertainties related to aerosol effects on deep convective cloud updrafts. This work also assisted in motivating the DOE Tracking Aerosol Convection Interactions Experiment (TRACER), which will further connect observational and modeling research to reduce the uncertainties in aerosol-cloud interactions.

ACKNOWLEDGEMENTS

My procurement of a Ph. D. in atmospheric science has been both trying and rewarding, and I am grateful for all those individuals who played a role in my journey. First and foremost, I thank my advisors, Dr. Susan van den Heever and Dr. Sonia Kreidenweis, for accepting me into the CSU graduate program, challenging me and providing me with support, advice and countless opportunities to learn. I would also like to thank the other members of my Ph. D. committee, Dr. Michael Bell and Dr. Richard Eykholt, for their time and thoughts on my research.

Throughout my graduate degree, I have had the opportunity to work on a variety of topics and with many collaborators. While my M. S. research primarily utilized atmospheric models, during my Ph. D. I have had several opportunities to venture into the world of observations, and I am thankful for those who assisted me with that transition, including Dr. Don Collins, Dr. Sonia Kreidenweis, Dr. Ezra Levin, Dr. Pat Kennedy, Dr. Michael Bell, Dr. Susan van den Heever, Dr. Leah Grant, Sean Freeman and Aryeh Drager. Your patience, instruction and enthusiasm has been extremely helpful and motivating. One of these opportunities was serving as the Operations Manager for the C^3LOUD-Ex field campaign. Through this role, I learned about managing a field campaign and the challenges associated with observational platforms, and I thank the entire C^3LOUD-Ex science team for their tremendous efforts and persistent high spirits. I would also like to thank Dr. Susan van den Heever for involving me in the Aerosol-Cloud-Precipitation-Climate (ACPC) working group. Through this international collaboration, I have had the opportunity to meet with and learn from incredible scientists and students. I am grateful for all the interactions that I have had at the ACPC meetings, particularly with those individuals who stimulated engaging discussions and made that working group a worthwhile enterprise.

The CSU Department of Atmospheric Science has been a welcoming and enriching community to be a part of, with many opportunities to develop as a student, researcher, teacher, mentor, colleague, manager and friend. Therefore, I thank the faculty, students and staff that I have interacted with at CSU. In particular, I acknowledge Dr. Susan van den Heever for providing me with several opportunities to be a teaching assistant. These roles have confirmed my passion for teaching and advanced my understanding of cloud processes.

My graduate education in atmospheric science would have never happened without the support of my family and friends and the individuals who first opened their doors to an ex-investment-banker looking for a more rewarding career. Specifically, I thank, Dr. Brian Colle, Dr. Chandra Venkatachalam, Dr. Pat Kennedy and Dr. Joseph Hardin for giving me my first chance to learn about atmospheric science research. However, without the support of my family and friends, this journey would not have been possible. I am most grateful for my partner in life, Leah, for your patience, kindness, laughter, and all of our times together that have made this adventure so much more enjoyable. I would also like to thank my family and friends for their unwavering support.

My research could not have been completed without the support from several funding agencies and fellowships. I acknowledge the National Science Foundation (NSF) Graduate Fellowship Program (Grant No. DGE-1840343), the CSU Monfort Excellence Fund, NSF Grant No. AGS-1409686, and NASA Grant No. 80NSSC18K0149 that in part supported me throughout the Ph. D. program. These programs are essential for the education of future scientists, and I am grateful for the work and people that uphold these programs.

TABLE OF CONTENTS

ABSTRACT ii

ACKNOWLEDGEMENTS iv

Chapter 1 : Introduction 1

1.1 Aerosol particles and their roles in clouds 1

1.2 Interactions between CCN and deep convective clouds 4

1.3 Dissertation outline: motivation and science questions 7

Chapter 2 : Quantifying Aerosol Size Distributions and Their Temporal Variability in the Southern Great Plains, USA 10

2.1 Introduction 10

2.2 Data 12

2.3 Seasonal variations in aerosol concentrations 14

2.4 Sub-seasonal cycles within aerosol number concentrations 23

a. Methods 23

b. Hourly-to-daily cycles of aerosol number concentrations 25

c. Daily-to-weekly aerosol cycles 39

2.5 Conclusions 42

Chapter 3 : Updraft Vertical Velocity Observations and Uncertainties in High Plains Supercells Using Radiosondes and Radars 45

3.1 Introduction 45

3.2 C^3LOUD-Ex observations 48

a. Radiosondes 48

b. Radars 51
3.3 C^{3}LOUD-Ex cases 54
a. 26 May 2017 case study 54
b. 17 July 2016 case study 56
3.4 Radiosonde-derived updraft vertical velocities (w_{air}) 57
a. 2017 case 60
b. 2016 case 65
3.5 Comparisons of radiosonde w_{air} to other platforms 69
a. Comparisons with dual-Doppler estimates 69
b. Comparisons with simple parcel theory 72
3.6 Implications for future in situ observations of w_{air} within storms 73
3.7 Conclusions 75
Chapter 4 : The Impacts of Varying Concentrations of Cloud Condensation Nuclei On Deep Convective Cloud Updrafts – A Multimodel Assessment 78
4.1 Introduction 78
4.2 ACPC Model Intercomparison Project (MIP) 83
a. Case study simulations 83
b. Aerosol initialization 85
c. Models 86
4.3 CCN effects on the deep convective updrafts 92
a. Frequency 92
b. Intensity 94
4.4 Vertical velocity tendency equation and terms 97

a. Thermal buoyancy (B_{TH}) 100
b. Water vapor buoyancy (B_{WV}) 101
c. Condensate loading buoyancy (B_{CL}) 104
d. Vertical perturbation pressure gradient (VPPG) 108
e. Advection terms 111
4.5 Conclusions 114
Chapter 5 : Dissertation Conclusions 117
5.1 Summary of studies 117
5.2 Implications of this research and future work 121
References 126
Appendix 1: Merged Aerosol Size Distributions 146
Appendix 2: Analysis of the Uncertainties Associated with Drag Forces on the C^3LOUD-Ex Updraft Estimates 154
Appendix 3: ACPC MIP Model Details 156
Appendix 4: ACPC MIP Base State Calculations 159

CHAPTER 1: INTRODUCTION

1.1 Aerosol particles and their roles in clouds

Aerosols are solid or liquid particles suspended in the atmosphere. Their sizes range from on the order of nanometers (e.g., newly formed particles from combustion or photochemical processes) to the order of millimeters (e.g., windborne dust). An example of an aerosol size distribution is shown in Figure 1.1. These data were obtained from the United States Department of Energy's Atmospheric Radiation Measurement's Southern Great Plains (SGP) site and are representative of a rural, North American, continental location. Generally, there are higher number concentrations of the smaller particles (diameters < 100 nm) and relatively few large particles (diameters > 1 micron). However, these larger particles play a more substantial role in

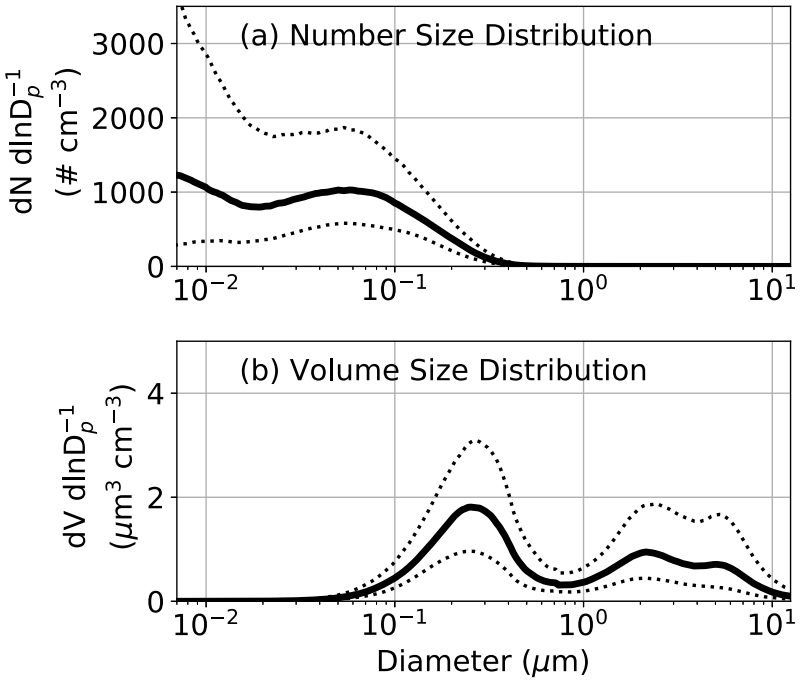

Figure 1.1. An example of the typical aerosol (a) number size distribution and (b) volume size distribution from the SGP site for springtime months (March, April and May). Data shown are the median value (solid) and the 25th and 75th percentiles (dotted) from the 5-year period between 2009 – 2013. Data from Marinescu et al. (2019).

terms of their volume and mass (Figure 1.1b). Aerosol particles also have varying composition, depending on their sources and any chemical reactions they undergo in the atmosphere.

An aerosol particle's impact on a cloud depends on both its composition and size. One way that aerosol particles interact with clouds is via radiation processes. For example, aerosol particles that are composed of black carbon or mineral dust absorb solar radiation effectively and therefore warm the atmosphere around them. If these aerosol particles are within clouds, their induced warming could lead to the evaporation, sublimation or melting of hydrometeors or change the thermodynamic stability within clouds (e.g., semi-direct aerosol effects; Hansen et al. 1997). Outside of clouds, high concentrations of radiatively-active aerosol particles can also alter the atmospheric temperature profile, change the atmospheric stability and impact cloud development. For example, large layers of biomass burning aerosol particles from central American fires are often advected into the southern United States (e.g., Rogers and Bowman 2001; Gebhart et al. 2001). Utilizing cloud-resolving model simulations, Saide et al. (2016) found that these biomass burning aerosol particles can change the thermodynamic environment prior to severe weather outbreaks, making them more or less conducive for the formation of tornadoes for different case studies. Grant and van den Heever (2014) also demonstrated that increased concentrations of aerosol particles reduce the shortwave radiation reaching the surface and in turn decrease boundary layer instability, moisture and convergence. These impacts result in weaker convective clouds in their tropical sea breeze simulations.

Aerosol particles also act as the primary formation nuclei for cloud droplets and ice crystals. Indeed, without aerosol particles on Earth, there would be no clouds resembling those that are currently observed. In the atmosphere, the air can become supersaturated with respect to liquid water. In these situations, aerosol particles lower the thermodynamic energy barriers for

the formation of cloud droplets to surpassable levels (Köhler 1936). Aerosol particles that act in this way and on which cloud droplets form are termed cloud condensation nuclei (CCN). An aerosol particle's ability to serve as a CCN depends on both its size and its hygroscopicity, the latter of which depends on its composition. Figure 1.2 shows the atmospheric supersaturation needed to form a cloud droplet for varying aerosol particle sizes and hygroscopicity, based on κ-Köhler theory (Petters and Kreidenweis, 2007). Larger particles and more hygroscopic particles require lower supersaturations to form cloud droplets. Clouds with relatively weak updrafts (e.g., less than 1 m s^{-1}) typically have peak supersaturations near cloud base that are less than 0.5%, while deep convective clouds that have stronger updrafts attain higher maximum supersaturations (e.g., Reutter et al. 2009), although it is unclear how large supersaturations can become due to the inability to observe or estimate supersaturations throughout deep convective clouds. As such, aerosol particles that act as CCN in a deep convective cloud may not act as CCN in a shallow cloud. Similar to their roles in the formation of cloud droplets, aerosol particles can also serve as ice nucleating particles (INPs), making it easier to form ice crystals in the atmosphere at modest supercoolings via a number of mechanisms (Vali 1996). However,

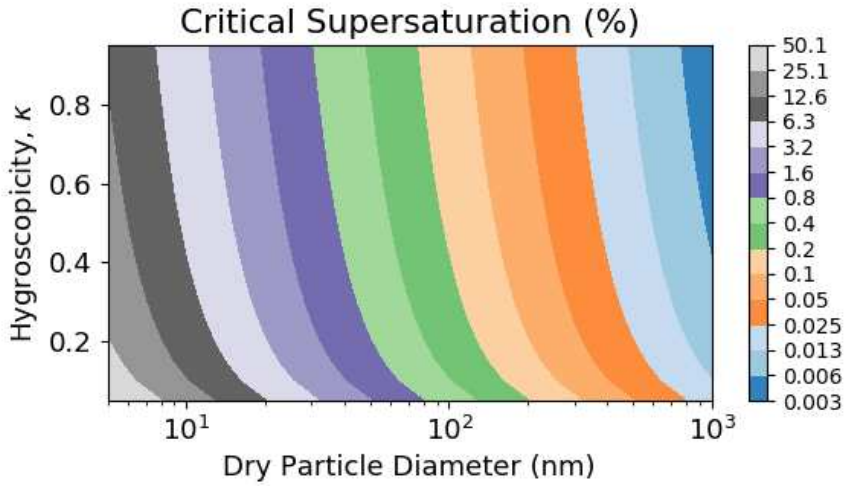

Figure 1.2. Critical supersaturations (shaded) required for aerosol particles for specified diameters (abscissa) and hygroscopicity parameters (κ, ordinate), based on κ-Köhler theory (Petters and Kreidenweis 2007).

many questions about the types of particles that can efficiently serve as INPs and the relative contributions of the different ice nucleation mechanisms remain unanswered. The impacts of aerosol particles on clouds via these nucleation pathways are also known as aerosol indirect effects.

The multiple roles played by aerosol particles make it important to understand the temporal and spatial variability of aerosol particles and their subsequent impacts on clouds. In other words, when clouds are exposed to higher concentrations of aerosol particles, how do the clouds respond? One of the first concepts towards answering this question was developed by Twomey (1974, 1977), who suggested that when holding liquid water content fixed, clouds that are exposed to higher number concentrations of CCN have higher number concentrations of smaller cloud droplets, which increases the brightness or albedo of the cloud. Albrecht (1989) took this concept even further by proposing that these clouds, which were exposed to high concentrations of CCN and have higher concentrations of small cloud droplets, are less effective at forming precipitation-sized hydrometeors and therefore, have longer lifetimes. Since these landmark studies, researchers have been attempting to better quantify these aerosol-cloud interactions. One key finding over the past decade is that magnitude and sign of the cloud response to increased concentrations of CCN varies depending on the cloud type (e.g., Seifert and Beheng 2006b; Khain et al. 2008; van den Heever et al. 2011). In this dissertation, the primary focus will be on CCN indirect effects on deep convective clouds.

1.2 Interactions between CCN and deep convective clouds

Deep convective clouds are especially important in the Earth system. They produce intense precipitation, severe weather and expansive anvil clouds, and thus have far-reaching

impacts on both weather and climate. It is therefore imperative to understand how these clouds respond to varying CCN concentrations. Deep convective clouds are typically driven by buoyancy and pressure gradients and have depths of several kilometers, often reaching the tropopause. Because of their depths, these clouds usually traverse the freezing level in the atmosphere, invoking both liquid and ice microphysical processes.

The primary pathway for CCN effects in deep convection is rooted within the updraft, where the atmosphere can become supersaturated due to the adiabatic cooling associated with the upward vertical motions. Within updrafts, CCN control the number concentrations of cloud droplets that form (recall Figure 1.2) and from this initial response, subsequent adjustments to the microphysical and dynamical processes ensue. For example, the initial responses within the updrafts can result in changes to the precipitation and resulting cold pools (e.g., van den Heever et al. 2006; Tao et al. 2007; Marinescu et al. 2017) and changes to the anvils (e.g., Saleeby et al. 2016), which can both feed back to new cloud development. These feedback processes complicate the net impact of CCN on the Earth system.

One of the primary concepts in CCN impacts in deep convective updrafts is often termed *invigoration*, whereby higher concentrations of cloud droplets that form in high-CCN conditions suppress precipitation processes (e.g., Albrecht 1989) and result in more latent heating within the cloud via either condensation, deposition or freezing processes (e.g., Andreae et al. 2004; Khain et al. 2005; Wang 2005; van den Heever et al. 2006). This increased latent heating results in more buoyant air and stronger vertical velocities within the updrafts, thereby *invigorating* the cloud. While the majority of studies have generally corroborated these initial studies, suggesting stronger updraft vertical velocities when increasing the CCN concentrations (e.g., van den Heever and Cotton 2007; Li et al. 2008; van den Heever et al. 2011; Fan et al. 2012), others

studies have shown negative or no responses in updraft velocities to increased CCN concentrations (e.g., Tao et al. 2007; Fan et al. 2009). These varying results have been attributed to differences in the environmental conditions in which the clouds form, such as differences in the convective available potential energy (CAPE; Lee et al. 2008; Storer and van den Heever, 2010; Storer et al. 2010), wind shear (e.g., Khain et al. 2008; Lee et al. 2008; Fan et al. 2009; Marinescu et al. 2017) and boundary-layer moisture (e.g., Khain et al. 2005; Tao et al. 2007; Khain et al. 2008), or to differences in microphysical parameterizations (e.g., Seifert et al. 2006; Lebo and Seinfeld, 2011). As can be seen, even for one of the more-established concepts in aerosol indirect effects in deep convective clouds, the results are muddled.

One underlying problem with understanding aerosol effects in deep convective clouds stems from a lack of comprehensive observations within deep convective updrafts. Due to the hazardous observing conditions within deep convective updrafts, the last U.S. research, storm-penetrating aircraft was decommissioned in 2005 (Geerts et al. 2018), and more recent in-situ measurements within deep convective updrafts have been scarce. Furthermore, the interpretation of observations of aerosol effects in deep convection present additional challenges. It is difficult to directly attribute changes in observed cloud features (i.e., updraft strength, cloud top height, precipitation) to changes in aerosol concentrations, because aerosol concentrations covary with many of the other thermodynamic variables that will also impact those same cloud features (e.g., Varble 2018). Modeling studies have led much of the discourse on aerosol-cloud interactions within deep convective clouds because they can better circumnavigate observational difficulties, particularly in their ability to better account for and assess the cloud's environment in simulation data and to systematically test the sensitivities in their results. In fact, some of the modeling-based research presented in Chapter 4 of this dissertation assisted in the development of a

proposal for a field campaign to provide better observations of aerosol impacts within deep convective clouds. TRACER (Tracking Aerosol Convection Interactions Experiment) takes place in Houston, Texas from April 2021 through April 2022 and aims to provide a more comprehensive observational dataset of convective clouds and their environments, which will assist in validating the current theories on aerosol impacts on deep convective clouds (Jensen et al. 2019).

1.3 Dissertation outline: motivation and science questions

The dissertation is a compilation of three studies that focus on improving the understanding of aerosol and deep convective updraft processes and their interactions. Chapters 2 and 3 present novel observations of aerosol particles and updrafts, respectively, while Chapter 4 shows the results from a model intercomparison study of aerosol-updraft interactions in deep convective clouds.

In Chapter 2[1], the following questions are addressed: 1) What are the typical aerosol particle size distributions for a rural, North American, continental location? 2) How do these typical size distributions vary be season?, and 3) What are the most important temporal cycles in aerosol particle concentrations, and do they vary as a function of particle size? The physical and chemical processes that govern the variability of aerosol particles determine the types and concentrations of aerosol particles that are available to interact with clouds. Furthermore, through quantifying the cycles in aerosol particle concentrations, their covariability with

[1] This study, titled "Quantifying aerosol size distributions and their temporal variability in the Southern Great Plains, USA," has been published in *Atmospheric Chemistry and Physics* (Marinescu et al. 2019a; © 2019 Copernicus); the pre-typeset and copyedited version appears in this dissertation.

different cloud types and environmental conditions can be assessed, which will bolster our understanding of the potential impacts that aerosol particles have on clouds. What is particularly unique about this study is the use of long-term observations (5 years) of size-resolved aerosol number concentrations, on which robust statistical analyses were completed. One of the primary findings of this study was that the smallest particles (diameters < 30 nm) have clear diurnal cycles that peak in the early afternoon hours. Both the timing of these diurnal cycles, which varies by season, and their consistent presence throughout the year, suggest that small particles may play a larger role in aerosol-cloud interactions than has been previously suggested. For longer time scales (days - weeks), aerosol number concentrations have cycles similar to those of synoptic weather patterns, which also vary based on the season. Further, statistics on typical seasonal aerosol size distributions were provided to assist in future modeling efforts.

Due to observing difficulties, in situ observations of vertical velocities within deep convective updrafts have been scarce, and most of the recent estimates of vertical velocities in deep convection are based on remotely sensed methods or cloud-resolving models, both of which have hard-to-characterize uncertainties (e.g., Nelson and Brown 1987; Oue et al. 2019). As part of the C^{3}LOUD-Ex field campaign (van den Heever et al. 2020), which took place in Colorado, Wyoming and Nebraska in 2016-2017, in situ observations of supercell updraft vertical velocities via targeted radiosonde launches were collected. These measurements are presented in Chapter 3[2],. Observations of vertical velocities on the order of 40-50 m s^{-1} were observed within two different supercell case studies. This research suggests that commonly used observations

[2] This study, which is co-authored by P. C. Kennedy, M. M. Bell, L. D. Grant, S. W. Freeman, A. J. Drager and S. C. van den Heever, is called "Updraft Vertical Velocity Observations and Uncertainties in High Plains Supercells Using Radiosondes and Radars" (Marinescu et al. 2020a, submitted) and is in review at *Monthly Weather Review*.

based on remote sensing (i.e., dual-Doppler analyses) may not be able to capture the most intense, localized vertical motions in storms, that can be captured by in situ measurements. Furthermore, this work has shown how the coordination of remotely sensed observations with in situ observations can provide the most value in future field campaigns (e.g., TRACER).

Chapter 4[3], addresses the interactions between aerosols and updrafts in deep convection. These interactions are complex, and different modeling studies have shown conflicting results in terms of the impact of increased aerosol particle concentrations within deep convective updrafts, as described above. In this study, results from a model intercomparison study are shown, whereby data from seven cloud-resolving models from research institutions around the world were used to answer the following question: for the same case study of deep convective clouds, what is the range of responses in deep convective cloud updrafts to similar changes in CCN concentrations within different models? The models generally produce consistent results in the warm-phase and mixed-phase regions of the updraft but begin to diverge at the higher levels where the ice phase is dominant. The different terms of the vertical velocity tendency equation are used to provide insights into the physical mechanisms causing the consistent and inconsistent trends amongst the different models. Finally, Chapter 5 provides a summary of the dissertation, as well as remarks on future work that directly stems from the research presented here.

[3] This study titled "The Impacts of Varying Concentrations of Cloud Condensation Nuclei On Deep Convective Cloud Updrafts – A Multimodel Assessment" (Marinescu et al. 2020b, in prep.) will be submitted to *Journal of Geophysical Research: Atmosphere*.

CHAPTER 2: QUANTIFYING AEROSOL SIZE DISTRIBUTIONS AND THEIR TEMPORAL VARIABILITY IN THE SOUTHERN GREAT PLAINS, USA

2.1 Introduction

Aerosol particles play a number of roles in the Earth-Atmosphere system, including impacting warm and cold cloud formation, solar and terrestrial radiation budgets, and human and environmental health. These impacts depend strongly on particle size, composition, and abundance. Aerosol number and mass concentrations arise from numerous sources and processes, including in situ chemical conversion, that shape the resulting chemical compositions and size distributions of the particle populations. Long-term observations provide insights to these processes by creating datasets that enable robust statistics regarding the typical temporal variations in aerosol properties. One such site with long-term aerosol measurements is the United States Department of Energy's Atmospheric Radiation Measurement's Southern Great Plains (SGP) site. Located in north central Oklahoma, the ARM-SGP site (Sisterson et al. 2016) is influenced by a variety of aerosol types, sources, and transport pathways (e.g., Peppler et al. 2000; Sheridan et al. 2001; Andrews et al. 2011), making it an ideal location to study a wide range of aerosol processes and to characterize aerosol properties for a typical North American, rural, continental site.

Several studies have utilized the long-term aerosol data at the SGP site to study aerosol temporal variability. Sheridan et al. (2001) provided a climatology using 4 years of data of aerosol optical properties at SGP, as well as monthly, daily, and hourly statistics of total aerosol number concentrations for particles with diameters (D_p) between ~10 nm and 3 μm. They found a diurnal cycle in total aerosol number concentrations that reached a minimum between 09 and

16 UTC, equivalent to 04 and 11 Central Daylight Time (CDT; CDT = UTC-5), and reached a maximum between 19 and 22 UTC (14 and 17 CDT). They also found a weak weekly cycle in aerosol number concentrations, with minimum concentrations on Sunday. However, their study did not assess the diurnal or weekly variability on a seasonal basis. Most recently, Sherman et al. (2015) assessed the temporal variability of aerosol optical properties at 4 different sites in the United States, including SGP. They found that aerosol optical properties (e.g., scattering and absorption coefficients of aerosol with $D_p < 1$ μm) had higher amplitude variations associated with seasonal time scales than with weekly or diurnal timescales at the individual sites, and that the seasonal variations at individual sites were larger than regional variations for the same season. Both findings support the need to understand aerosol processes on a seasonal basis. Sherman et al. (2015) was a follow-up study to, and generally consistent with, the results of Delene and Ogren (2002) and Sheridan et al. (2001), with all three studies focusing on aerosol optical properties at the SGP site. These studies demonstrated weak diurnal and weekly cycles of aerosol scattering and absorption that were significant depending on the season, with absorption having a stronger signal. Parworth et al. (2015) also provided some evidence of diurnal cycles in aerosol properties at the SGP site using 18 months of speciated aerosol mass concentration data (D_p between 100 nm and 1 μm). Jefferson et al. (2017) related some of the results from these prior studies to the seasonal variability in aerosol scattering coefficient hygroscopic growth with 7 years of SGP data.

None of these prior studies of long-term variability in aerosol properties at the SGP site exploited the multiyear datasets of number size distributions available for the site, which allow for specific size ranges of aerosol particles to be studied. Number size distributions have been used to understand a variety of aerosol processes, such as new particle formation and growth

(e.g., Dal Maso et al. 2005; Hallar et al. 2011; Pierce et al. 2014; Yu et al. 2015; Niemenen et al. 2018) and cloud processing of aerosol size distributions (e.g., Weingartner et al. 1999), at long-term aerosol observing sites around the world. Here, we present and analyze 5 years of aerosol number size distribution data (D_p between 7 nm and 14 μm) from the SGP site. Specifically, we develop descriptions of annually and seasonally averaged sub- and super-micron size distributions and quantify their variability. Such descriptions are useful for validating aerosol models on a variety of scales, and for selecting aerosol properties representative of the SGP site and the region. Representative aerosol size distributions at SGP are especially important for guiding the characteristics, location, and life cycle of aerosol particles in numerical modeling studies that try to represent the impacts of aerosol particles on the Earth system (e.g., Fridlind et al. 2017; Marinescu et al. 2017; Saleeby et al. 2016). Further, the long-term time series contain information on temporal cycles that can lead to insights into the aerosol sources and processes at SGP. In this work, we apply power spectral analysis to the time series of aerosol size distributions to determine the presence of significant temporal cycles in the aerosol data.

2.2 Data

The data presented here were collected at the SGP central facility (lat = 36.605, lon = -97.485), representing a typical North American, rural, continental site. This site has many atmospheric science observations platforms, all located within an approximately 1 km^2 area (Sisterson et al. 2016). This site is located within a large agricultural region in the central United States, which grows a variety of crops such as winter wheat, soybeans, cotton, corn and alfalfa and has open pasture land (USDA-NASS Oklahoma Field Office). Therefore, agricultural aerosol sources frequently impact the aerosol conditions observed at the SGP site. There are a

few local power plants (e.g., a coal-fired power plant in Red Rock, Oklahoma, 30 km to the southeast) and oil refineries (e.g., near Ponca City, Oklahoma, 35 km to the east), and Oklahoma City is approximately 130 km to the south. Besides local sources, the SGP site often encounters large concentrations of aerosol particles via long-range transport. High concentrations of aerosol particles associated with biomass burning in Central America and Mexico have been well documented in the spring and summer months (e.g., Peppler et al. 2000; Sheridan et al. 2001), although localized agricultural burning is also present (e.g., Parworth et al. 2015). Dust aerosol particles from both local sources and long-range transport have been observed at the SGP, as well (e.g., Andrews et al. 2011).

A scanning mobility particle sizer (SMPS), which was part of the tandem differential mobility analyzer system (TDMA), measured particle size distributions between approximately 12 and 750 nm (Collins 2010) during the 2009-2013 period at the SGP site. The size distributions were typically measured in 42-49-minute time intervals, which was longer than typical SMPS measurements due to simultaneous operation of the instrument as a TDMA to measure aerosol hygroscopicity. In this study, the data were binned into 2-hour intervals to create a more robust and evenly spaced dataset for analysis. For most of this time period, observations from an aerodynamic particle sizer (APS; TSI model 3321) were combined with the SMPS data to construct a number size distribution from ~12 nm to ~14 μm with 215 size bins (SMPS+APS; ARM Climate Research Facility, 2010, 2015). An assumed particle density of 2 g cm^{-3} was used to convert the aerodynamic diameter measured by the APS to mobility diameter prior to merging the two size distributions. A condensation particle counter (CPC; TSI model 3010; ARM Climate Research Facility, 2007, 2011), which has a ~10% detection efficiency for particles of 7 nm diameter (Mertes et al. 1995), was connected to the same inlet as the SMPS+APS. The CPC data

were used to augment the size distribution data at the smallest particle sizes, as described in the Appendix, to result in number concentrations for D_p ranging from 7 nm to ~14 μm. The details of the ARM data streams used, the multiple quality control tests performed, the size distribution adjustments made that incorporated the CPC data, and a validation of these adjustments are also included in the Appendix, and the final data product is archived (Marinescu et al. 2019). Of the 5 years of archive data that were processed, over 3 years of data (15,202 2-hour samples) passed our quality control process and were used in the subsequent analyses. The resulting dataset that was utilized in this study is shown in Figure 2.1. Gaps in the data timeline represent time periods with unavailable data or data that did not pass quality control tests. The largest gap in the data (October 2010 through April 2011) was due to an internal leak in the CPC that was documented in the ARM dataset. While the SMPS+APS data were available during this period, the CPC adjustments could not be made and therefore, these data were excluded from this study.

2.3 Seasonal variations in aerosol concentrations

Several previous studies have found seasonal differences in aerosol properties at the SGP site (e.g., Andrews et al. 2011; Parworth et al. 2015; Sherman et al. 2015), and we therefore used the same season definitions (MAM, JJA, SON, DJF) as these prior studies in order to facilitate comparisons. Throughout this manuscript, the terms MAM, JJA, SON, and DJF can be used interchangeably with spring, summer, autumn and winter, respectively. The 25th, 50th, and 75th percentile aerosol number (N) size distributions were computed for each season as well as for the entire 5-year period (ALL) and are shown in Figure 2.2a; these number distributions were converted to surface area (S) and volume (V) size distributions as shown in Figure 2.2b and c. While similarities are evident in the seasonal size distributions' shapes and modes, several

differences between the seasons can be seen in Figure 2.2. JJA had a higher fractional contribution of particles with diameters larger than 50 nm as compared to the other seasons, which led to higher total surface area and volume concentrations in JJA. MAM and SON more

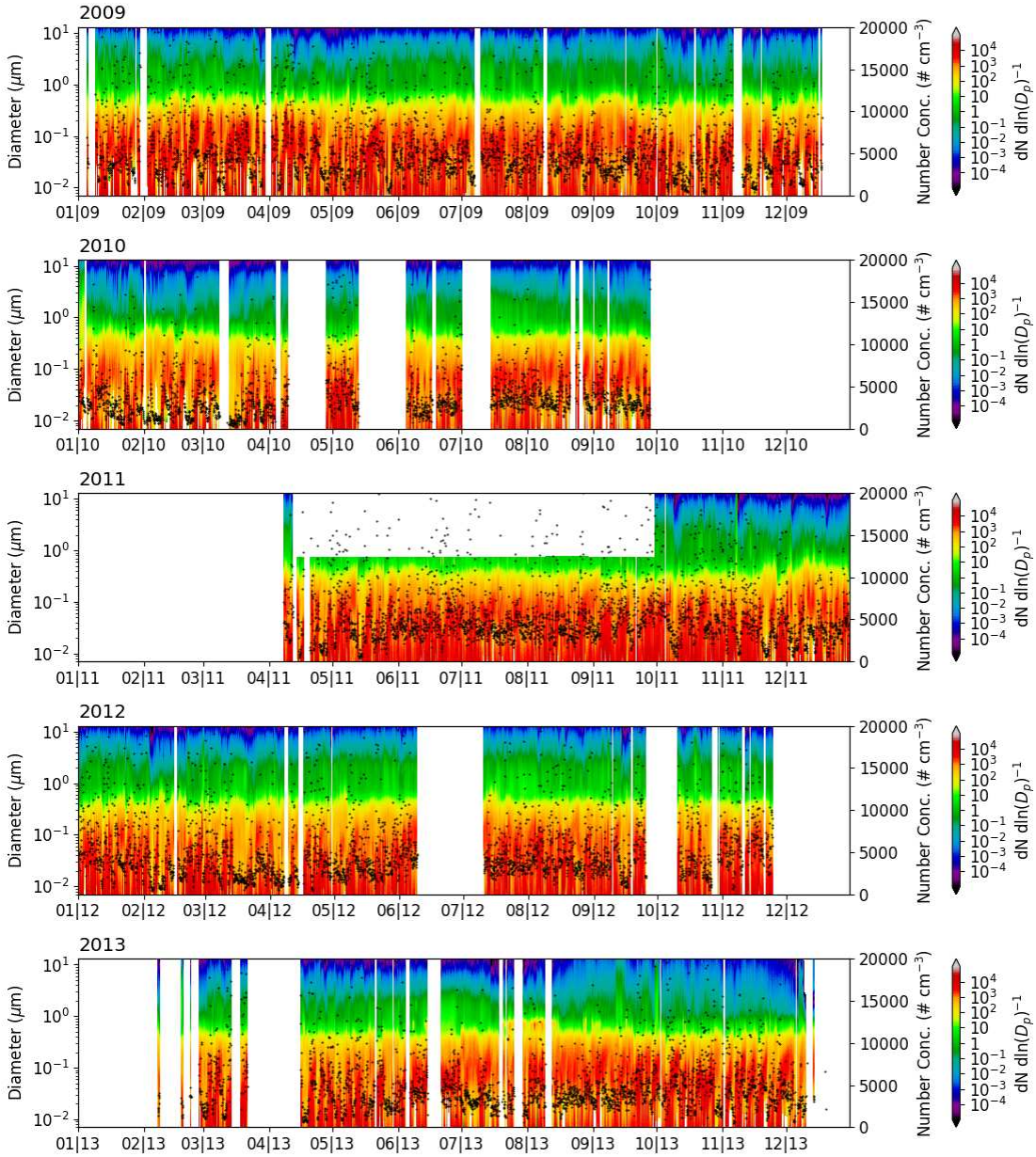

Figure 2.1 Time series of the final aerosol dataset used in this study following the quality control and the aerosol number size distribution adjustments, as described in Appendix 1. Each row represents one year from 2009 through 2013. The shading represents the value of the number size distribution, dN $dlnD_p^{-1}$, as a function of diameter (left axis), and the black dots represent the total integrated number concentrations (N_T, right axis).

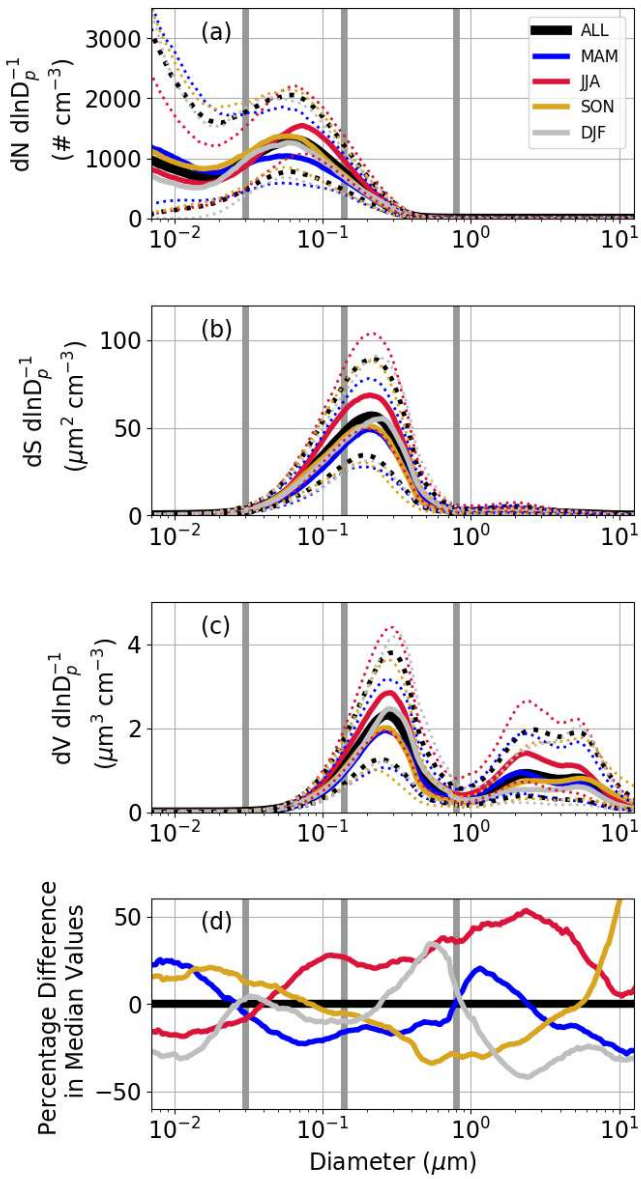

Figure 2.2. Aerosol size distributions for the entire time period and by season. (a) represents the number size distributions (# cm^{-3}), (b) represents the surface area size distributions (μm^2 cm^{-3}), and (c) represents the volume size distributions (μm^3 cm^{-3}). The solid colored lines depict the median values, and the dotted lines depict the 25th and 75th percentiles. (d) represents the percentage difference in the median size distributions for each season with respect to the entire period (ALL). The vertical grey lines demarcate the four separate regions of the size distribution that were used for further analyses in this study.

frequently had larger concentrations of the smallest particles (D_p< 20nm), while DJF often had very few small particles. Four lognormal distribution modes were found to best fit the median size distributions (Fig 2.3), where the lognormal distribution was defined as:

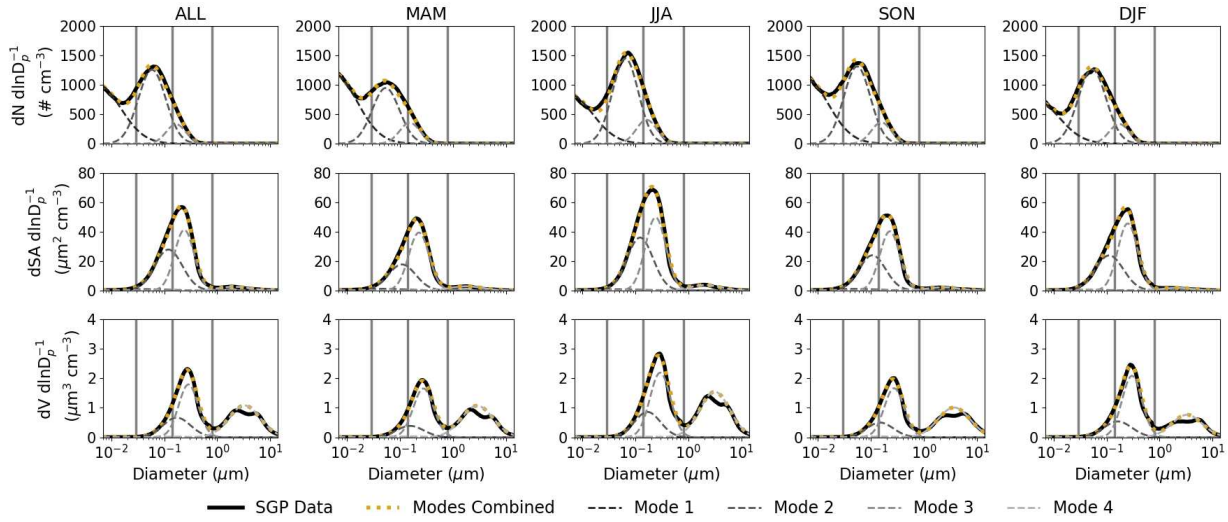

Figure 2.3. Median distributions from each season (black) fitted with 4 lognormal distributions (modes). The columns (left to right) represent the time periods ALL, MAM, JJA, SON, and DJF, respectively. The rows (top to bottom) represent the number, surface area, and volume size distributions, respectively. The vertical grey lines demarcate the four separate regions of the size distribution that were used for further analyses in this study

$$N\big(\ln(D_p)\big) = \frac{dN}{dln(D_p)} = \frac{N_0}{\ln(\sigma_g)\sqrt{2\pi}} e^{-\frac{(\ln(D_p)-\ln(D_m))^2}{2\ln^2(\sigma_g)}} \quad (2.1)$$

where N_0 is a total number concentration within the mode (# cm^{-3}), σ_g is the geometric standard deviation, and D_m is the median diameter (μm). One lognormal mode, as opposed to two, was chosen to fit the coarse mode because the decrease in concentrations around 3 μm was a data artifact, which is believed to have been caused by inaccurate size bin boundaries determined from the initial instrument calibration. The fitting was completed such that the mode parameters (Table 1) were converted between the number, surface area, and volume size distributions, and the integrated number and surface area were within 1% of the observed median values. The integrated volume values from the fitted distributions were ~2-4% higher than the median distributions values due to the aforementioned data artifact. The parameters for the number size distributions are shown in Table 2.1. The persistent but highly variable presence of a sub-30 nm mode, not completely resolved by the instrumentation at SGP, was likely associated

with the growth of newly formed aerosol particles into the size ranges that were observed by the instrument suite used here. The next two modes approximate Aitken and accumulation modes with lognormal number distribution median diameters of 50-65 nm and 150-175 nm, respectively. Finally, one coarse mode represents the supermicron aerosol particles. It is important to note that the location and steepness of the drop-off in the largest aerosol mode may be related to the upper limit of the APS, as well as the decrease in inlet transmission efficiency

Table 2.1. Parameters for each mode of the fitted lognormal distributions for the number size distributions shown in Figure 3. N_0 represents the amplitude of the lognormal distribution and the total number concentration within the mode (# cm^{-3}), D_m represents the median diameter (μm), and σ_g represents the geometric standard deviation, all as denoted in Equation 2.1 in the text.

	ALL	MAM	JJA	SON	DJF
Mode 1					
N_0	2606	3083	2171	2910	1911
D_m	0.00530	0.00550	0.00550	0.00550	0.00450
σ_g	2.80	2.80	2.80	2.80	2.80
Mode 2					
N_0	1883	1406	2049	1896	1929
D_m	0.05866	0.05426	0.06460	0.05459	0.05343
σ_g	1.82	1.81	1.76	1.78	1.84
Mode 3					
N_0	352	395	452	391	362
D_m	0.16624	0.15416	0.16189	0.15605	0.17262
σ_g	1.53	1.56	1.56	1.54	1.54
Mode 4					
N_0	0.791	1.244	1.100	0.576	0.486
D_m	0.82355	0.69573	0.85788	0.87508	0.88354
σ_g	1.97	1.99	1.93	2.00	1.94

for the largest particles, which was not corrected for in this dataset. The resulting 4 regions of the aerosol size distribution are demarcated by the vertical grey lines in Figure 2.2 and Figure 2.3 and represent particles with D_p between 7 and 30 nm, 30 and 140 nm, 140 and 800 nm, and 800 nm and 14 μm. The integrated number concentrations within these 4 size ranges ($N_{7\text{-}30nm}$, $N_{30\text{-}140nm}$, $N_{140\text{-}800nm}$, and N_{800nm+}) are used for further analyses in this study. While the focus of this study is primarily on number concentrations, we have performed the same analyses for the same aerosol modes for integrated surface area and volume concentrations. Generally, the results were consistent amongst the integrated number, surface area, and volume distributions. These analyses are included in the supplement for completeness.

To better quantify the variability within a season as well as the differences between seasons, Figure 2.4 shows the distributions of total measured aerosol number concentrations of particles between 7 nm and 14 μm (N_T) for the entire period (ALL) and for each season, as well as the integrated number concentrations for each of the 4 size ranges. To estimate the statistical significance of the differences between the seasonal distributions, a simple bootstrapping technique was used. For each season, the effective sample size was estimated using lag-1 autocorrelations (Leith 1973; Wilks, 2011) since the 2-hour samples were not independent. This typically reduced the sample size by a factor of 0.04-0.29, depending on the lag-1 autocorrelation of each integrated variable in each season. 10,000 random samples of a size equal to the effective sample size for each season were drawn, with replacement, from the ALL distribution. For each of the 10,000 random samples, the mean, median, interquartile range (IQR), and the 5% and 95% percentile range (R595) were calculated, resulting in a distribution of these summary statistics for the 10,000 ALL random samples. Then, the mean, median, IQR and R595 were computed for each season's data and were compared to the distribution of the same statistic for the 10,000

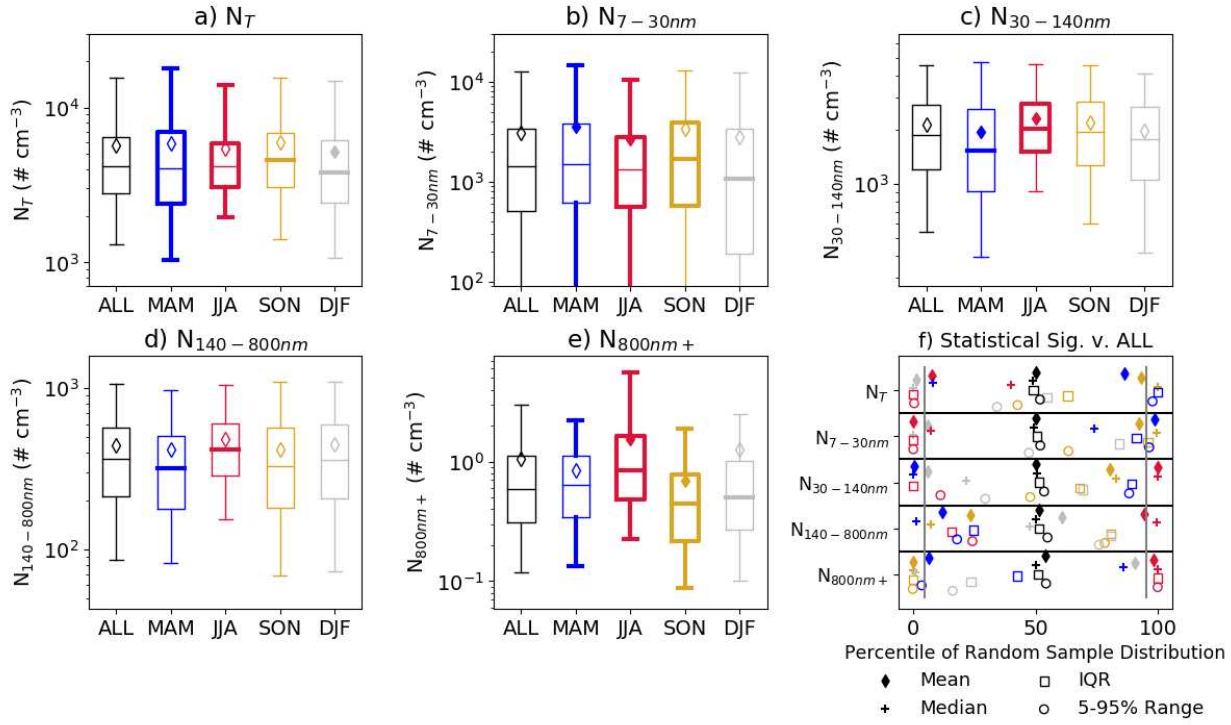

Figure 2.4. Distributions of integrated number concentrations for the entire size distribution (a) and for the 4 size ranges (b-e, $N_{7\text{-}30nm}$, $N_{30\text{-}140nm}$, $N_{140\text{-}800nm}$, and N_{800nm+}), shown as box-plot diagrams. Data are shown for the entire time period (ALL) and by season. The boxes represent the interquartile ranges separated into two boxes by the median values, the diamonds represent the mean values, and the lines extending from the boxes represent the 5th and 95th percentiles. Bolded lines and solid symbols in panels (a) through (e) represent differences between the seasonal and ALL variables that are statistically significant at the 95% level, as described in the text and shown in panel (f). The vertical grey lines in (f) are the 5th and 95th percentiles.

ALL random samples. For example, the DJF mean concentration for N_T (5195 cm^{-3}) was equal to the 1st percentile of the 10,000 ALL random sample means (grey diamond in the top row of Fig. 2.4f). In other words, when 10,000 random samples of the ALL N_T data were taken with the effective sample size of the DJF N_T data, only 1% of those 10,000 samples had means smaller than the DJF mean, suggesting the DJF mean value is significantly different from (in this case significantly less than) the ALL mean value. The same process was completed for the median, IQR, and R595 statistics for each season. Bolded distribution characteristics in Figure 2.4a-e represent instances where that key statistic was less than the 5th percentile or greater than the 95th

percentile of the distribution of random samples from the ALL data (Fig. 2.4f), suggesting significantly lower and higher values than the ALL data, respectively. It is important to note that these are arbitrary levels of significance, and Figure 2.4f shows the entire range of percentile values for each distribution statistic for all the integrated number variables. We have also included the same analysis for surface area and volume distributions in the Supplement.

In terms of total aerosol number concentrations (N_T, Figure 2.4a), the DJF mean (5195 cm^{-3}) and median (3808 cm^{-3}) concentrations were significantly lower than ALL, while the median SON value (4572 cm^{-3}) was significantly higher than the other time periods. MAM was the most variable season, with a significantly different IQR and R595, while JJA was significantly less variable than the other time periods, with a lower IQR and R595. For example, the R595s were 14286 cm^{-3}, 16889 cm^{-3}, 11957 cm^{-3}, 14072 cm^{-3}, and 13772 cm^{-3} for ALL, MAM, JJA, SON, and DJF, respectively. These R595 results are consistent with the results of Sheridan et al. (2001), particularly their Figure 5, which showed the largest breadth of number concentrations in the spring months and smallest breadth in the summer months. These results suggest the importance of seasonal synoptic scale weather variability with respect to N_T variability. For example, Andrews et al. (2011) used back trajectories to determine the transport pathways of aerosol to the SGP site, and in the MAM, SON and DJF periods, there were high frequencies of pathways coming both from the northwest and from the south or southeast, while in JJA the pathways were primarily from the same direction (southerly), resulting in lower variability in observed aerosol properties. Furthermore, several studies have documented episodically high concentrations of aerosol particles at SGP in MAM from both local agricultural / wildfire sources and from the transport of biomass burning aerosol into this region from various parts of North America (e.g., Peppler et al. 2000; Wang et al. 2009).

For $N_{7\text{-}30nm}$, the MAM mean value (3512 cm^{-3}) was the largest of all seasons, while the SON median value (1669 cm^{-3}) was the largest, demonstrating the MAM had the most extreme high concentrations of particles within this smallest size mode, while high concentrations were more frequent during SON. JJA had a significantly lower mean (2639 cm^{-3}) value for total concentrations within this mode, as well as significantly lower variability in terms of lower IQR (2196 cm^{-3}) and R595 (10315 cm^{-3}), as compared to the other time periods, which may have been a result of a consistent coagulation sink due to the higher concentrations of larger aerosol (Fig. 2.2). DJF had the highest frequency of low concentrations, which lowered the median concentration (1080 cm^{-3}). This smallest size mode was also associated with the highest variability of all the aerosol modes (in terms of absolute values) as seen by the breadth of the R595 (spanning several orders of magnitude). This large variability was likely caused by the frequent bursts of high concentrations associated with new particle formation and the growth of these newly formed particles into the size ranges observed in this study, although uncertainties associated with the observations of particles within this smallest mode may have also contributed to this variability, as discussed in Appendix 1.

For $N_{30\text{-}140nm}$, a shift in seasonal trends occurred. JJA, which had significantly lower concentrations than ALL for $N_{7\text{-}30nm}$, had a significantly larger mean (2315 cm^{-3}) and median (2037 cm^{-3}) concentration, which could be related to enhanced precursor concentrations in the summer months (e.g., Parworth et al. 2015). A similar reversal of trends occurred for MAM, which had a significantly lower mean (1959 cm^{-3}) and median (1523 cm^{-3}) concentration for $N_{30\text{-}140nm}$ as compared to ALL. As was the case for $N_{7\text{-}30nm}$, JJA was the least variable season for $N_{30\text{-}140nm}$. The seasonal trends for $N_{140\text{-}800nm}$ were similar to $N_{30\text{-}140nm}$, albeit with smaller differences between the seasons.

There was large seasonal variability associated with concentrations of the largest particles (N_{800nm+}). JJA had a significantly higher mean (1.53 cm^{-3}) and median (0.85 cm^{-3}) concentration and had significantly higher variability (R595 of 5.32 cm^{-3}), as compared to the other seasons. On the other hand, SON had a significantly lower mean (0.69 cm^{-3}) and median (0.44 cm^{-3}) concentration and significantly lower variability (R595 of 1.79 cm^{-3}), as compared to ALL. MAM also had significantly lower variability (R595 of 2.07 cm^{-3}). Interestingly, while DJF had a significantly low median concentration (0.50 cm^{-3}) as compared to ALL, its mean concentration (1.27 cm^{-3}) was larger than the ALL data mean (1.06 cm^{-3}), due to the presence of a few time periods with very high concentrations within this mode. These N_{800nm+} results are generally consistent with prior studies (Sheridan et al. 2001; Andrews et al. 2011), which have attributed the seasonal presence of coarse mode aerosol particles to dust, both from local sources and transported into the region.

2.4 Sub-seasonal cycles within aerosol number concentrations

a. Methods

While the prior section was focused on seasonal differences in the aerosol size distribution, the focus of this section is the investigation of the sub-seasonal variability on time scales from several hours to several weeks using power spectral analysis. Power spectral analysis is a computational tool that fits a range of harmonic functions of varying frequencies to a data series using Fourier sums, and then calculates the amount of total variance in a data series that can be explained by each harmonic function, each associated with a specific frequency and period. The amount of variance explained by each frequency is often termed the power spectrum. The length and resolution of the data series on which the power spectral analysis is computed

determines the frequencies of cycles within the dataset that can be resolved and tested. The cycle periods (T) and frequencies (f) that are resolved in such analyses are given by:

$$T = \frac{1}{f} = \frac{M}{k}\ , where\ k = 1, \dots ,\ \frac{M}{2} \tag{2.2}$$

where M is the length of the data series.

The aerosol number concentration data were separated into the 4 seasons as was done in Section 2.3. Then, the data were further partitioned into years to ensure a continuous time series, a requirement for spectral analysis. This partitioning resulted in the following 21 data subsets JF-2009, MAM-2009, JJA-2009, SON-2009, DJF-2010, …, SON-2013, D-2014. The DJF seasons included the December month of the prior year to create the continuous time period. For each of these 21 subsets, anomalies were first recalculated as differences from the subset mean and the anomalous data were then separated into smaller data chunks (7 days and 28 days in this study) for spectral analysis. Two choices for the length of the data series (*M*) were used in order to study different temporal scales. The resulting power spectra were averaged together by season for all the years and tested for significance. Separating each of the 21 seasonal subsets into smaller data chunks and averaging the resulting power spectra together increased the robustness of the analysis. Because of the difficulties in fitting harmonic functions at the edges of finite data, a Hanning window was applied to smooth the data. However, it should be noted that using such a smoothing method also limited the smallest frequency (largest period) that could be accurately detected. In order to account for this smoothing and to incorporate all the data, a 50% overlap window was also applied to the data.

To determine the statistical significance of the averaged power spectra, red noise spectra were estimated from the data. For each length *M* data chunk without any missing values, the lag-

1 autocorrelation (r_{lag1}) was determined. The red noise power spectra were then computed for each data chunk using the following formula from Gilman et al. (1963):

$$red\ noise(f,r) = \frac{1-r_{lag1}^2}{1-2r_{lag1}cos(2\pi f)+r_{lag1}^2} \quad (2.3)$$

These red noise power spectra were averaged together for each season. The 99% confidence level was calculated using the F-distribution, with the test statistic being the ratio of variances (i.e., power) of the actual data to that of red noise at the same frequencies. The degrees of freedom used for calculating the 99% confidence level were based on the number of individual power spectra that were averaged together multiplied by 2.8 (Welch 1967) for the actual data spectra and 1000 for the red noise spectra. Choosing a relatively large value (1000) for the red noise degrees of freedom demonstrates confidence in our red noise spectrum formulation. However, other values (100, 500) were tested and resulted in no qualitative changes to the results presented herein.

b. Hourly-to-daily cycles of aerosol number concentrations

To determine the hourly-to-daily power spectra, the data series were binned and averaged over 2-hour intervals, with a length of the data series (*M*) of 7 days, thus resolving 4-hour to 3.5-day cycles in the data. Missing data for up to 6 hours were interpolated linearly from surrounding values. The resulting power spectra for total aerosol concentrations (N_T), for the entire period and by season, are shown in Figure 2.5. The strongest cycle in this aerosol dataset was the 24-hour or diurnal cycle. This was present in the average power spectrum for each season and for the entire dataset and always exceeded the 99% significance level as compared to red noise. In other words, we can state with very high confidence that the diurnal cycle in these data did not arise from random fluctuations as represented by a red noise time series. 48%, 37%, 42%, and

42% of the total number of weekly data chunks had power associated with the diurnal cycle greater than that of red noise for MAM, JJA, SON, and DJF, respectively. Therefore, while MAM had slightly more frequent diurnal cycles in N_T, this diurnal cycle was a year-round

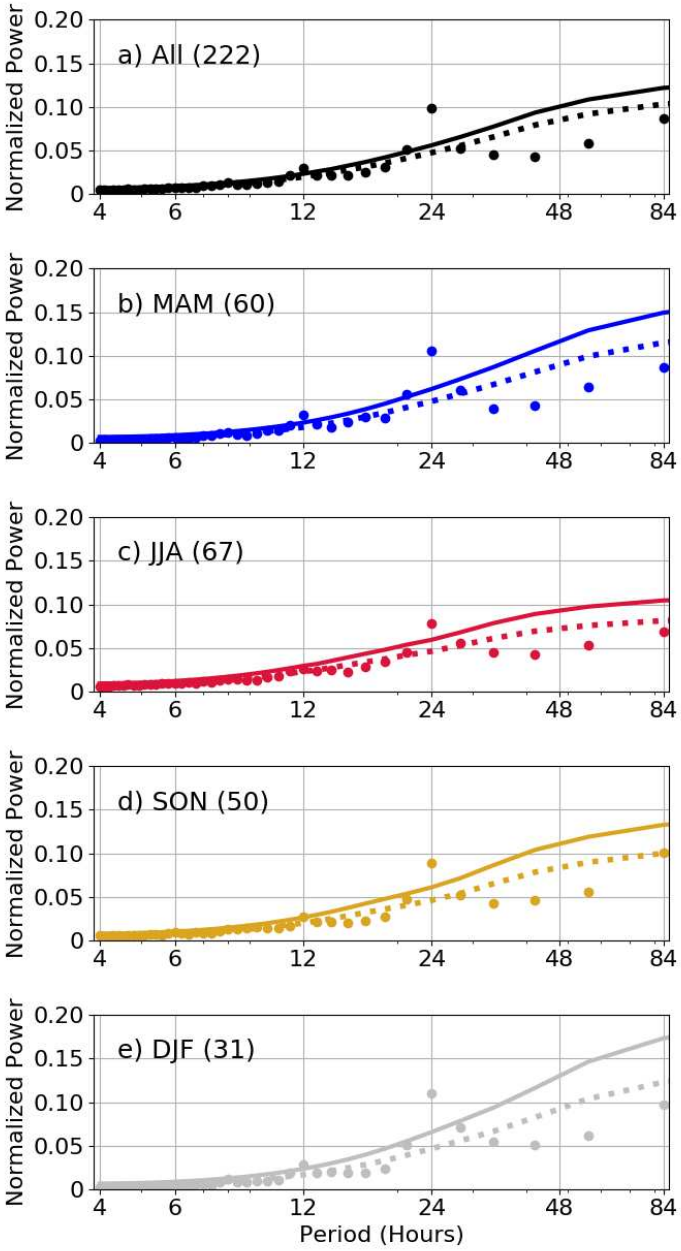

Figure 2.5. Normalized power spectra for N_T for the entire period (a) and by season (b-e). The dots represent power associated with the data. The dashed lines represent an estimate of the red noise power spectrum for each data set, and the solid lines represent the 99% significance testing level, as described in the text. The values in the parentheses are the number of weekly data chunks used in this analysis.

phenomenon at the SGP site. All seasons, except JJA, also exhibited a 12-hour cycle in N_T at 99% confidence. We will first focus on the 24-hour cycle and then examine the 12-hour cycle in the following sections.

i. 24-hour (diurnal) cycle of aerosol particles

The subset of weekly data chunks that had power associated with the diurnal cycle greater than that of red noise was used to calculate the timing of the maximum and minimum aerosol concentrations associated with the diurnal cycle. Although the focus here will be on the timing of the maximum concentrations, the timing of minimum concentrations can be calculated by shifting the maximum concentration timing by half of the period of interest (i.e., for the diurnal cycle, a 12-hour shift between maximum and minimum concentrations). Figure 2.6

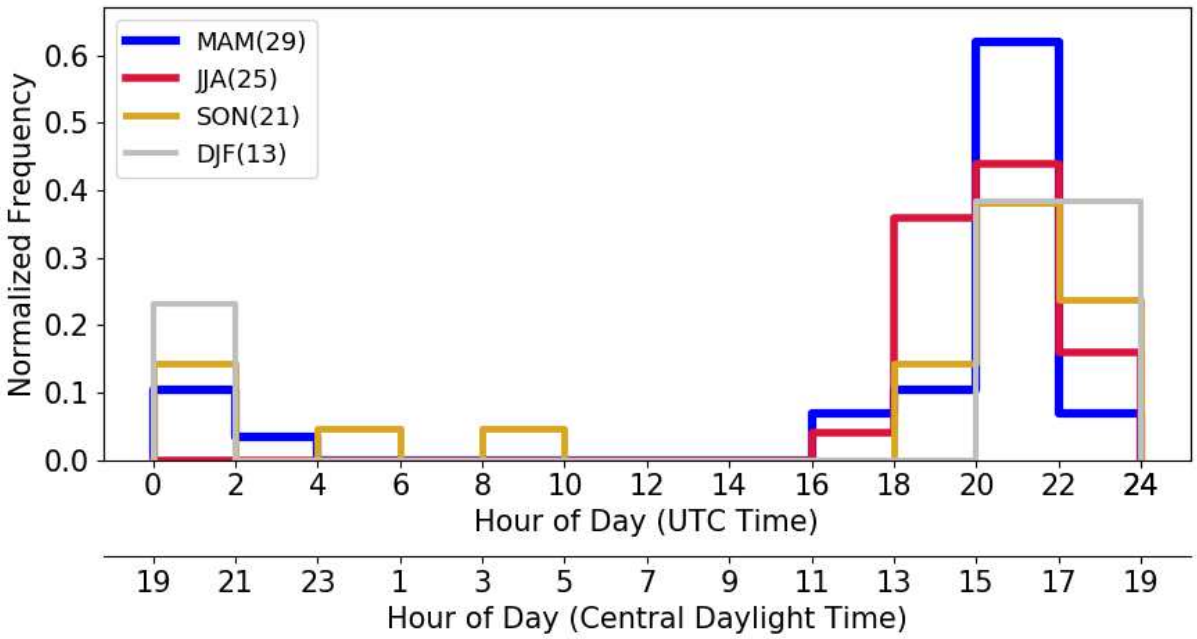

Figure 2.6. Normalized frequency of the daily time of peak concentrations associated with the 24-hour cycle in N_T. This figure only includes weekly data chunks that had normalized power associated with the 24-hour cycle greater than that of the corresponding seasonal estimate of the red noise spectrum power. The numbers in parentheses represent the number of weekly data chunks that met this criterion.

shows the normalized frequency of the maximum aerosol concentrations associated with the diurnal cycle as a function of time. The maximum aerosol number concentrations associated with the diurnal cycle primarily occurred between 18 and 02 UTC (13 and 21 CDT). While the timing of the diurnal cycle peak was generally in the local afternoon and evening hours for all seasons, the exact timing shifted between the seasons. The peak in the JJA diurnal cycle occurred several hours earlier (peak concentrations around 18-22 UTC or 13-17 CDT) than the peak in the annual average (20-22 UTC or 15-17 CDT), and the peak for DJF was shifted towards the later hours (peak concentrations from 20-02 UTC or 15-21 CDT) relative to the annual average.

To better understand the aerosol processes related to this diurnal cycle in N_T and to test whether there were size-dependent cycles, power spectra for the integrated aerosol number concentrations for each of the 4 modes of the aerosol size distribution ($N_{7\text{-}30nm}$, $N_{30\text{-}140nm}$, $N_{140\text{-}800nm}$, and N_{800nm+}) were computed and are shown in Figure 2.7. There were statistically significant diurnal cycles for all seasons for $N_{7\text{-}30nm}$ and $N_{140\text{-}800nm}$. For $N_{30\text{-}140nm}$, JJA had the strongest diurnal cycle, although the diurnal cycles for $N_{30\text{-}140nm}$ were relatively weaker, as compared to red noise, than those for $N_{7\text{-}30nm}$ and $N_{140\text{-}800nm}$. For the largest particles (N_{800nm+}), there was no consistent diurnal cycle above that of red noise, although there was some enhanced power in JJA. These results were generally consistent for the integrated surface area and volume concentrations unless otherwise noted.

As was done for the total integrated number concentration for the entire size distribution, N_T, the timing of peak concentrations associated with the diurnal cycle was calculated for each of the 4 aerosol size ranges (Figure 2.8). Because small particles often accounted for the majority of the total number concentrations, $N_{7\text{-}30nm}$ was the primary driver of the diurnal signal in the total aerosol number concentrations (N_T, Figure 2.5). This was further corroborated by the fact

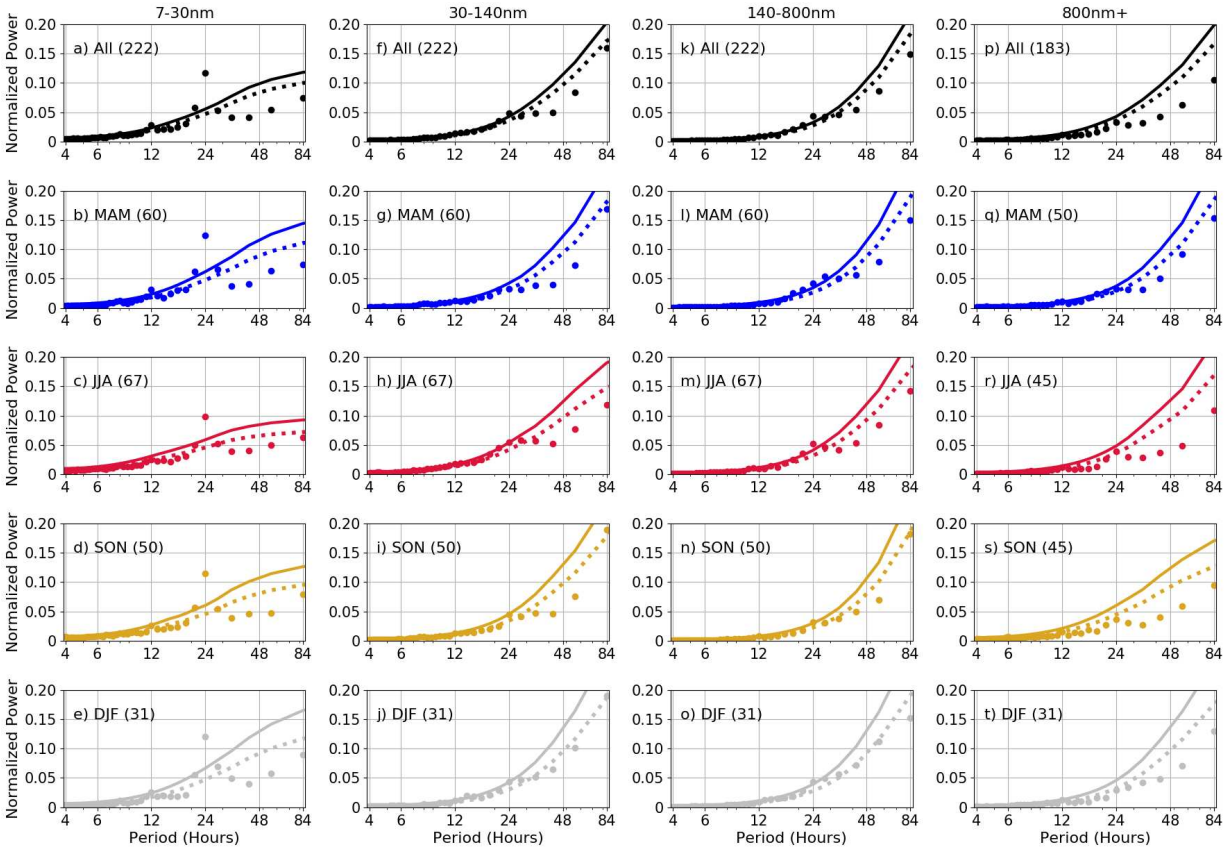

Figure 2.7. Normalized power spectra for $N_{7\text{-}30nm}$, $N_{30\text{-}140nm}$, $N_{140\text{-}800nm}$, and N_{800nm+} for the entire period and by season. The descriptions of the symbols used are the same as in Figure 2.5.

that the timing of the diurnal cycle peak concentrations for $N_{7\text{-}30nm}$ occurred at approximately the same times as that for N_T (compare Figure 2.8a with Figure 2.6). Aerosol particles in this smallest size range are typically presumed to have originated in new particle formation (NPF) events, followed by growth of those newly formed particles to sizes that can be detected by the instruments used in this study. Niemenen et al. (2018) assessed NPF at many sites around the world, including SGP, and found that the presence and growth of these small particles most frequently occurred in MAM (25% of the time) at SGP, but were much less frequent in the other seasons (10% in SON, 8% in DJF, and 4% in JJA). While our results corroborate the high concentrations of small particles in MAM, they also indicated consistent diurnal cycles of $N_{7\text{-}30nm}$

throughout the year. 55%, 46%, 56%, and 48% of the weekly $N_{7\text{-}30nm}$ data chunks had 24-hour cycles with power above that of red noise for MAM, JJA, SON, and DJF, respectively. Reasons for differences between this study and Niemenen et al. (2018) are likely related to the

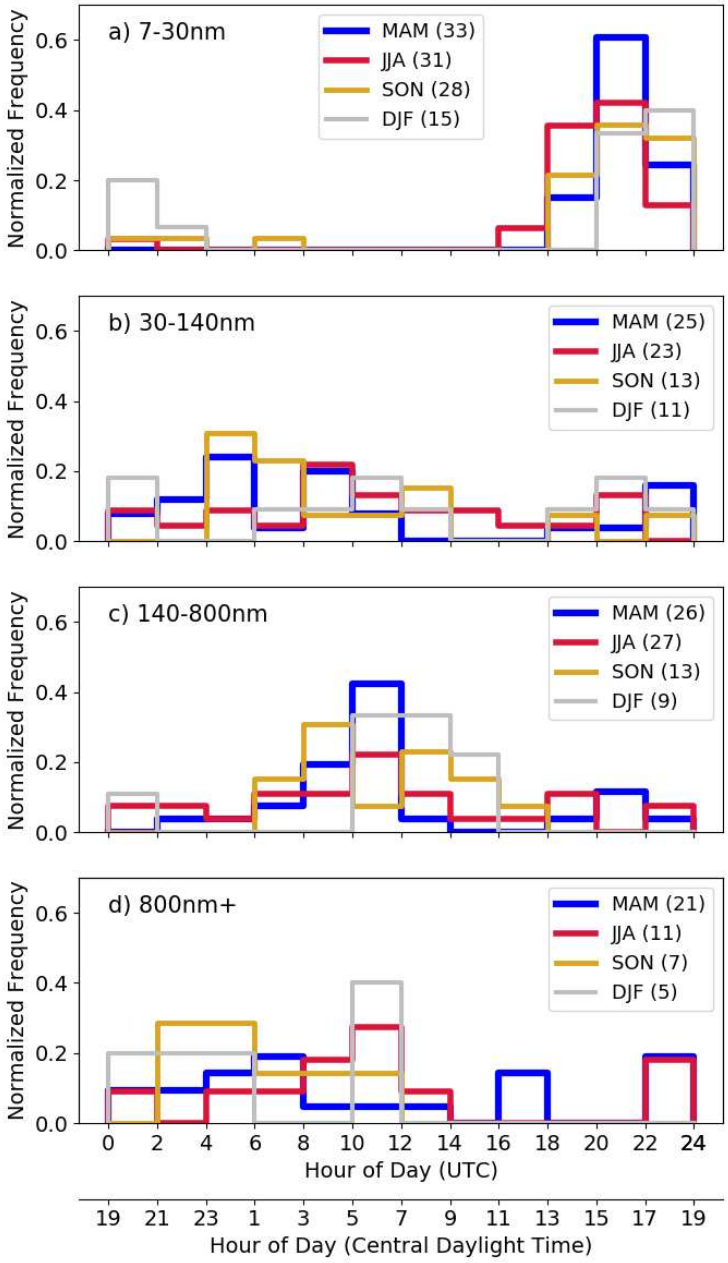

Figure 2.8. Normalized frequency of the daily time of peak concentrations associated with the 24-hour cycle in the different modes of the aerosol number size distribution. (a-d) represent $N_{7\text{-}30nm}$, $N_{30\text{-}140nm}$, $N_{140\text{-}800nm}$, and N_{800nm+}, respectively. The description of the figure is the same as in Figure 2.6.

incorporation of the CPC data and the adjustments made to the aerosol size distribution at these smaller sizes in this study (see Appendix 1), but are also related to the metric used to assess the presence of these small particles.

The broadly consistent timing of the diurnal cycle in $N_{7\text{-}30nm}$ throughout the year (local afternoon/evening) may suggest similar formation, growth, and/or transport mechanisms for aerosol with D_p between 7 and 30 nm. The several-hour seasonal shift in the timing of the peak concentrations between seasons may also help to elucidate some of the processes leading to observations of elevated $N_{7\text{-}30nm}$ at the SGP surface site. At SGP, the height of the atmospheric boundary layer reaches a specified altitude earlier in JJA and later in DJF, with MAM and SON falling in between (Liu and Liang, 2010; Delle Monache et al. 2004), which is consistent with the seasonal shift in the timing of the $N_{7\text{-}30nm}$ diurnal cycle. If the source region of these small particles were above the surface, then this shift in $N_{7\text{-}30nm}$ timing could also be impacted by the rate of vertical mixing and transport in the boundary layer in the different seasons. Chen et al. (2018) found that it took ~0.5-1.0 hour to vertically mix small aerosol particles from ~400 m above the ground to the surface during a new particle formation event on 12 May 2013 that occurred in an unstable atmosphere (lapse rate of 0.9-1.2ºC per 100m up to 400m AGL). This vertical mixing of aerosol from heights above the surface to the surface would take longer in boundary layers that are more statically stable, such as those typical in winter, and hence may also help to explain the seasonal shift in the timing of the $N_{7\text{-}30nm}$ diurnal cycle.

To assess the boundary layer evolution for the 5 years that are focused on in this study, boundary layer heights, estimated from radiosonde data, were examined (ARM Climate Research Facility, 2001). During 2009-2013, radiosondes were typically launched 4 times a day, at approximately 5:30, 11:30, 17:30, and 23:30 UTC. Boundary layer heights were estimated

using the bulk Richardson number and a threshold of 0.25 (Siebert et al. 2000); however, additional boundary layer height estimates (Sivaraman et al. 2013) were also tested and resulted in qualitatively similar statistics. The data were then filtered to only include the weekly data when the power associated with the $N_{7\text{-}30nm}$ diurnal cycle was within the top 25% of the data (high diurnal power, circles in Figure 2.9) and weekly data when the power associated with the $N_{7\text{-}30nm}$ diurnal cycle was within the bottom 25% of the data (low diurnal power, diamonds in Figure 2.9). Generally, the boundary layer at SGP reaches its maximum height between 20:00 and 23:00 UTC (15:00 and 18:00 CDT; Delle Monache et al. 2004; Liu and Liang, 2010), and therefore, was not resolved in this dataset. However, these data do demonstrate that weekly

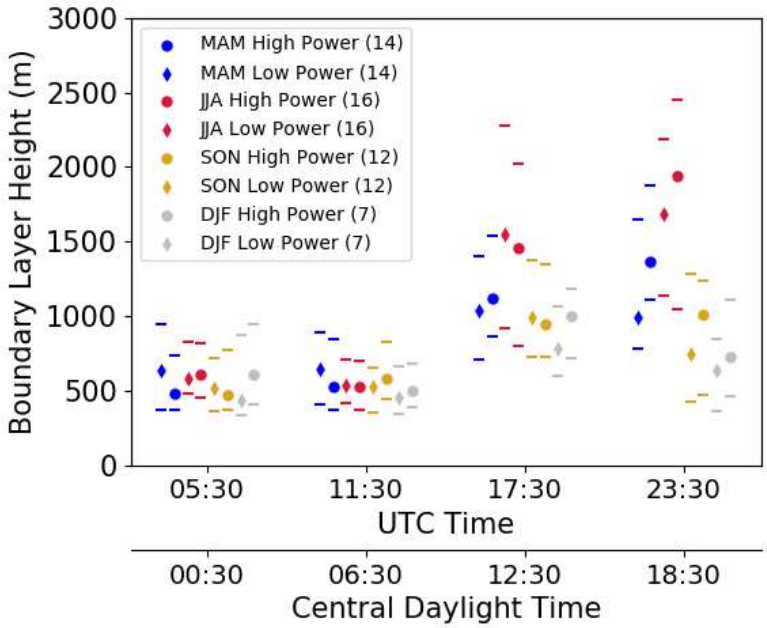

Figure 2.9. Diurnal cycle of boundary layer heights at SGP for each season, as estimated from radiosonde data. The circles represent the median boundary layer height for the top 25% of the weekly data in terms of power associated with the diurnal cycle in $N_{7\text{-}30nm}$ (High Power). Similarly, the diamonds represent the median boundary layer height for the bottom 25% of the weekly data (Low Power). The horizontal lines above and below the circles and diamonds represent the 25th and 75th percentiles (interquartile ranges) for these data. The numbers in parentheses represent the number of weekly time periods used in this analysis. The abscissa offset for each radiosonde launch time is for viewing purposes and does not reflect any shift in timing for each of the 4 radiosonde launch times for the different seasons.

periods with more consistent diurnal cycles in $N_{7\text{-}30nm}$ were associated with deeper boundary layers that extended into the late afternoon and evening hours, as can be seen by the higher median heights at 23:30 UTC for all seasons. This suggests that boundary layer development may play an important role in the $N_{7\text{-}30nm}$ diurnal cycle. However, the significant overlap in the boundary layer height interquartile ranges between weekly periods with strong and weak diurnal power also suggests that there are other significant factors, such as synoptic weather events and aerosol sources, that will impact the occurrence of consistent diurnal cycles in $N_{7\text{-}30nm}$. Both the evolution of the boundary layer at SGP and the shift in timing of the diurnal cycle of $N_{7\text{-}30nm}$ found in this present study corroborates earlier work that suggested nucleation of new particles sometimes occurs in the free troposphere or residual layer and is observed at the surface when mixing processes transport these aerosol to the surface (e.g., Weingartner et al. 1999; Hallar et al. 2011; Chen et al. 2018). The seasonal shift in the timing of the $N_{7\text{-}30nm}$ diurnal cycle may also be related to the seasonal shifts in insolation, including both the variation in sunrise times and intensity, and the resulting impacts on photochemical processes leading to the formation and growth of small aerosol particles (e.g., O'Dowd et al. 1999).

For $N_{30\text{-}140nm}$, there was a weaker diurnal signal in all seasons (Figure 2.7f-j). The timing of the peak concentrations often occurred in the night and early morning hours, several hours after the peak in concentrations of $N_{7\text{-}30nm}$. This signal could be representative of the growth of the $N_{7\text{-}30nm}$ aerosol mode to larger sizes. It is important to note that timing of peak concentrations of the diurnal cycle associated with these particles was more variable (Figure 2.8b) than for $N_{7\text{-}30nm}$, with peak concentrations occurring at almost all times of the day. Therefore, the timing of and processes associated with the diurnal cycle for $N_{30\text{-}140nm}$ were much less consistent

throughout this dataset and could be related to a wide range of aerosol, radiative, and dynamical processes.

For $N_{140\text{-}800nm}$, a more consistent diurnal cycle was present for all seasons (Figure 2.7k-o). The timing of the $N_{140\text{-}800nm}$ diurnal cycle was also generally consistent for all the seasons, with peak concentrations occurring between 08 and 16 UTC (03 and 11 CDT). These results are consistent with those for the integrated volume concentration for this mode ($V_{140\text{-}800nm}$, Figure 2.10k-o and Figure 2.11c), with volume concentrations providing a better comparison to prior studies that focused on optical properties and aerosol mass concentrations. For example, the timing of the diurnal cycle in $N_{140\text{-}800nm}$ (and $V_{140\text{-}800nm}$) was similar to the reported diurnal cycle

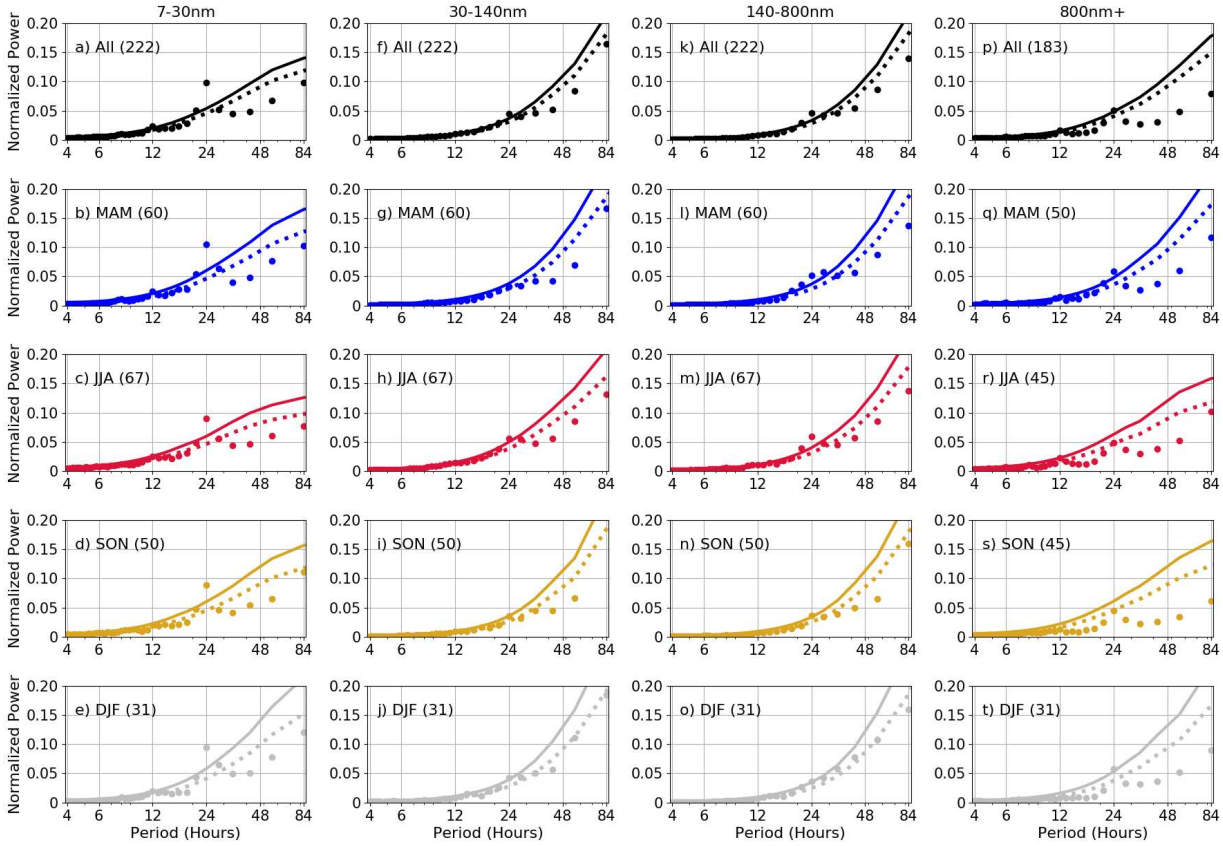

Figure 2.10. Normalized power spectra for $V_{7\text{-}30nm}$, $V_{30\text{-}140nm}$, $V_{140\text{-}800nm}$, and V_{800nm+} for the entire period and by season. The descriptions of the symbols used are the same as in Figure 2.5.

in the light absorption coefficient for $D_p < 10$ μm (Sheridan et al. 2001) and nitrate and organic aerosol mass concentrations for submicron particles from December 2011 through May 2011

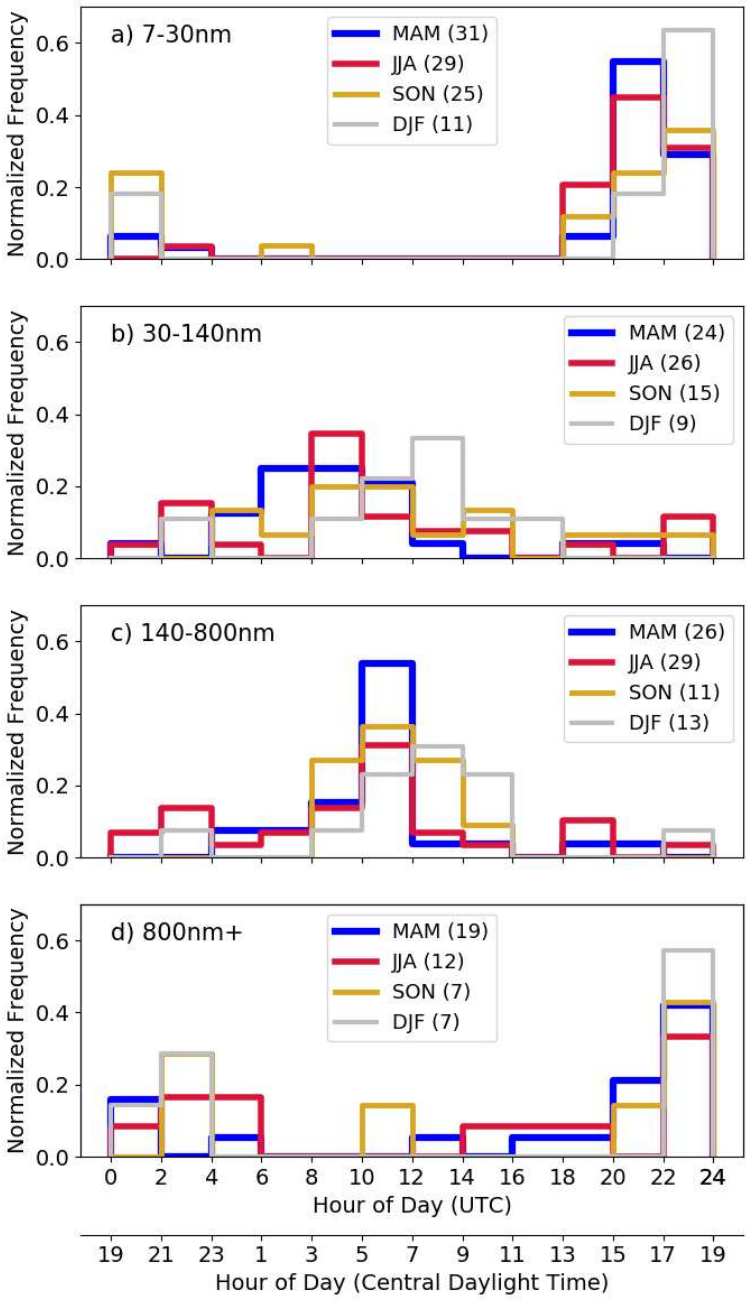

Figure 2.11. Normalized frequency of the daily time of peak concentrations associated with the 24-hour cycle in the different modes of the aerosol volume size distribution. (a-d) represent $V_{7\text{-}30nm}$, $V_{30\text{-}140nm}$, $V_{140\text{-}800nm}$, and V_{800nm+}, respectively. The description of the figure is the same as in Figure 2.6.

(Parworth et al. 2015). To explain this diurnal cycle in particles between 140 and 800 nm, data from an Aerosol Chemical Speciation Monitor (ACSM) at the SGP site (Ng et al. 2011) from

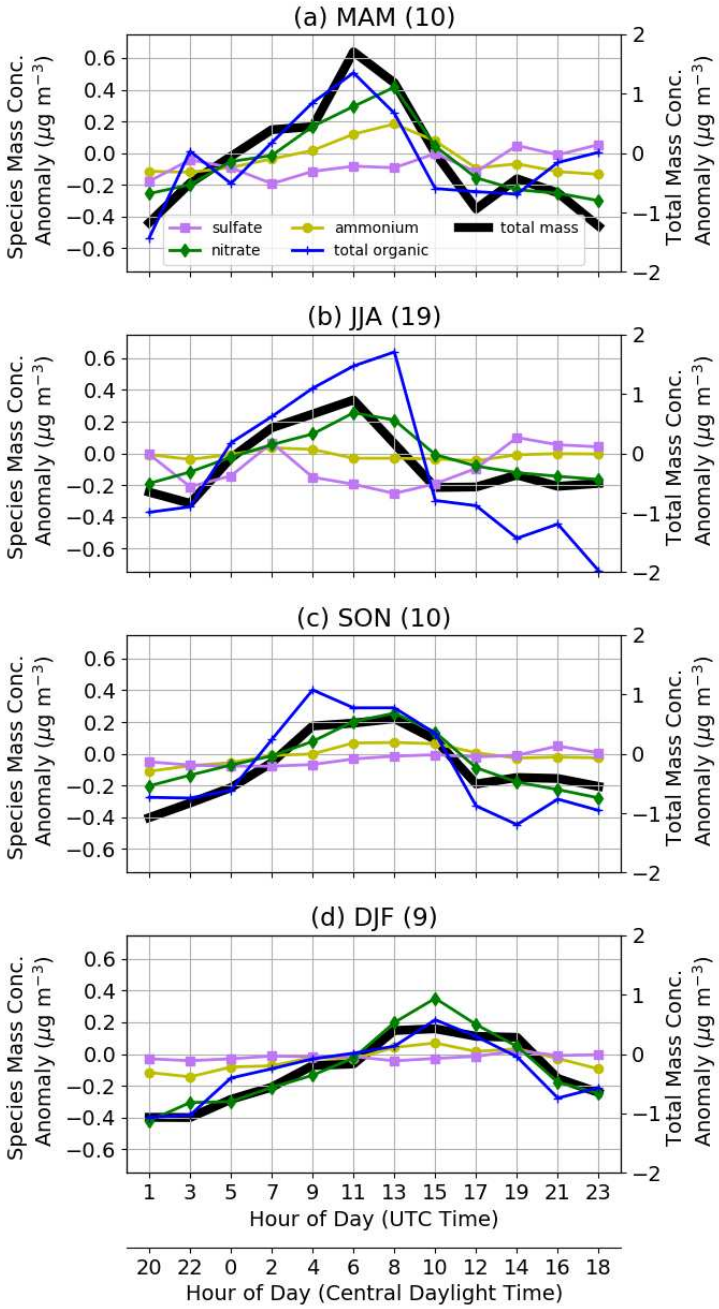

Figure 2.12. Diurnal cycle of aerosol mass concentration anomalies for sulfate, nitrate, ammonium, and organic aerosol species (left axis) and total mass concentrations (right axis) from the ACSM. The data were separated into seasons (a-d) and only included the weekly time periods where the power associated with the 24-hour cycle in integrated volume between 140 and 800nm ($V_{140\text{-}800nm}$) was greater than that of red noise. The number of these weekly time periods is shown in the parenthesis in the panel titles.

August 2011 through December 2013 was used. The data was filtered to only include weekly data with power associated with the $V_{140\text{-}800nm}$ diurnal cycle that was greater than that of red noise. The ACSM measured non-refractory submicron aerosol mass concentrations for several species, including nitrate, sulfate, ammonium, and organic aerosol. The timing of peak ACSM total mass concentrations (Figure 2.12) aligns with the timing of peak concentrations in $V_{140\text{-}800nm}$ and $N_{140\text{-}800nm}$ (Figure 2.11c and Figure 2.8c, respectively). The ACSM data demonstrate that the diurnal cycle in $V_{140\text{-}800nm}$ was related to nitrate and organic aerosol mass concentrations, although their relative contributions to the diurnal cycle varied by season. Organic aerosol had much stronger diurnal variations in JJA as compared to nitrate, while nitrate had stronger diurnal variations in DJF. Ammonium also had a similarly timed cycle in MAM, SON, and DJF, but with much lower anomalous concentrations. These trends represent a variety of aerosol processes, including temperature-dependent gas-to-particle partitioning, regional aerosol transport, and local emissions, and generally agree with the results of Parworth et al. (2015). Focused modeling studies and measurements are needed to further determine the specific and most important pathways leading to these diurnal cycles in aerosol concentrations.

Lastly, while there were no significant diurnal cycles in N_{800nm+} (Figure 2.7p-t), there were significant peaks for the diurnal cycle associated with the integrated volume of particles within this size range (V_{800nm+}, Figure 2.10p-t), with the strongest signals in MAM and DJF. The timing of peak concentrations associated with the diurnal cycle in V_{800nm+} was consistent amongst seasons and primarily occurred during the local evening hours, between 22-24 UTC (17-19 CDT, Figure 2.11d). The fact that this signal was weaker in N_{800nm+} suggests that the diurnal signal was primarily associated with the largest particles within the coarse aerosol mode. This result aligns with the results of Andrews et al. (2011), which documented low Ångström

exponent values in their spring and winter measurements at SGP, which is often a signal for large dust aerosol. Also, surface meteorology data from the SGP site (ARM Climate Research Facility 1995) during the same 5-year period demonstrate that surface winds, on average, reach a peak between 20 and 24 UTC, with stronger winds occurring in MAM and DJF. Therefore, we speculate that the timing of the V_{800nm+} diurnal cycle was related to the timing of strong wind conditions, which can loft large aerosol particles.

ii. 12-hour cycle of aerosol particles

The strongest cycle with respect to red noise in the N_T data was the diurnal cycle (Figure 2.5). However, there was also a statistically significant 12-hour cycle present in some of these data, particularly in MAM and DJF (Figure 2.5b,e). In general, the variability in N_T was caused by variability in $N_{7\text{-}30nm}$, due to the high concentrations and high variability of particles in this size range. The peak concentrations of the 12-hour cycle for all seasons occurred between 04 and 12 UTC (23 and 07 CDT) and between 16 and 24 UTC (11 and 19 CDT) for both N_T and $N_{7\text{-}30nm}$

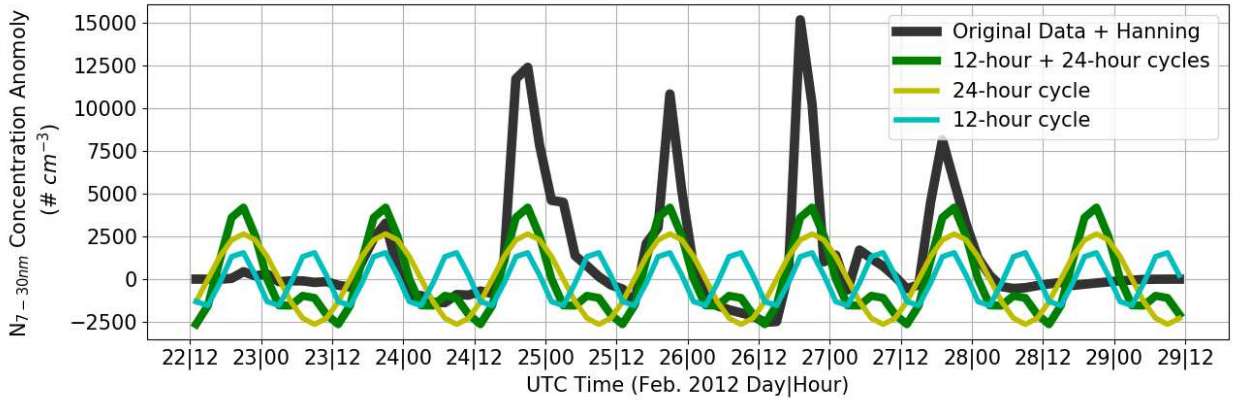

Figure 2.13. $N_{7\text{-}30nm}$ for the weekly data chunk that had the highest power associated with the 12-hour cycle (22-29 February 2012). The aerosol data are shown as a concentration anomaly from the seasonal mean (black). The anomaly data are broken down into the 12-hour cycle component (cyan), the 24-hour cycle component (yellow), and the combination of the 12- and 24-hour cycles (green), as computed by the power spectral analysis.

(not shown). The similarities between the timing of the peak concentrations of the 12-hour cycles for N_T and $N_{7\text{-}30nm}$ further demonstrate that the variability in $N_{7\text{-}30nm}$ is the driving mechanism for the variability in N_T.

The latter of the two daily peaks in concentrations associated with the 12-hour cycle occurred at approximately the same time as the peak concentrations associated with 24-hour cycle (16-02 UTC or 11-21 CDT), suggesting that the 12- and 24-hour cycles are related. To explain this relationship between the 12- and 24-hour cycles, Figure 2.13 shows the weekly aerosol data (22-29 February 2012) that had the strongest 12-hour cycle, broken down into their 12- and 24-hour cycle components. The peak concentrations of the 24-hour cycle (yellow) clearly aligned with the peak concentrations of the aerosol data (black). However, the minimum in aerosol concentrations typically occurred directly before peak $N_{7\text{-}30nm}$, as opposed to the 12-hour shift that would be associated with a purely diurnal cycle. When including the 12-hour cycle (cyan), the combination of the 12- and 24-hour cycles (green) much better represented the aerosol time series (black). Therefore, the power associated with the 12-hour cycle manifested from the different rates of growth and decay of aerosol number concentrations. The formation of $N_{7\text{-}30nm}$ occurred at a much faster rate than the loss of $N_{7\text{-}30nm}$. While the 12-hour cycle primarily manifested from the sudden increase in number concentrations in this size range, it is important to note there were also time periods where a second peak in $N_{7\text{-}30nm}$ occurred in the 04-12 UTC (23-07 CDT) time frame (e.g., 26-27 Feb 2012 in Figure 2.13).

c. Daily-to-weekly aerosol cycles

Several prior studies have demonstrated weekly cycles in aerosol total number concentrations (Sheridan et al, 2001) and aerosol optical properties (Delene and Ogren, 2002;

Sherman et al. 2015) at the SGP site. Spectral analyses aimed at resolving cycles on the order of 2 days to 14 days required re-partitioning of the data into daily samples and 28-day data chunks. In order to achieve a larger number of 28-day continuous samples, the dataset was doubled to include the time period between 1 January 2007 and 1 January 2017. However, since the SMPS+APS size distribution data were not available during this extended time range, only the total aerosol number concentrations from the CPC were used. The CPC data for this extended time range were screened in the same manner as was done for the earlier analyses and as described in Appendix 1. Figure 2.14 shows the power spectra for the entire period and by season for the expanded dataset. For the entire dataset, no cycles significant at the 99% confidence interval were found. However, the power spectra for MAM and SON had peaks just below this significance level for 7-day cycles, and the SON and DJF power spectra had peaks just missing this criterion for cycles lasting ~3.5-5 days. In JJA, there was no clear peak in the power spectrum above that of red noise on the time scales of 2-14 days. These results are possibly related to the temporal cycles of synoptic conditions and air masses in the southern United States. At the SGP site, JJA is typically associated with large-scale ridges and weak synoptic flows (Coleman and Rogers, 2007) that would lead to stagnant air masses and no consistent cycles on these time scales. Using four years of springtime data, Lanicci and Warner (1991) determined that changing synoptic patterns lead to an approximately one week cycle in elevated mixed layers in the southern United States, and therefore, this periodicity in synoptic patterns could help explain the weak weekly cycle in MAM. These results are also consistent with the higher intraseasonal variability observed in MAM, SON, and DJF for N_T (Figure 2.2). Other studies have corroborated our hypothesis about the importance of synoptic scale variability on aerosol concentrations at SGP. For example, Power et al. (2006) demonstrated significant

differences in aerosol optical depth based on the classified air mass present at many locations across the United States, including at SGP.

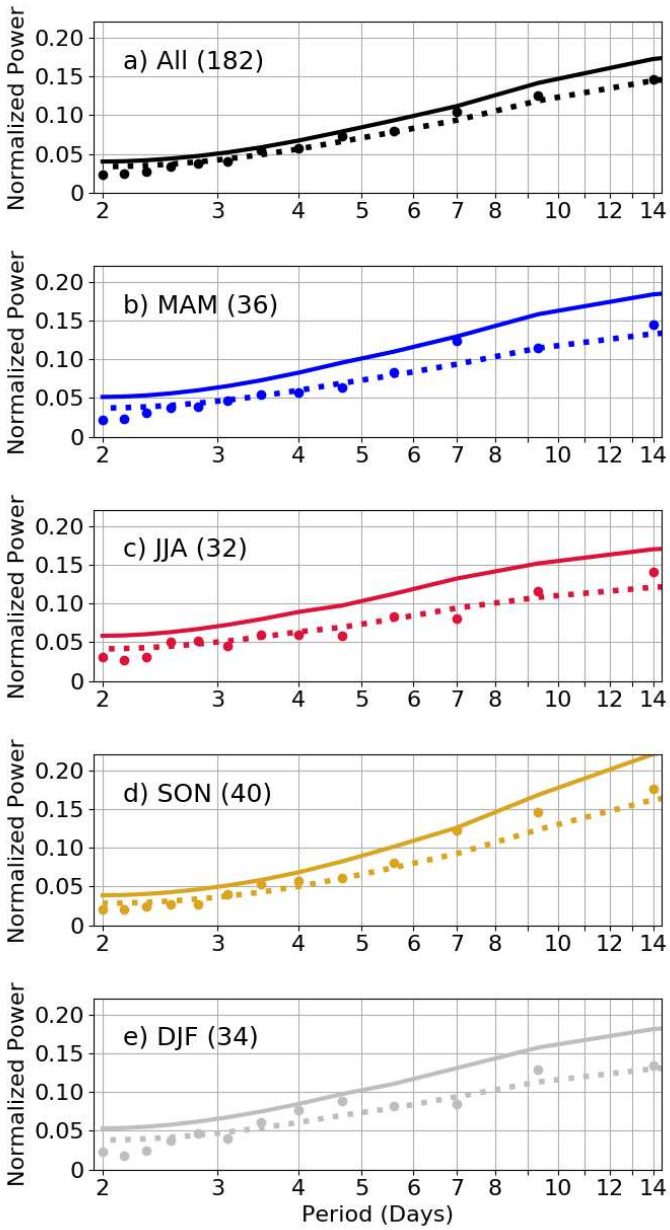

Figure 2.14. Normalized power spectra for 2-14 day cycles for the total aerosol number concentrations from the CPC for the entire period (a) and by season (b-e). The dots represent power associated with the data. The dashed lines represent an estimate of the red noise power spectrum for each data set, and the solid lines represent the 99% significance testing level, as described in the text. The values in the parentheses are the number of 28-day data chunks used in this analysis.

2.5 Conclusions

The focus of this study is on 5-year (2009-2013) measurements from several instruments located at the Department of Energy's Atmospheric Radiation Measurement's Southern Great Plains (SGP) site. These instrument datasets were merged to provide aerosol number size distributions for particles with diameters between 7 nm through ~14 μm and were also converted to surface area and volume size distributions (Marinescu et al. 2019). This quality-controlled dataset was used for two purposes. First, we provided key characteristics of the size distributions, including fits for 4 lognormal modes, both for the entire period and on a seasonal basis for the SGP site (a North American, rural, continental site). These observational data and analyses may be useful for validating models that explicitly represent aerosol processes. Furthermore, the characteristic aerosol size distributions presented in this study could also be used in a variety of applications, including more realistic representations of aerosol activation, radiation, and ice nucleation, especially in models that do not have detailed aerosol processes. Second, we quantified the variability in aerosol concentrations, with a focus on number concentrations, for a range of time scales from hourly to seasonal. Variability in the total number concentrations, as well as the integrated concentrations within specified size ranges that were associated with the different aerosol modes, was assessed.

In terms of seasonal differences, for total aerosol number concentrations (N_T), spring (MAM) and autumn (SON) had the largest mean concentrations, and winter (DJF) had the lowest mean concentrations. Summer (JJA) had the lowest variability in N_T, as compared to the other seasons, suggesting more consistent background aerosol conditions during the summer months. Comparing the integrated number concentrations within the aerosol modes, the variability in total number concentrations (N_T) was driven by the large variability in the smallest particles (N_{7-}

$_{30nm}$), which was likely related both to the presence of new particle formation events and the growth of these particles. JJA had the lowest mean concentrations of smallest particles ($N_{7\text{-}30nm}$), possibly due to a coagulation sink that was associated with the fact that JJA had the highest mean concentrations of larger particles ($N_{30\text{-}140nm}$, $N_{140\text{-}800nm}$, and N_{800nm+}). The distributions of $N_{7\text{-}30nm}$ and N_{800nm+} were more different between the seasons, as compared to $N_{30\text{-}140nm}$ and $N_{140\text{-}800nm}$. Therefore, the formation mechanisms and/or transport pathways of the smallest and largest particles have significant seasonal dependencies.

We used power spectral analyses to determine the presence of key temporal cycles, from hourly cycles through weekly cycles, within the aerosol data. A predominant 24-hour (diurnal) cycle in each season was observed for N_T, driven by concentrations of the smallest particles ($N_{7\text{-}30nm}$). Peak concentrations associated with this diurnal cycle in $N_{7\text{-}30nm}$ and N_T generally occurred in the afternoon and evening hours, with a slight seasonal shift in the timing that was associated with seasonal shifts in boundary layer development and insolation. There was also a consistent diurnal cycle in $N_{140\text{-}800nm}$ (and $V_{140\text{-}800nm}$), with peak concentrations typically occurring between 08 and 16 UTC (03 and 11 CDT) in all seasons, consistent with the prior studies that have focused on aerosol optical properties and mass concentrations and likely related to nitrate and organic aerosol mass concentrations. Because size-resolved measurements were limited to 5 years, cycles in aerosol number concentrations for longer periods (several-day to several-week cycles) were only tested for N_T, for which 10 years of observations were used. Although there was no cycle that was sufficiently consistent to pass our 99% significance testing, there were several temporal scales that exhibited enhanced power, which varied by season and were likely related to synoptic scale weather variability at SGP.

While this study provided key characteristics of aerosol size distributions at SGP and quantified the temporal variability of aerosol number concentrations within varying sizes and on a range of scales (hourly-to-seasonal), there are still uncertainties in attributing this variability to physical mechanisms, for which more in-depth analyses are required. For example, the recent New Particle Formation Study (NPFS) (Smith and McMurray, 2015; NPFS, 2017), which took place in April-May 2013 at the SGP site, was focused on understanding the pathways under which aerosol particles are formed and grow to larger sizes. Using the NPFS data, Hodshire et al. (2018) and Chen et al. (2018) presented several different growth pathways of newly formed particles during the 2013 spring period. Our study demonstrates with 5 years of observations that new particle formation and growth at SGP occur frequently throughout the year, and therefore, new particle formation and the subsequent growth pathways at SGP may be a more significant contribution to cloud condensation nuclei than previously appreciated. Classifying specific time periods when there are both consistent cycles in the data and hypotheses as to the mechanisms involved, as has been done in this study, can provide the temporal map for further detailed analyses using the wide range of instruments present at the SGP site or in future field campaigns.

CHAPTER 3: UPDRAFT VERTICAL VELOCITY OBSERVATIONS AND UNCERTAINTIES IN HIGH PLAINS SUPERCELLS USING RADIOSONDES AND RADARS

3.1 Introduction

Supercell updrafts contain some of the most intense vertical air velocities (hereafter, w_{air}) in the atmosphere (e.g., Musil et al. 1986; Lehmiller et al. 2001; DiGangi et al. 2016). The magnitude and vertical structure of w_{air} within supercell updrafts control many atmospheric processes, including the production of severe hail (e.g., Browning and Foote 1976; Heymsfield and Musil 1982) and the transport of atmospheric constituents from the boundary layer to the upper troposphere and stratosphere (e.g., Foote and Fankhauser 1973; Mullendore et al. 2005). Due to the strong vertical velocities in supercell updrafts, cloud droplets do not have enough time to grow to sizes that can be observed by most radars. Supercell updrafts can therefore be clearly identified in radar data as regions with lower reflectivity in the lower and middle tropospheric levels, laterally and vertically bounded by higher reflectivity, known initially as vaults and later as weak echo regions (WERs; Browning and Ludlam 1962; Chisholm 1970; Marwitz and Berry 1971). Despite supercell updrafts' importance for atmospheric processes, they have seldom been observed in situ.

The first of these infrequent in situ observations of the magnitudes of supercell updraft velocities came from armored aircraft penetrations through the WERs (Marwitz and Berry 1971; Heymsfield and Musil 1982). These observations were usually made near cloud base and in the inflow air ahead of the supercell, were typically taken in the High Plains of the U.S. and Canada, and generally resulted in estimates of w_{air} in the 15-30 m s^{-1} range. One research flight into the

WER of a supercell in Montana at ~7 km above mean sea level (AMSL) observed w_{air} as high as 50 ± 5 m s^{-1} (Musil et al. 1986). Despite the continued need for in situ observations of deep convection, the last U.S. storm-penetrating research aircraft was retired without replacement in 2005 (Geerts et al. 2018).

In situ estimates of updraft velocities can also be achieved via releasing sensors or trackable objects into supercell updrafts from the storm's proximity. Chaff packets have been released from aircraft at thunderstorms' cloud bases and tracked with radar to estimate vertical velocities within supercells. Results from this approach have generally been consistent with those from in situ aircraft penetrations (Marwitz 1972, 1973). Radiosondes have also been used throughout the past 50 years, albeit infrequently, to estimate the vertical velocities in supercells (Barnes 1970; Davies-Jones 1974; Davies-Jones and Henderson 1975; Bluestein et al. 1988; Bluestein et al. 1989; Marshall et al. 1995; Markowski et al. 2018). From these radiosonde observations, the greatest reported w_{air} values were 49 m s^{-1} (Bluestein et al. 1988) and 53 m s^{-1} (Markowski et al. 2018), which occurred in Texas and Oklahoma, respectively.

Due to the challenges associated with in situ observations of updrafts, such as the hazardous sampling conditions and the difficulty of placing sensors directly within the updraft core, remotely-sensed observations have replaced in situ observations as the primary estimates of w_{air} in deep convection in recent decades. The most common method for estimating w_{air} with remote sensing utilizes data from multiple Doppler radars to determine the horizontal components of the wind, and then invokes the mass continuity equation to calculate the vertical component of the wind (e.g., Armijo 1969; Miller 1975; Kropfli and Miller 1976; Gal-Chen 1978). Multi-Doppler retrievals can provide vertical velocities over a relatively large domain and are often conveniently gridded to Cartesian coordinates. However, multi-Doppler estimates also

have hard-to-characterize uncertainties due to their sensitivities to analysis specifications, such as how the data are filtered or gridded (e.g., Nelson and Brown 1987; Miller and Frederick 1998; Collis et al. 2010) or the temporal and spatial resolution of the data (e.g., Bousquet et al. 2008; Potvin et al. 2012; Oue et al. 2019). Because of their availability, these remotely-sensed observations have often been used to validate case study model simulations of deep convection in large field campaigns (Varble et al. 2014; Marinescu et al. 2016; Fan et al. 2017). These studies have shown that cloud-resolving models tend to produce stronger vertical velocities than their corresponding radar-derived estimates. However, the errors associated with multi-Doppler w_{air} are largely case-specific and depend on the radar scanning strategy, the type of convection and location of convection with respect to the radars (Oue et al. 2019). Therefore, it is still challenging to attribute the differences in updraft magnitudes from radar-based analyses and cloud-resolving models. In situ observations can thus assist in providing independent estimates of w_{air}.

In this study, we present GPS-radiosonde-based in situ observations and uncertainties of w_{air} within the updraft regions of two supercells. These observations were made during the Colorado State University Convective CLouds Outflows and UpDrafts Experiment (C^3LOUD-Ex) during 2016 and 2017 in the High Plains of Colorado, Wyoming, and Nebraska (van den Heever et al. 2020). Using the radiosonde data, along with radar observations within the C^3LOUD-Ex domain, we (1) provide our best in situ estimates of w_{air} within the two supercell updrafts, (2) contextualize and compare these observations to other available w_{air} estimates for the two cases, and (3) offer insights for future efforts towards obtaining in situ observations within supercell updrafts.

3.2 C^{3}LOUD-Ex observations

a. Radiosondes

During C^{3}LOUD-Ex, the iMet-1-ABxn radiosonde was used, which included a pressure, temperature and humidity sensor, as well as a GPS receiver (InterMet Systems 2016). The radiosonde package was attached via a dereeler (30 m length) to a 200-g balloon that was filled with enough helium to reduce the helium tank's gauge pressure by approximately 3447 kPa (500 psi). For this study, the most essential radiosonde data were from the GPS receiver, which has a horizontal position accuracy of 10 m and an altitude accuracy of 15 m. GPS positions were received from the radiosonde at a rate of 1 Hz.

Using the GPS altitude data, the vertical velocity of the radiosonde was estimated using a centered-in-time derivative:

$$w_{sonde} = \frac{\Delta z}{\Delta t} \tag{3.1}$$

where w_{sonde} is the representative vertical velocity of the radiosonde system over the time interval Δt, and Δz is the vertical distance traveled by the radiosonde during Δt. For this study, Δt is chosen to be 9 seconds, which for 10-60 m s^{-1} updrafts equates to vertical distances of 90-540 m, comparable to current numerical model simulation grid spacings and/or observational grids. The error in this w_{sonde}, denoted $\epsilon_{w,sonde}$, was calculated using error propagation methods (e.g., Palmer 1912). Because the relative error in the GPS time measurement was several orders of magnitude smaller than the error in GPS position measurement, $\epsilon_{w,GPS}$ can be simplified to the following:

$$\epsilon_{w,sonde} = |w_{sonde}| \left(\frac{\sqrt{2}\epsilon_z}{\Delta z}\right) \tag{3. 2}$$

where ϵ_z is the error in the GPS altitude from the radiosonde (15 m). For a fixed Δt = 9 s and due to the linear relationship between w_{sonde} and Δz, $\epsilon_{w,sonde}$ is always ± 2.3 m s^{-1}.

While w_{sonde} was directly observed by the radiosonde, the vertical velocity of the air that the radiosonde sampled (w_{air}) was desired. We decompose w_{sonde} into the following components:

$$w_{sonde} = w_{air} + w_{buoy} + w_{upd-drag} + w_{upd-hydro} \quad (3.3)$$

where w_{buoy} is the vertical velocity arising from the buoyancy of the radiosonde system (balloon and radiosonde) in clear-sky, still-air conditions; $w_{upd\text{-}drag}$ is the vertical velocity associated with changes to the drag force on the radiosonde system within an updraft as compared to clear, still air; and $w_{upd\text{-}hydro}$ is the forcing from hydrometeors impacting or accumulating on the radiosonde system. In this formulation, we do not consider changes to w_{sonde} due to the pendulum effects of the radiosonde, "bobbing" or self-induced motions of the balloon (e.g., Wang et al. 2009; Söder et al. 2019), nor the effects related to deviations from terminal velocity balance, because these processes occur on time scales smaller than the 9 s interval used in this study, and thus, their contributions are small. Ultimately, by observing w_{sonde}, whose uncertainty ($\epsilon_{w,sonde}$) is known, and estimating w_{buoy}, $w_{upd\text{-}drag}$, $w_{upd\text{-}hydro}$, and their associated uncertainties ($\epsilon_{w,buoy}$, $\epsilon_{w,upd-drag}$, $\epsilon_{w,upd-hydro}$), an estimate of w_{air} and its uncertainty ($\epsilon_{w,air}$) can be determined.

Implicit in these definitions is that in clear-sky, still-air conditions w_{air}, $w_{upd-drag}$, and $w_{upd-hydro}$ are all ~0 m s^{-1} and hence, $w_{sonde} = w_{buoy}$. Therefore, we estimated w_{buoy} from the w_{sonde} measurements obtained from thirteen radiosondes that were launched at the Colorado State University Foothills Campus in clear conditions with weak vertical motions throughout the troposphere. These radiosondes were launched during synoptic-scale ridges, which provided weak subsidence throughout the region. Seven launches took place overnight to minimize the influence of boundary layer vertical motions, as well as to eliminate the impacts of solar radiation on the balloon, which could affect the buoyancy of the radiosonde system (Farley 2005). Vertical profiles of w_{buoy} for the clear-sky, still-air launches are shown in Figure 3.1a. The

radiosonde descent rates (red), which occur after the radiosondes' balloons burst, vary with altitude and have a greater spread than the ascent rates (blue), which are approximately constant throughout the troposphere and lower stratosphere. Figure 3.1b shows a normalized histogram of the ascent rates from the rising radiosondes. The mean upward vertical velocity from these experiments is 4.8 m s^{-1} (w_{buoy}), with 90% of the data falling within ± 1.1 m s^{-1}, which we define here as $\epsilon_{w,buoy}$.

It is unknown whether and how the drag force on the radiosonde system within supercell updrafts differs from that in clear air, and we therefore assume that the $w_{upd\text{-}drag}$ is 0 m s^{-1} (i.e., no systematic shifts in the radiosonde-based w_{air} due to different drag forces within the updraft).

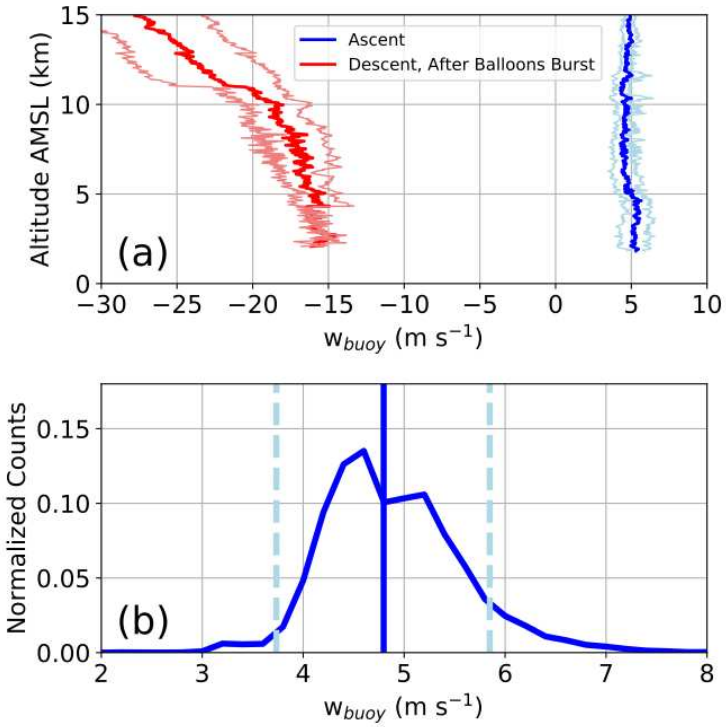

Figure 3.1. (a) Mean w_{buoy} during the clear, still air launches from ascending radiosondes (blue) and from descending radiosondes, after the balloons burst (red). Light blue and red lines represent 1 standard deviation from the mean. Data are not available for most descending radiosondes below 4.5 km AMSL. (b) Normalized histogram counts from all w_{buoy} from ascending radiosondes shown in (a), with the vertical, solid line representing the mean value (4.8 m s^{-1}) and dashed lines representing ± 1.1 m s^{-1} from the mean, between which 90% of the data falls. The bin width is 0.2 m s^{-1}.

Using the relationship between terminal velocity and the drag coefficient, however, we estimate that the uncertainty associated with variable drag forces on the radiosonde system within updraft conditions ($\epsilon_{w,upd\text{-}drag}$) is ±1.6 m s^{-1} (See Appendix 2).

The forcing from hydrometeor impacts ($w_{upd\text{-}hydro}$) will typically be downward and can be caused by collisions with or accumulation of condensate mass (e.g., riming) on the radiosonde system. Because of the uncertainties in quantifying the presence and magnitude of these processes from the data available during C^{3}LOUD-Ex, we did not attempt to estimate $w_{upd\text{-}hydro}$ or its uncertainty in this study. Therefore, the radiosonde w_{air} is expected to be most accurate in scenarios where there is little to no impact from hydrometeors on the radiosonde system (i.e., outside of regions with hydrometeors). In such situations, the radiosonde w_{air} has an uncertainty ($\epsilon_{w,air}$) of ±3.0 m s^{-1}, where $\epsilon_{w,air}$ is the summation in quadrature of $\epsilon_{w,sonde}$ (±2.3 m s^{-1}), $\epsilon_{w,buoy}$ (±1.1 m s^{-1}), and $\epsilon_{w,upd-drag}$ (±1.6 m s^{-1}), following error propagation methods. In regions with hydrometeors, however, since $w_{upd\text{-}hydro}$ is negative for a rising balloon, the radiosonde w_{air} represents a lower bound on the actual w_{air}. It is important to note here that these estimates also assume that the balloon has not burst. Using the radiosonde accelerations and the radar observations (as described in Section 3.4), we estimated the times at which the balloons burst and made adjustments for those situations to provide a more realistic estimate of w_{air}.

b. Radars

Because the radiosondes provided localized measurements within the broad supercell updrafts, we used radar data to contextualize the in situ observations. Additionally, the radar data provided an independent estimate of w_{air} using dual-Doppler methods. Three radars were primarily utilized during C^{3}LOUD-Ex: the CSU-CHILL radar (Brunkow et al. 2000), located in

Greeley, CO; the Cheyenne, WY NEXRAD (KCYS); and the Denver, CO NEXRAD (KFTG). KCYS is located ~79 km to the north of CSU-CHILL, and CSU-CHILL is located ~74 km to the north of KFTG. Plan position indicator (PPI) scans from all radars, as well as additional range height indicator (RHI) scans from CSU-CHILL, provided detailed views of the storm structure and the relative position of the radiosonde within the storms. During C^{3}LOUD-Ex, the NEXRAD radars (KCYS and KFTG) had prescribed volume coverage patterns that each lasted ~5 minutes, while the CSU-CHILL radar was manually operated and synchronized with the relevant NEXRAD radar during updraft-targeted radiosonde launches. Figure 3.2 shows an example of radar elevation angles for the NEXRAD and CSU-CHILL radars for one radar volume for the two cases examined in this study.

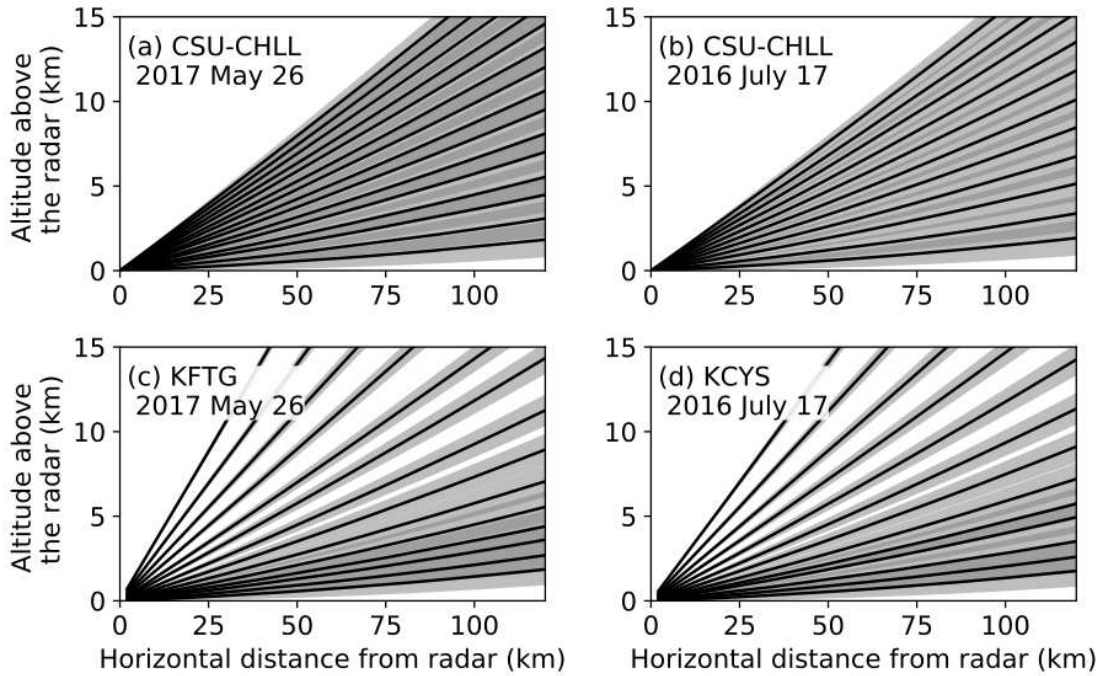

Figure 3.2. Radar elevation angles for both the CSU-CHILL (a-b) and NEXRAD (c-d) radars during dual-Doppler analysis times for the two C^{3}LOUD-Ex cases. Black lines represent the center of the beams, while gray shading represents the vertical distance covered by the beams.

Reflectivity, velocity and some dual-polarization data from all three radars were used. These radar data were first quality-controlled using the dual-polarization data. Specifically, we

excluded all radar gates where the standard deviation of the differential propagation phase was greater than 21 degrees over a range of 11 gates. We found that this threshold eliminated noise and ground clutter, while retaining more data near features of interest (e.g., the WER), which were otherwise eliminated when using correlation coefficient as a threshold. The radar velocity data were dealiased using the region-based method in the Python-ARM Radar Toolkit (Py-ART; Helmus and Collis 2016), and the storm motion for both cases was estimated for each 5-min radar volume scan using the Py-ART grid displacement algorithm on the radar reflectivity between 3 and 8 km AGL. These estimated storm motions were calculated for each radar volume and used for corrections related to storm translation in the dual-Doppler analyses, as well as for advecting the radar analyses in time for comparisons with the 1 Hz radiosonde data. Although these processing steps were largely automated, all quality-controlled and processed data were also manually checked.

Two analysis programs were then used to synthesize the radial velocity data and produce radar-based w_{air} estimates. These programs were the Custom Editing and Display of Reduced Information in Cartesian space (CEDRIC; Miller and Frederick 1998) and the Spline Analysis at Mesoscale Utilizing Radar and Aircraft Instrumentation (SAMURAI; Bell et al. 2012). While these programs both solve the basic radar equations, CEDRIC uses column-by-column vertical integration of the mass continuity equation to produce local solutions for each vertical column, while SAMURAI uses a 3D-variational approach (Gao et al. 1999) and produces a global solution for the entire analysis domain via a cost minimization function. The 3D-variational approach has been shown to produce better vertical velocity solutions for a supercell case than other methods (Potvin et al. 2012). These analyses were completed on 1-km and 500-m Cartesian grids for the 26 May 2017 and 17 July 2016 cases, respectively, due to the relative locations of

each storm with respect to the radars as shown in the following section. For the CEDRIC analyses shown here, the variational vertical integration method was used, whereby downward integration was first completed, residual errors were spread throughout the column in an iterative manner and lastly, variationally adjusted integration was applied (e.g., W_{var} in Dolan and Rutledge 2010). A linear, least-squares two-dimensional filter was also used on the horizontal winds in the CEDRIC analyses (Miller and Frederick 1998). Low-pass filters with approximate scales of 4-km and 2-km for the 1-km and 500-m Cartesian grids, respectively, were applied in the SAMURAI analyses (Ooyama 2002, Purser et al. 2003).

3.3 C^{3}LOUD-Ex cases

During C^{3}LOUD-Ex, there were 7 cases in which the updrafts of supercell storms were successfully sampled with radiosondes (van den Heever et al. 2020). In this study, we focus on the two cases that had successful radiosonde sampling of updrafts within the regions where dual-Doppler estimates of w_{air} could also be made. These occurred on 26 May 2017 and 17 July 2016 and are briefly described in the following two sections and summarized in Figure 3.3.

a. 26 May 2017 case study

At 18:15 UTC, an environmental sounding (Fig. 3.3b) was launched at 39.72 °N, 104.22 °W and showed 0-6 km shear of 26 m s^{-1}, mixed-layer (0-90 hPa AGL) convective available potential energy (MLCAPE) of 491 J kg^{-1}, and surface-based CAPE of 1882 J kg^{-1}.[4] By 20:00 UTC (UTC = local time + 6 hours), terrain-induced scattered convection was moving eastwards over the Denver metropolitan region. The destabilized boundary layer and favorable

[4] The CAPE calculations in this study are based on Bryan (2008).

environmental conditions resulted in the development of an isolated supercell by 22:00 UTC, located within the dual-Doppler analysis region for the CSU-CHILL and KFTG radars (Fig. 3.3a). At 21:58 UTC, a radiosonde (2017-1) was launched and sampled the updraft of the developing supercell, while 1.5 inch (3.8 cm) diameter hail was reported at the surface nearby (NCEI 2017). Around 22:00 UTC, the storm propagation slowed and took a rightward turn

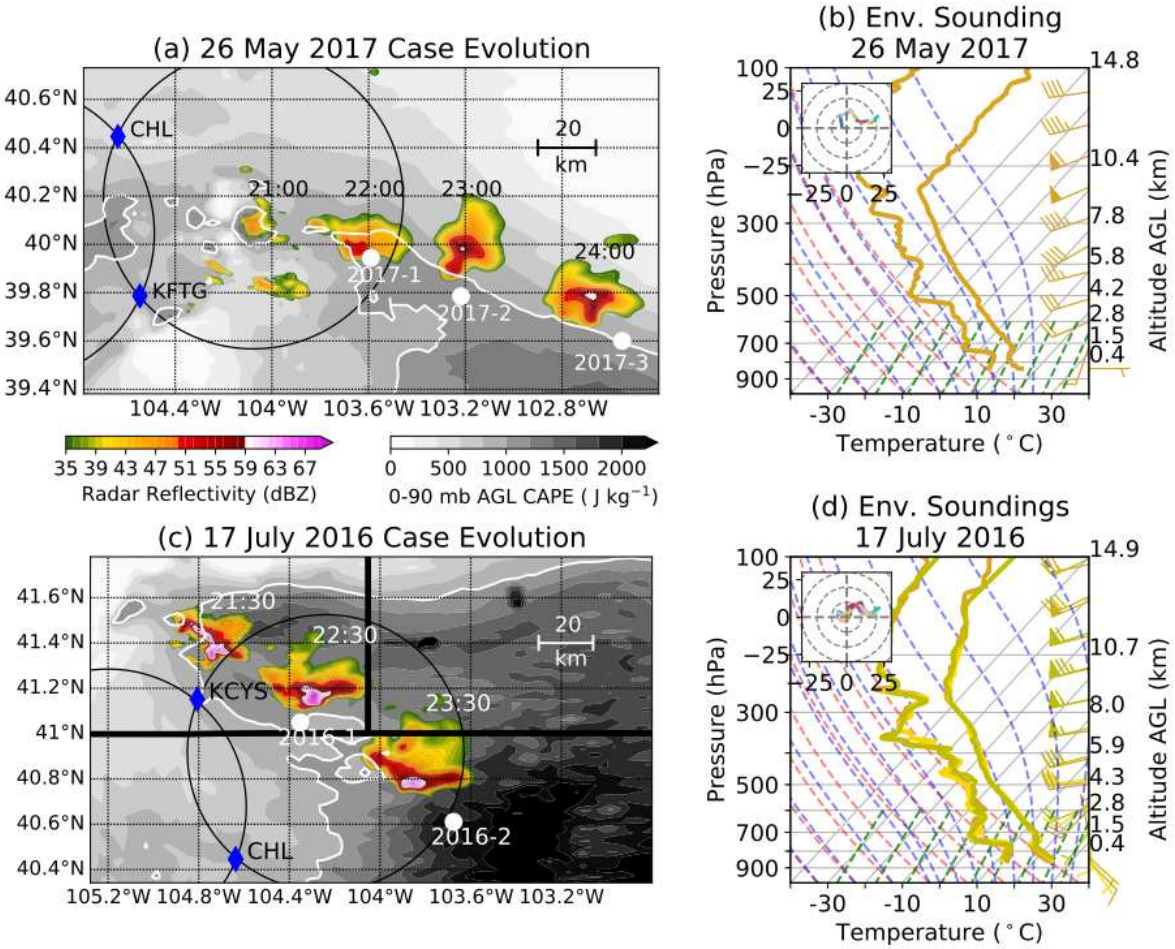

Figure 3.3. Case evolution and environmental soundings from the 2017 case (top row), and the 2016 case (bottom row). The white dots represent updraft radiosonde launch locations. The blue diamonds are the radar locations, and non-overlapping regions of the black circles indicate where dual-Doppler analyses are possible. The color shading shows radar reflectivity at 1 km AGL at the approximate time of radiosonde launch. The gray shading represents MLCAPE from the 21:00 UTC operational simulation of High Resolution Rapid Refresh (HRRR) model for both cases; 1000 J kg^{-1} is contoured in white. The right column shows skew T – log p diagrams of the environmental radiosonde launches as described in the text. Hodographs are inlaid and the different colors within the hodographs represent 500-m increases in altitude from the surface to 6 km AGL.

towards the east-southeast. Over the next several hours, many instances of hail with diameters of 1-1.5 inches (2.5-3.8 cm) were reported at the ground along the storm's path, as were 2 weak tornadoes (NCEI 2017). Two additional radiosondes (2017-2 and 2017-3) sampled the supercell updraft between 22:00 and 24:00 UTC. This long-lived supercell continued into Kansas, outside of the C^{3}LOUD-Ex became part of a mesoscale convective system.

b. 17 July 2016 case study

On 17 July 2016 at ~20:30 UTC, convection that had initiated over the high terrain of southern Wyoming moved eastward onto the high plains to the northwest of Cheyenne, Wyoming, where it quickly organized into a supercell and subsequently turned towards the southeast (Fig. 3.3c). Earlier in the day, between 18:00 and 19:00 UTC, three radiosondes were launched (at 40.67 °N, 104.33 °W; 41.22 °N, 104.35 °W; and 41.24 °N, 103.70 °W) to better capture the environment ahead of this storm. These observations (Fig. 3.3d) indicate MLCAPE of ~950-1200 J kg^{-1} and 0-6 km shear of 21-25 m s^{-1}. This supercell propagated southeastward across the C^{3}LOUD-Ex domain, including through the region where dual-Doppler analyses could be conducted using the CSU-CHILL and KCYS radars. This storm had more intense radar reflectivity than did the 2017 case, and there were several reports of 2.0-inch (5.1-cm) diameter hail as well as a few baseball-sized hailstones (diameters of ~7.5 cm; NCEI 2016). As the supercell propagated southeastward, two radiosondes were launched into the supercell's main updraft region (Fig. 3.3c). The first, 2016-1, was located within the dual-Doppler analysis region, while the second, 2016-2, was just outside the dual-Doppler lobes in a more unstable environment. By 01:30 UTC on 18 July 2016, the storm began to lose many of its supercellular characteristics, and it dissipated by 03:00 UTC.

We note here that both of these High Plains supercells experienced environments with substantial vertical wind shear (0-6 km; ~21-26 m s^{-1}) and moderate MLCAPE (~1000-1600 J kg^{-1}). These environments had bulk Richardson numbers of ~10-15, well within the range favorable for supercells (Weisman and Klemp 1982), although the MLCAPE values are on the lower end of those conditions supporting weakly-tornadic and non-tornadic supercells within the broader United States (Thompson et al. 2003). Therefore, these C^3LOUD-Ex observations of w_{air} will likely be lower than similar observations of supercells in more unstable air masses, such as those present in the U.S. southern Great Plains.

3.4 Radiosonde-derived updraft vertical velocities (w_{air})

The w_{air} estimated from the 5 radiosondes that sampled the two supercells' updrafts are shown in Figure 3.4, which for simplicity's sake only depicts w_{air} from when the radiosonde was launched to when the radiosonde reached its maximum altitude. These data represent point locations within the large supercell updrafts. Thus, radar data were essential for determining the position of the radiosonde within the updraft and elucidating whether each radiosonde was likely to have sampled the strongest w_{air} within these storms. The radiosondes took many different trajectories throughout the supercells. Only one of these five radiosondes (2017-2) continued to rise into the stratosphere after sampling the supercell updraft. The other radiosonde systems likely experienced conditions within the updraft that robbed them of their positive buoyancy (e.g., radiosonde balloon bursting or significant riming). In order to identify these events, the radiosonde-derived accelerations were calculated from w_{air} and were examined for the entirety of the radiosondes' data transmissions (Fig. 3.5). A 5-second moving average was then applied to data to eliminate noise but still capture significant events. The most intense negative

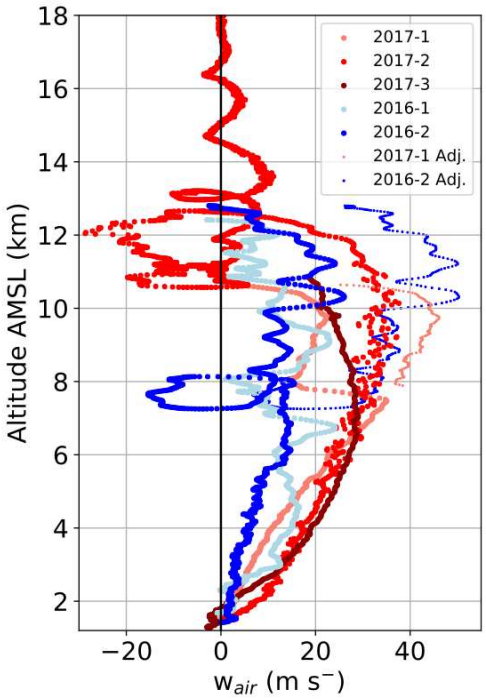

Figure 3.4. Radiosonde w_{air} from radiosondes that sampled the two C^{3}LOUD-Ex supercell updrafts. Data are only shown from the radiosondes' launch times through to when the radiosondes reached their maximum altitudes. The smaller dots for 2017-1 and 2016-2 represent w_{air} adjusted for a burst radiosonde balloon (see Fig. 5).

accelerations were likely associated with the radiosonde balloon bursting, whereby w_{buoy} instantaneously changed from approximately +4.8 m s^{-1} to anywhere between -15 to -25 m s^{-1}, depending on the radiosonde's tropospheric altitude (Fig. 3.1a). The most intense negative accelerations are highlighted in yellow in Figure 3.5 and had values between -1.9 and -5.1 m s^{-2}. These values were similar to those associated with the radiosonde balloon bursting during the clear-sky, still-air launches, which all occurred above 16 km AMSL and ranged from -2.5 to -5.5 m s^{-2} (not shown). For radiosondes 2017-2 and 2016-1, the radiosondes' balloons did not burst until right before their final descents to the surface. However, for radiosondes 2017-1, 2017-3, and 2016-2, it appears that the balloon burst within the radiosonde's initial ascent through the updraft. As will be shown in the following sections, radar data suggest that the radiosondes were entering regions of large hail at these estimated burst times and altitudes. Therefore, for

radiosondes 2017-1 and 2016-2, adjustments were made to the radiosonde-derived w_{air} after the balloon burst (Fig. 3.4, smaller dots), taking into account the altitude-dependent, mean terminal velocities of the descending radiosonde system (Fig. 3.1a). For radiosonde 2017-3, data were unavailable after the balloon burst; therefore, no adjustments were necessary.

Before the adjustments described above, the maximum w_{air} values measured by the radiosondes for the 2017 and 2016 cases were 37.6 and 26.1 m s^{-1}, respectively. After the

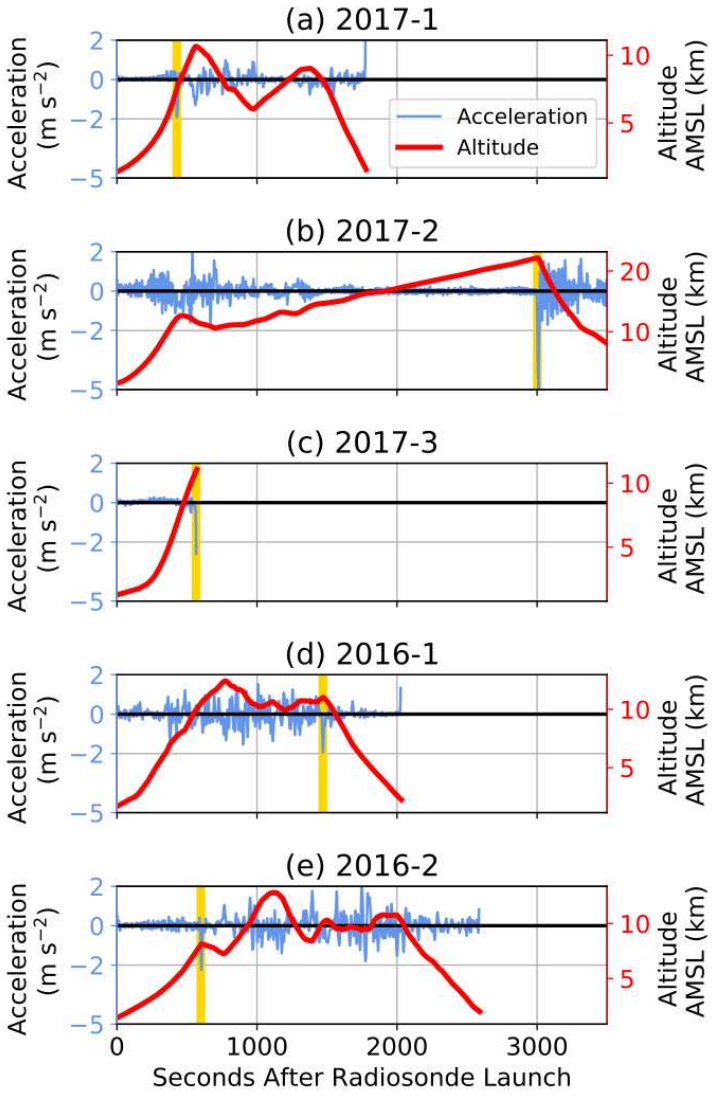

Figure 3.5. Radiosonde accelerations from each launch (blue, left axis) and radiosonde altitude (red, right axis) as a function of seconds since launch. Yellow vertical lines indicate the strongest negative accelerations, likely associated with the radiosonde balloon bursting.

adjustments, the respective maximum radiosonde w_{air} values were 46.1 and 50.3 m s^{-1}. However, due to the large spread associated with the terminal velocities of radiosondes following balloon bursting (Fig. 3.1a), additional testing would be needed to develop the uncertainties for the adjusted w_{air} estimates. In the next sections, we present the radiosonde w_{air} for each launch in the context of the radar data.

a. 2017 case

Radiosonde 2017-1 was launched at 21:58 UTC, shortly after the supercell formed and within the dual-Doppler analysis region for the CSU-CHILL and KFTG radars. Figure 3.6 depicts the radiosonde w_{air} along with two snapshots of the radiosonde position within the storm based on the radar reflectivity and dual-Doppler-derived w_{air}. Based on the radiosonde humidity data, the radiosonde entered cloud around 2.7 km AMSL, at which point $w_{air,}$ the updraft vertical velocity, was 5.5 m s^{-1}. This corresponds to an average rate of acceleration from the ground level to cloud base of 0.034 m s^{-2}. The radiosonde continued to accelerate within the cloudy updraft through ~7.5 km AMSL at an average rate of 0.086 m s^{-2}, more than double the rate below cloud base.

During this time period, the radiosonde was located within the main updraft, along the western edge of the weak echo region. At 7.5 km AMSL (Fig. 3.6b-g), the radiosonde decelerated for ~15-20 s as it entered a region of higher reflectivity (>50 dBZ) and low correlation coefficients (<0.9, not shown), suggesting large hail (e.g., Balakrishnan and Zrnic 1990; Rhyzkov et al. 2013). At this point in time, both dual-Doppler analyses (Fig. 3.6e,g) demonstrate increasing w_{air} with height, which would suggest positive balloon acceleration, not negative. This corroborates our hypothesis that the balloon most likely burst. As such, above 7.5

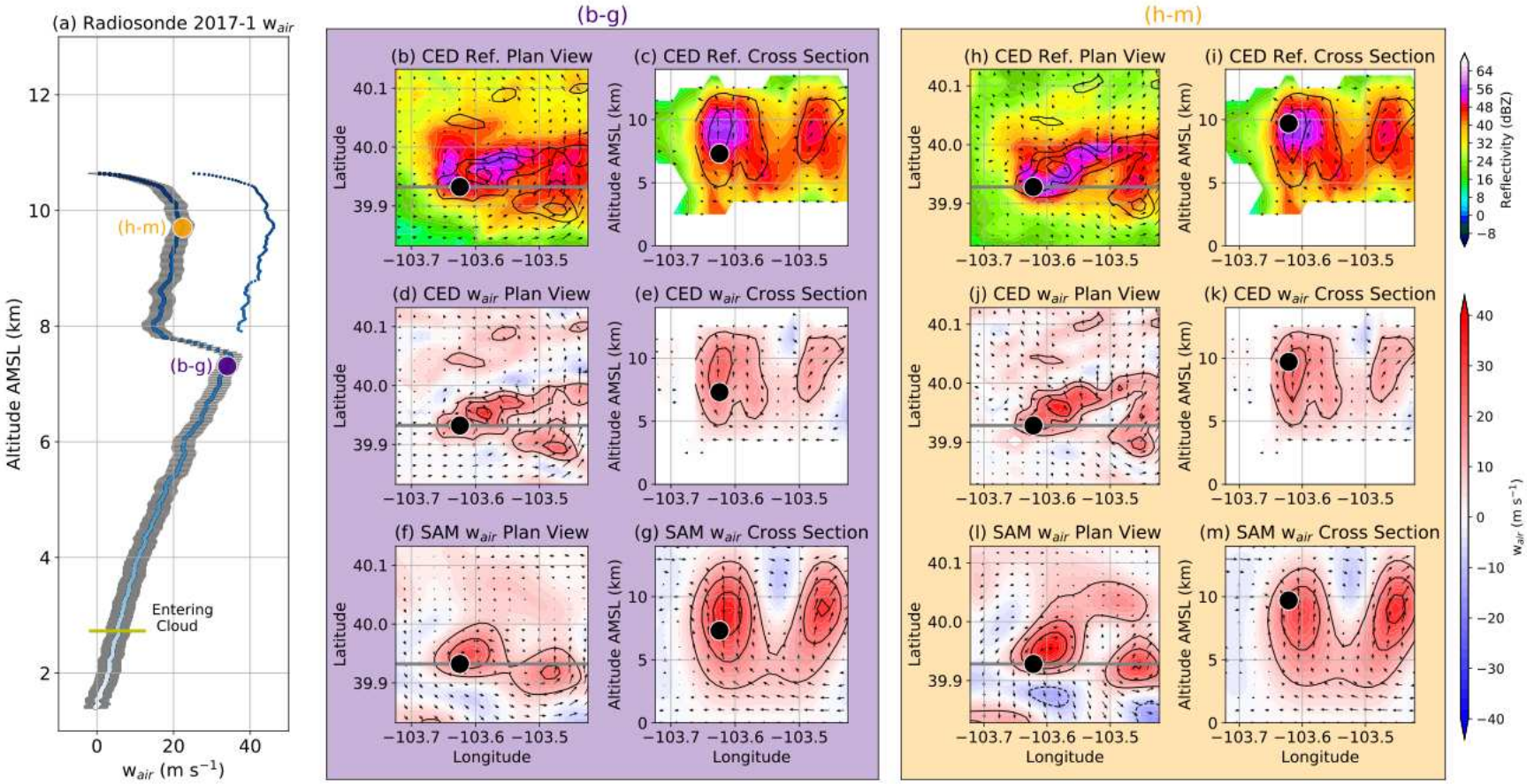

Figure 3.6. (a) Radiosonde w_{air} for the 2017-1 launch with uncertainty estimates (gray). The shading from light to dark blue represents the time evolution of the radiosonde from launch to maximum altitude. The smaller dots take into account adjustments, assuming the radiosonde balloon burst. (b-m) demonstrate the position of the radiosonde (black dots) within the storm at two different times during the radiosonde ascent. The top row shows radar reflectivity plan views and vertical cross sections, as denoted by the grey lines in the plan views. The middle row shows the plan views and cross sections of CEDRIC w_{air}, while the bottom row shows SAMURAI w_{air}. The arrows represent storm-relative winds in their respective planes, and black contours indicate 10 m s^{-1} intervals of w_{air}, excluding the 0 m s^{-1} contour.

km AMSL, adjustments were made to the w_{air} estimates using a w_{sonde} corresponding to a burst radiosonde balloon, as described in the prior section. At 9.7 km AMSL (Fig. 3.6h-m), the w_{air} after adjustments reached its peak value (46.1 m s^{-1}). At this time, the radiosonde was within the primary updraft region but was nevertheless located ~5 km to the southwest of the most intense radar-derived updrafts (Fig. 3.6j,l), suggesting that the maximum w_{air} in this storm was likely even higher than that estimated from the radiosonde. We note that the adjusted radiosonde w_{air} values are more intense than those from the radar analyses, and the w_{air} estimates from the different observing platforms are compared in Section 3.5a. The radiosonde reached its maximum altitude of 10.6 km AMSL and began to descend through the updraft periphery, where the w_{air} was no longer strong enough to suspend the radiosonde system.

Approximately 1 hour later (22:51 UTC), another radiosonde (2017-2) was launched into the supercell updraft. Although the supercell was no longer within the region where dual-Doppler estimates could be made, both radar RHIs (not shown) and PPIs were used to contextualize the radiosonde measurements. Figure 3.7 shows PPI snapshots throughout the radiosonde trajectory at times when the radiosonde location was simultaneously sampled by one of the radars. The 2017-2 radiosonde was launched to the southwest of the WER (Fig. 3.7b), and accelerated to ~14 m s^{-1} before entering the cloud at 3.7 km AMSL, which was above cloud base. A maximum w_{air} of 37.6 m s^{-1} was obtained at approximately 10.1 km AMSL (Fig. 3.7e). Despite observing strong w_{air} throughout its trajectory, the radiosonde was consistently located ~5-10 km to the southwest of where the strongest w_{air} was likely located: the WER in the lower and middle troposphere (Fig. 3.7c,d) and the higher reflectivity regions in the upper troposphere (Fig. 3.7e). After reaching the top of the storm, the radiosonde underwent negative acceleration and sampled a minimum w_{air} of -28.7 m s^{-1}, which was likely associated with strong downdrafts

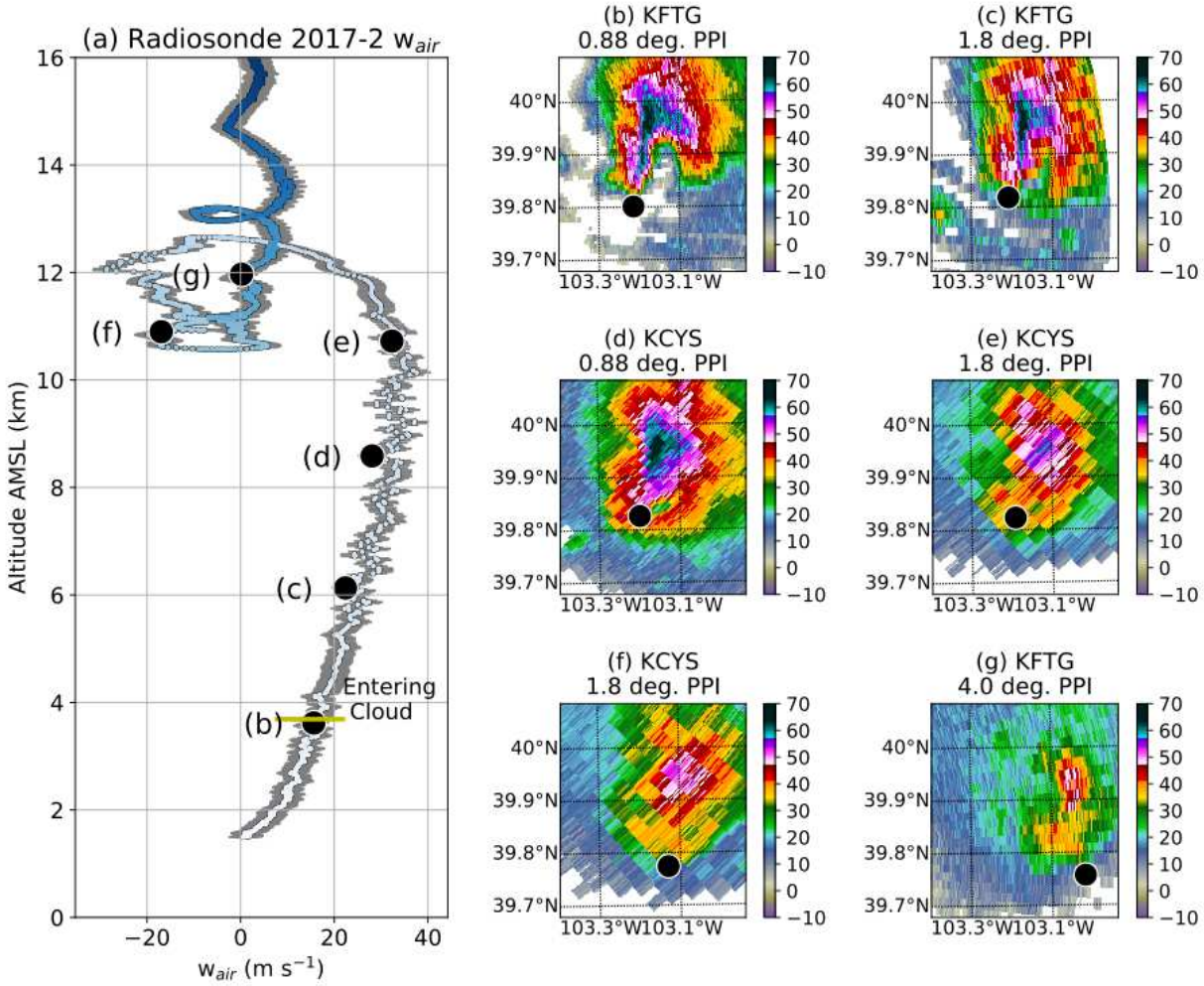

Figure 3.7. Radiosonde-derived w_{air} for the 2017-2 launch with uncertainty estimates (gray). The shading from light to dark blue represents the time evolution of the radiosonde from launch to maximum altitude. Panels (b-g) represents PPI scans of radar reflectivity that overlapped with the radiosonde within a 15 second window and within 500 m of the radiosonde's position, as labeled in panel (a).

south of the main updraft (Fig. 3.7f). Unlike the 2017-1 radiosonde, 2017-2 eventually exited the storm (Fig. 3.7g) and rose to an altitude of 22.2 km AMSL before the radiosonde balloon burst.

At 23:59 UTC, a third radiosonde (2017-3; Fig. 3.8) was launched and subsequently sampled the WER in the middle troposphere (Fig. 3.8b,c). This radiosonde experienced the strongest vertical velocities between the surface and 6.8 km AMSL of all three radiosondes from this case, accelerating at an average rate of 0.113 m s^{-2} from 4.6 m s^{-1} at 2 km AMSL to a maximum w_{air} of 31.3 m s^{-1} at 7.0 km AMSL. Unfortunately, the thermodynamic sensors were

compromised during the radiosonde launch, and thus it is unclear at exactly which point the radiosonde entered cloudy conditions. Above 7.0 km AMSL, the radiosonde began to decelerate and likely encountered rain and/or hail (Fig. 3.8a,d); communication with the radiosonde was lost at 10.8 km AMSL.

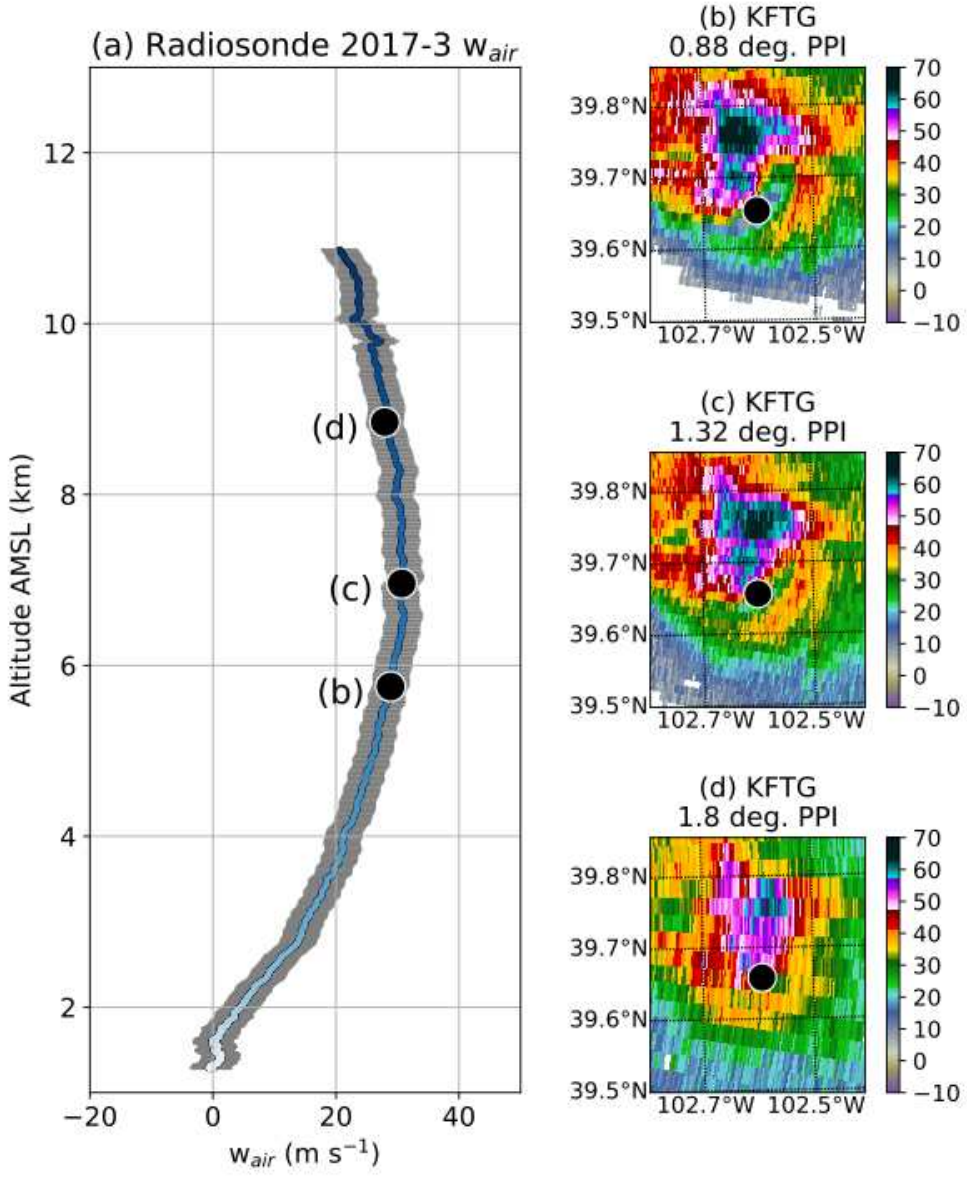

Figure 3.8. Same as Figure 3.7, but for the 2017-3 radiosonde launch.

b. 2016 case

Similar analyses were conducted for radiosondes 2016-1 and 2016-2 for the isolated supercell that occurred on 17 July 2016. Because the supercell passed closer to the radar network (Fig. 3.3c), the dual-Doppler analyses were conducted with 500 m grid spacing, which allowed for a more detailed structure in the w_{air} values.

At 22:24 UTC, the 2016-1 radiosonde (Figs. 9-10) was launched on the southern side of the supercell, shortly after the cold pool associated with the rear flank downdraft passed the launch location, resulting in negative w_{air} near the surface (Fig. 3.9a). A radiosonde-based w_{air} of ~24 m s^{-1} was observed twice during the radiosonde's ascent through the storm (at 6.7 km and 9.1 km AMSL; Fig. 3.9). In both instances, the radiosonde was in the extreme southwest edge of the updraft region, and ~10 km to the west of the WER (Fig. 3.9b-c; Fig. 3.9h-i). The radiosonde continued to rise above 12 km AMSL and then underwent a 2.5 km descent, during which it observed a minimum w_{air} of -27.0 m s^{-1} (Fig. 3.10b-g). This radiosonde, however, experienced its most intense negative acceleration immediately before the radiosonde's final descent to the surface (Fig. 3.5d), and therefore, this first radiosonde descent was likely associated with nearby, strong upper-level downdrafts that were diagnosed by both dual-Doppler analyses (Fig. 3.10d-g) rather than with the balloon bursting. The radiosonde then experienced several vertical oscillations, ascending and descending 3 times around 10-11 km AMSL and ~15 km to the southeast of the main updraft (Fig. 3.10h-m). These oscillations were likely associated with gravity waves in the cloud anvil, which are evident in the CEDRIC analyses (Fig. 3.10j-k), but less so in the SAMURAI analyses (Fig. 3.10l-m) due to the filtering scales and different approaches used (Section 3.2b). The relatively weak vertical motions in the anvil (Fig. 3.10j-m) would not have been strong enough to suspend the radiosonde had the balloon burst, providing

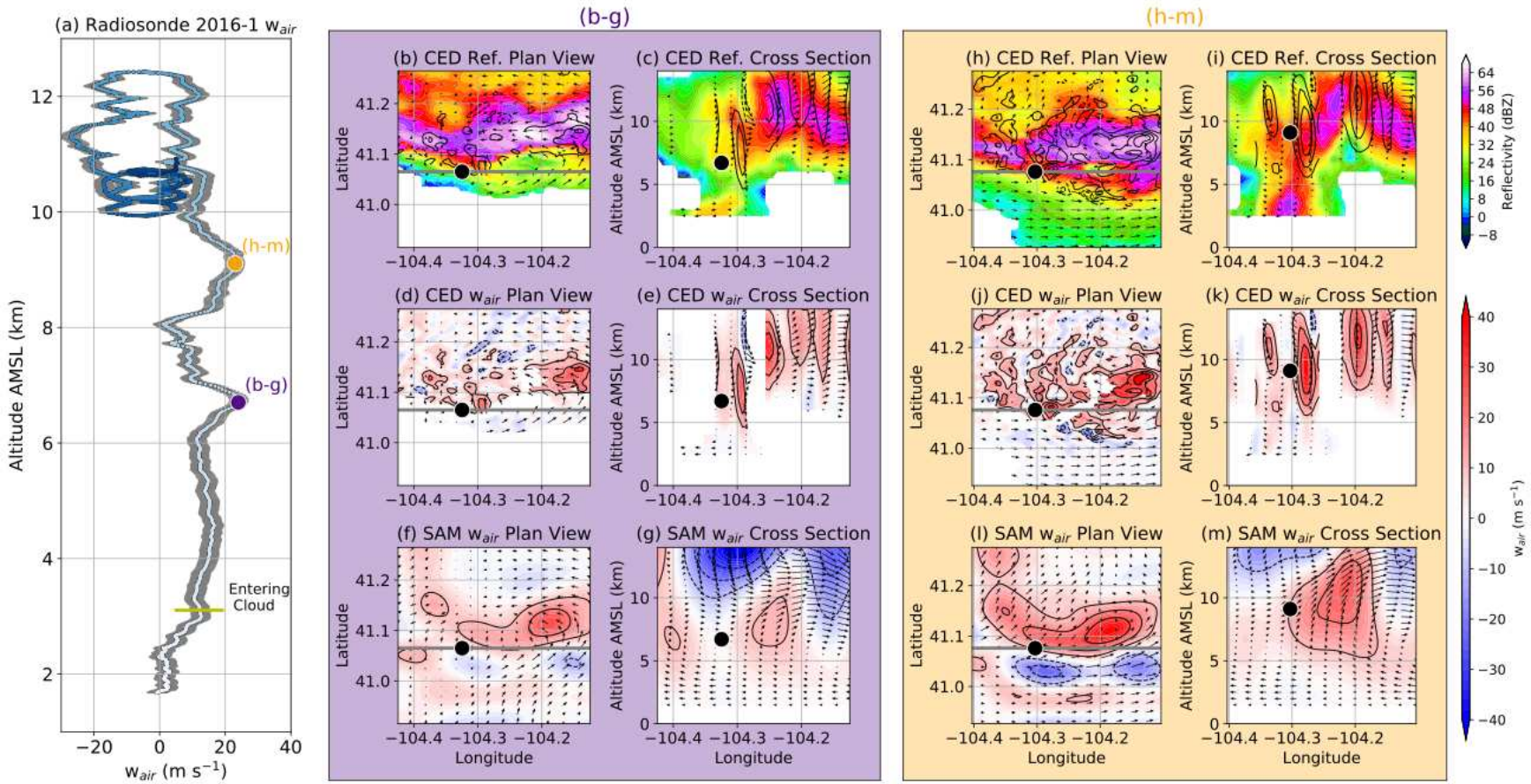

Figure 3.9. Same as Figure 3.6 but for the radiosonde 2016-1 data. The light blue to dark blue shading in (a) represents the progression of time from launch to when the balloon likely burst.

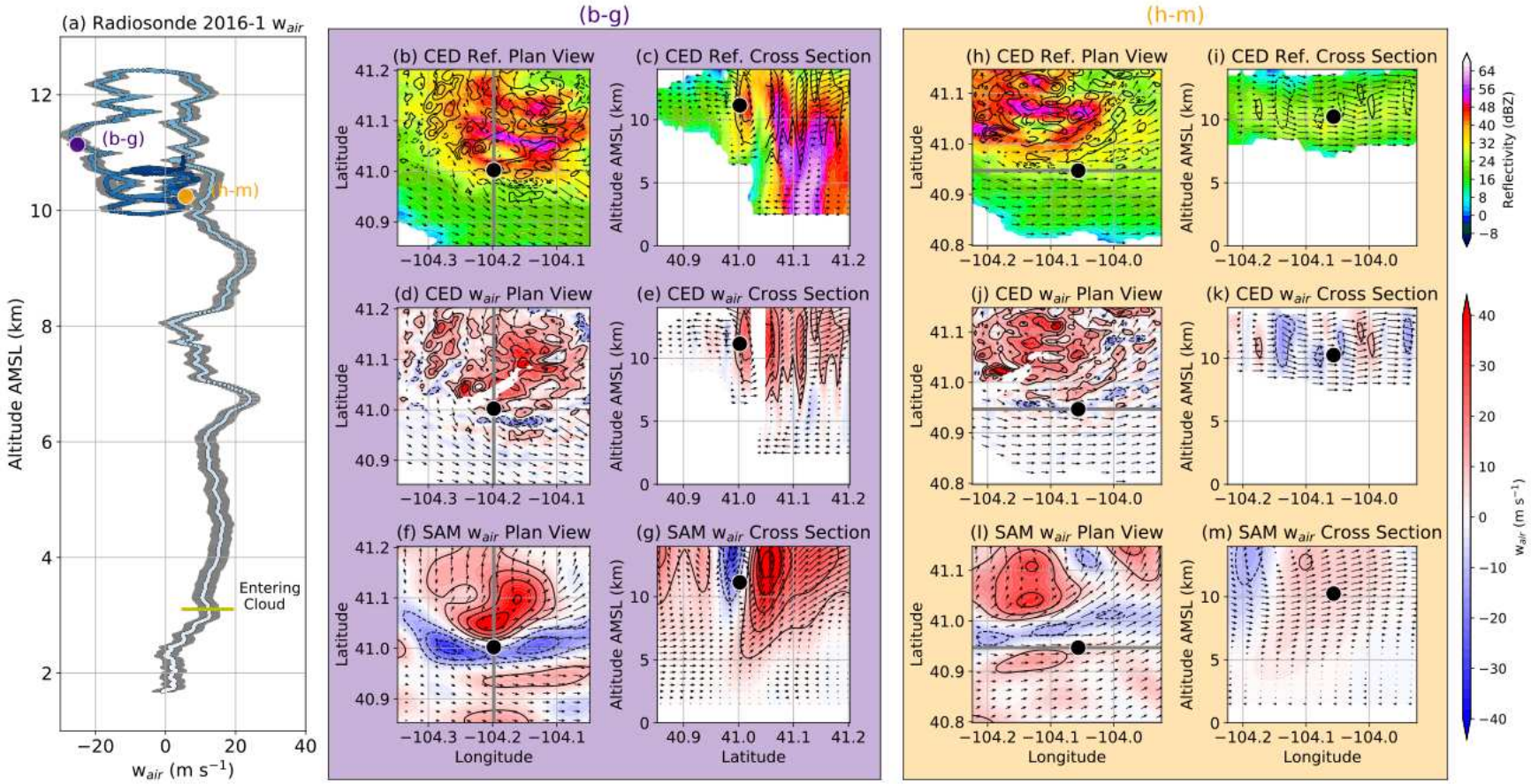

Figure 3.10. Same as Figure 3.6 and Figure 3.9, but for two later times during the progression of radiosonde 2016-1.

further evidence that the balloon did not burst until right before the radiosonde's final descent to the surface.

At 23:41 UTC, radiosonde 2016-2 was launched to the south of the WER (Fig. 3.11b) and was likely closer to the regions with the most intense vertical motions than was radiosonde 2016-1. At 8 km AMSL, however, the radiosonde experienced its most intense negative acceleration (Fig. 3.11a,c, Fig. 3.5e) while the radiosonde was entering a region to the north with high reflectivity (> 50 dBZ) and correlation coefficients < 0.94, which suggests large hail. Based

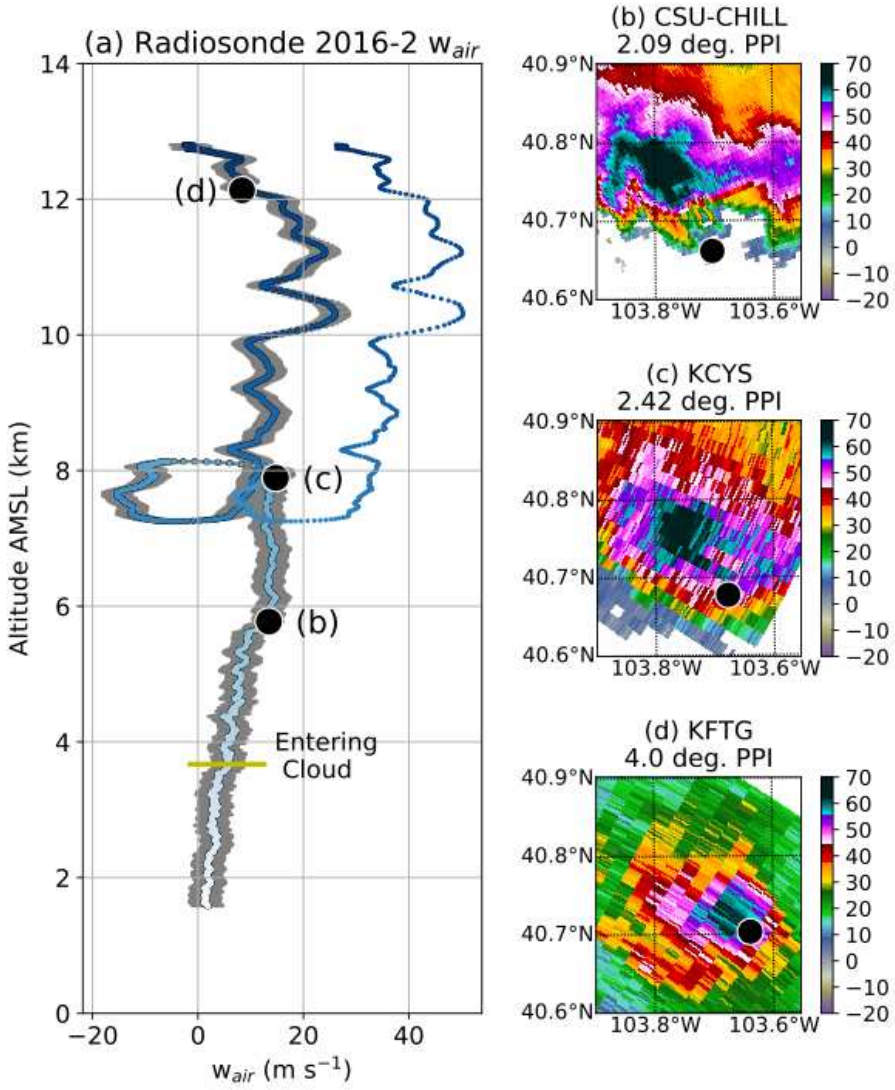

Figure 3.11. Same as Figure 3.7 and Figure 3.8, but for radiosonde 2016-2. The smaller dots take into account adjustments assuming that the radiosonde balloon burst.

on this evidence, it is likely that the balloon burst at this time, and subsequent adjustments were made to w_{air}. The radiosonde measured a maximum estimated w_{air} of 50.3 m s^{-1} at 10.3 km AMSL (Fig. 3.11a). Shortly after this maximum value was reached, the radiosonde was located within the region of maximum reflectivity at 12.1 km AMSL (Fig. 3.11d). This suggests that the radiosonde was near some of the storm's most intense vertical motions, which were able to loft large hydrometeors to these near-tropopause heights. Considering the assumptions and adjustments for balloon bursting, 50.3 m s^{-1} was the strongest vertical velocity observed by a radiosonde from these two C^3LOUD-Ex cases, and when considering the impacts of hydrometeors, this value could be even larger. This result is consistent with the fact that this radiosonde was launched in the most unstable (i.e., highest CAPE) environment of all the radiosondes (Fig. 3.3c; Table 3.1), as will be discussed in Section 3.5b.

3.5 Comparisons of radiosonde w_{air} to other platforms

a. Comparisons with dual-Doppler estimates

In addition to contextualizing the radiosonde observations, the radar data also provide an independent estimate of w_{air} for radiosondes 2017-1 and 2016-1. It is important to note the differences in the features that the two types of observing systems can resolve. The values in the dual-Doppler analyses represent the *average* vertical velocity over a cube with side lengths of 1 km (500 m) for the 2017 (2016) case using data collected over a 5-minute interval. The radiosonde values, however, represent averages along a slantwise path corresponding to the radiosonde trajectory over the course of the 9 s averaging period (e.g., horizontal and vertical distances generally between 100 and 500 m). Such differences need to be considered when comparing these estimates of vertical velocity obtained using these different platforms.

A comparison of radiosonde w_{air} with the dual-Doppler w_{air} from SAMURAI and CEDRIC is shown in Figure 3.12. The dual-Doppler analyses for each radar volume were calculated at the volume-scan midpoint time and were advected in time using the calculated storm motion for each radar volume to create a 4D dataset. These 4D data were interpolated in time and space to the same position as the radiosonde for this comparison. To account for shifts in position within the dual-Doppler analyses that may be due to small advection errors, we also show the range of values in the surrounding grid boxes that are 1 km from the radiosonde location in the horizontal plane. This spread does not, however, represent any underlying uncertainty in the radar dual-Doppler analyses, which would require additional observation system simulation experiments (OSSEs; e.g., Potvin et al. 2012; Oue et al. 2019; Dahl et al. 2019).

Comparisons cannot be made below 3.7 km AMSL (Fig. 3.12a) and 6.0 km AMSL (Fig. 3.12b) for the 2017 and 2016 cases, respectively, due to the lack of quality radar data at the radiosonde locations. This demonstrates one benefit of the radiosonde observations, namely their ability to sample vertical motions where radars only observe very low signal-to-noise ratios, such as below cloud base and along cloud edges. Based on the C^3LOUD-Ex radiosonde observations, w_{air} can approach 20 m s^{-1} in these regions.

Both dual-Doppler analyses show consistent trends and similar magnitudes of w_{air}. In both cases and for both dual-Doppler analyses, at the locations where the radiosondes observe the strongest w_{air}, the dual-Doppler w_{air} values was generally 15-20 m s^{-1} less than those derived from the radiosondes. For radiosonde 2017-1 (Fig. 3.12a), right before the balloon likely burst at 7.5 km AMSL, the difference between the radiosonde w_{air} and those of both dual-Doppler analyses was ~15-20 m s^{-1}. For radiosonde 2016-1 (Fig. 3.12b), similar differences were present

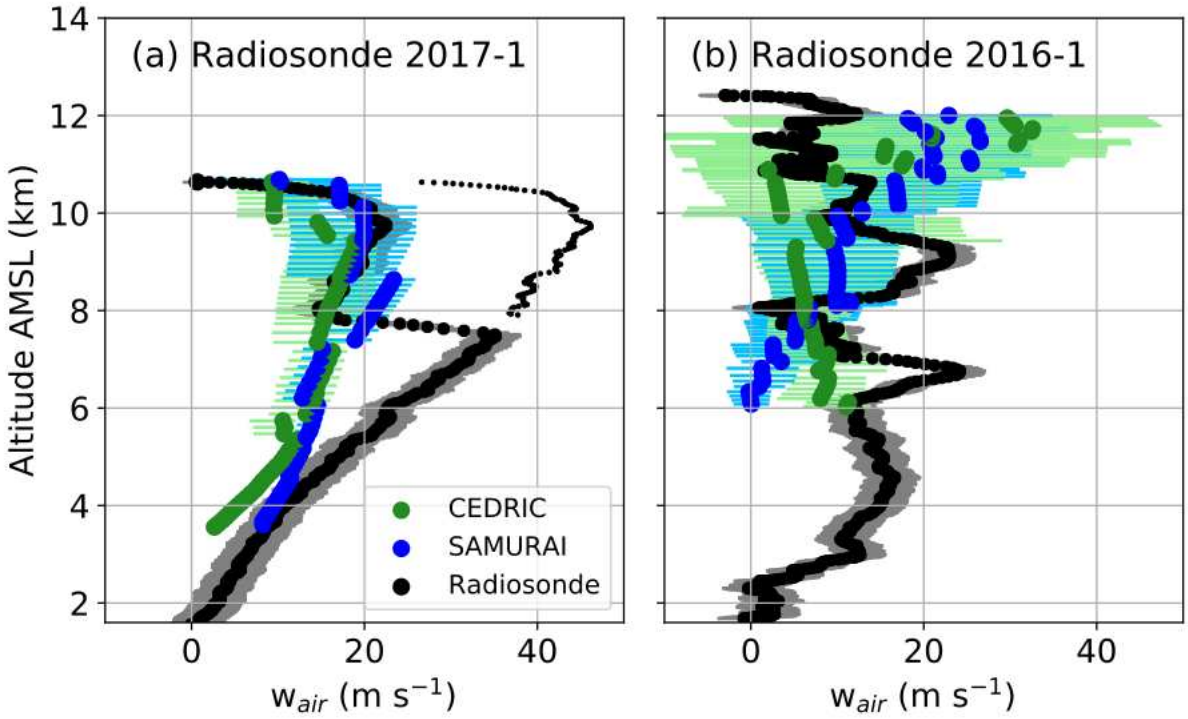

Figure 3.12. Comparison of radiosonde and dual-Doppler w_{air} for radiosondes (a) 2017-1 and (b) 2016-1, as described in the text. The gray range for the radiosonde data represents the quantified uncertainty in w_{air}. The green and blue dots represent the radar dual-Doppler analyses interpolated to the radiosonde position. The green and blue horizontal lines represent the range of values within 1 km in the horizontal direction of the radiosonde position within the dual-Doppler analyses.

at 6.7 and 9.1 km AMSL. This dual-Doppler underestimation of w_{air} as compared to the most intense radiosonde w_{air} was at least partly due to the radiosonde capturing localized features that were unable to be resolved by the resolution of these radar analyses. However, without a detailed error estimation of the dual-Doppler syntheses obtained from OSSEs for these cases, we are unable to quantify how much of the differences are due to errors associated with the C^3LOUD-Ex radar network and scanning patterns (e.g., Oue et al. 2019) versus systematic differences in the observed quantities. Regardless, this comparison does demonstrate that a comprehensive analysis of w_{air} would benefit from in situ measurements that can better capture highly localized conditions.

b. Comparisons with simple parcel theory

Parcel theory can also be used to estimate the theoretical maximum possible vertical velocity due to its relationship with CAPE (e.g., Weisman and Klemp 1984):

$$w_{MLCAPE} = \sqrt{2 \cdot MLCAPE} \tag{3.4}$$

MLCAPE is chosen, as compared to other CAPE variants (e.g., surface-based or most-unstable), because it more realistically represents the air entering deep convective updrafts. The expression shown in Eq. 3.4 assumes that vertical accelerations are only forced by buoyancy and does not account for the negative impacts from condensate loading and entrainment. Eq. 3.4 also does not consider the impacts of perturbation pressure gradients, which have been shown to decelerate updrafts within the upper levels of supercells where the maximum vertical velocities are achieved (Peters et al. 2019). Therefore, Eq. 3.4 likely overestimates the maximum vertical velocities in supercell updrafts.

To assess Eq. 3.4 with respect to the C^{3}LOUD-Ex observations, MLCAPE (0-90 hPa AGL) is calculated for each radiosonde launch. These calculations assume pseudoadiabatic ascent and account for the latent heating associated with freezing above the 0 °C level by assuming that ice fraction linearly increases from 0 °C to -40 °C. While the sub-cloud-layer radiosonde data sampled by the updraft radiosondes are generally representative of the environmental air entering the supercell updraft, the data within the cloudy updraft are no longer representative of the environmental conditions needed to estimate MLCAPE. Therefore, the thermodynamic data from lowest levels of the updraft soundings were merged with data from the middle and upper levels of the environmental soundings (Fig 3b,d). This concatenation occurred at the altitude where the temperature profiles first overlapped for each pair of soundings, near the inversion of the environmental sounding between 700 and 800 hPa. In cases where the

radiosonde was launched in a cold pool or the thermodynamic data were not available (radiosondes 2016-1, 2017-1, and 2017-3), the closest, representative radiosonde launch in time and space was used as a better estimate of the inflow air for that radiosonde launch, since we are interested in estimating the theoretical maximum vertical velocities.

Overall, the w_{MLCAPE} values calculated via parcel theory were larger than the w_{air} values observed by the radiosondes (Table 1). Further, these results highlight the variability of w_{air} within the primary supercell updraft. The percentage differences between w_{air} and w_{MLCAPE} range from -10% to -55%, largely due to the variability in the positions sampled within the supercell updrafts. The radiosonde with the largest difference (-55%, 2016-1) sampled the extreme western edge of the primary updraft, ~10 km from the WER (Fig. 3.9). The radiosonde with the smallest difference (-10%, 2017-1) sampled close to where the most intense vertical motions were likely located (Fig. 3.6). While the maximum vertical velocities estimated from these radiosonde data do not reach their theoretical maxima, as predicted by Eq. 3.4, a larger sample of observations, especially those similar to radiosonde 2017-1 that sampled near the most intense w_{air}, is needed to better observationally assess the relationship shown in Eq. 3.4.

3.6 Implications for future in situ observations of w_{air} within storms

This study has shown that GPS sensors aboard radiosondes can provide useful in situ observations of w_{air} within storms, especially when used in conjunction with radar data. Understanding the position within the updraft being sampled by the radiosonde provided invaluable context for interpreting the radiosonde observations. Particularly with GPS radiosondes that can directly transmit their locations while sampling, coordinated scanning of radars through the use of PPIs and RHIs to the exact positions of airborne radiosondes should be

Table 3.1. 0-90 hPa AGL MLCAPE, the theoretical maximum w_{MLCAPE} based on Eq. 3.4, and comparisons with the maximum radiosonde w_{air} for each radiosonde launch.

Radiosonde	MLCAPE (J kg^{-1})	w_{MLCAPE} (m s^{-1})	Maximum radiosonde w_{air} (m s^{-1})	% Difference (w_{air} from w_{MLCAPE})
2017-1	1313	51.2	46.1	-10.0
2017-2	1172	48.4	37.6	-22.3
2017-3	952	43.6	31.6	-27.6
2016-1	1510	55.6	25.2	-54.7
2016-2	2305	67.9	50.1	-26.2

considered for future field campaigns. For example, using these collocated radar and radiosonde observations, we demonstrated that most of the radiosonde measurements were likely several km away from the strongest w_{air} in these two supercell updrafts. Obtaining large samples of in situ observations in the locations of strongest w_{air} within storms continues to be challenge, but forgoing cost constraints, this sampling difficulty can be alleviated by launching a high number of GPS sensors into storms (e.g., Markowski et al. 2018) so as to increase the probability of sampling the most intense vertical motions. This would also simultaneously improve the spatial coverage of these in situ measurements.

While several of the uncertainties in the radiosonde-based w_{air} were quantified in this study, we did not quantify the uncertainty associated with hydrometeor collisions and collection on the radiosonde system. Innovative techniques and technologies to minimize or quantify these hydrometeor impacts would improve radiosonde observations within cloud systems. For example, cameras have been placed on radiosondes to assess icing impacts on in situ

observations within winter storms (Waugh and Schuur 2018), and similar strategies could potentially be used to observe the possible accumulation of hydrometeors on the radiosonde system within updrafts. Furthermore, we analyzed balloon accelerations to estimate whether and when radiosonde balloons likely burst within the supercell updrafts in order to obtain a better estimate of w_{air}, and additional sensors could be introduced to the radiosonde system to assist in assessing balloon burst events.

3.7 Conclusions

One of the goals of the C^{3}LOUD-Ex field campaign was to obtain in situ observations of the vertical velocities of supercell updrafts (w_{air}) with targeted radiosonde launches. In situ observations of supercell vertical velocities have been limited, despite their importance for understanding physical processes within supercells and for verifying simulations as well as other observational platforms with difficult-to-characterize uncertainties. In this study, we present observations of w_{air} from two isolated supercell cases observed during C^{3}LOUD-Ex, which occurred in the High Plains of Colorado, Wyoming, and Nebraska. Radiosonde w_{air} estimates were based on GPS data and were calculated with an uncertainty of $\pm$ 3.0 m s^{-1}, which considered uncertainties associated with the GPS measurements themselves, the helium balloon buoyancy, and varying drag forces. These estimates, however, did not consider hydrometeor impacts on the radiosonde systems.

In three of the five updraft radiosonde launches assessed in this study, it was likely that the radiosonde balloon burst while within the updraft, based on the extrema in the radiosonde negative accelerations. In these instances, we adjusted the w_{air} estimates to account for the loss of buoyancy associated with balloon bursting. Before these adjustments, the maximum radiosonde

w_{air} was 37.6 m s^{-1} at an altitude of 10.1 km AMSL during the 2017 case. After these adjustments, the maximum w_{air} that was observed was 50.3 m s^{-1} at an altitude of 10.3 km AMSL during the 2016 case, which occurred in the most unstable environment. At the lower and middle tropospheric levels, radiosonde 2017-3 captured the greatest w_{air} and was located within the WER, reaching a maximum value of 31.3 m s^{-1} at 7.0 km AMSL. In most of the observations presented, the radar data suggested that the radiosondes were several km away from the strongest w_{air} within the supercell updraft. This fact, along with the potential impacts of hydrometeors on the radiosonde systems, suggests that the maximum w_{air} in these two supercells could have been even larger than the values reported here.

The C^3LOUD-Ex radiosonde observations were also compared with other methods of obtaining w_{air}. One radiosonde in each of the two supercell cases sampled the updraft within the regions where dual-Doppler analyses could be performed, allowing for an independent measure of w_{air}. For the locations where the radiosondes observed the greatest w_{air}, the dual-Doppler w_{air} values were generally 15-20 m s^{-1} less than the radiosonde estimated w_{air} values. This was at least partly due to the different scales being observed by these two platforms, although it was difficult to fully quantify these differences without a detailed assessment of the dual-Doppler errors, such as may be obtained through the use of OSSEs, and which is left for future work. However, these comparisons did demonstrate that radiosondes provide complementary data to multi-Doppler analyses in terms of their ability to sample regions with low signal-to-noise ratios and to provide localized, high-resolution observations, both of which can be challenging in multi-Doppler analyses. The maximum radiosonde-based w_{air} values were also 10-55% less than the theoretical maximum w_{air} from parcel theory. The variability in these differences was

primarily due to the locations within the broad supercell updrafts that were sampled by the radiosondes, which were gleaned through utilizing collocated radar data.

Some of the challenges associated with making radiosonde observations of updrafts were highlighted here, and additional ideas on how these challenges can be surmounted were provided. There continues to be large uncertainty in the vertical velocities within deep convection, which are important for understanding many atmospheric processes and improving models. In situ observations of w_{air} can complement remotely-sensed estimates both by providing both an independent measure of w_{air} for comparison and by observing finer-scale motions that often cannot be resolved using remote sensing. As such, despite their relative scarcity, in situ observations of w_{air} can contribute to a more comprehensive understanding of storm vertical motions and hence should be considered for future field campaigns.

CHAPTER 4: THE IMPACTS OF VARYING CONCENTRATIONS OF CLOUD CONDENSATION NUCLEI ON DEEP CONVECTIVE CLOUD UPDRAFTS – A MULTIMODEL ASSESSMENT

4.1 Introduction

One of the primary and most studied pathways in which aerosol particles interact with deep convective clouds is via their ingestion into convective updrafts. Within these updrafts, supersaturated conditions develop, which can allow aerosol particles to serve as cloud condensation nuclei (CCN), becoming the seeds for cloud droplet formation (Köhler 1936). By altering the number concentrations of CCN that enter a cloud's updraft, the number concentrations and sizes of the cloud droplets within the updraft will also vary, which can have many subsequent feedbacks on a cloud's characteristics and evolution (e.g., Twomey 1977; Albrecht 1989). Typically, the majority of CCN are ingested through the bases of deep convective clouds within the atmospheric boundary layer, although several studies have shown that some fraction of CCN in the middle troposphere can also become entrained within deep convective updrafts, form cloud droplets, and subsequently impact the cloud development (Fridlind et al. 2004; Lebo 2014; Marinescu et al. 2017).

When the number concentrations of CCN that are ingested into an updraft are increased, the initial response is an increase in the cloud droplet number concentration, which results in smaller cloud droplet sizes due to increased competition for the available water vapor (e.g., Twomey and Squires 1959). While this first step in the chain of aerosol-updraft interactions is well-understood, many studies have shown that the subsequent responses in deep convective

cloud updrafts are complex and have had conflicting results (e.g., Khain et al. 2005; van den Heever et al. 2006; Tao et al. 2007; Fan et al. 2009; and as reviewed by Tao et al. 2016).

One of the most prevailing theories on these subsequent processes within deep convective updrafts is the concept of CCN-induced convective invigoration, originally reported in both observational and modelling studies (e.g., Andreae et al. 2004; Khain et al. 2005, Wang 2005; van den Heever et al. 2006). Generally, CCN-induced convective invigoration refers to the increase in the vertical velocity magnitudes within convective cloud updrafts when exposed to higher concentrations of CCN. Due to higher number concentrations of cloud droplets that form, more latent heating occurs, resulting in more buoyant (i.e., invigorated) updrafts. However, the specific process that causes the enhanced latent heating and more buoyant updrafts has been shown to vary. For example, some studies have reported that this increased latent heating within deep convective updrafts under relatively high CCN concentrations is primarily the result of increased condensation due to the higher number concentrations of cloud droplets (e.g., Wang 2005; Fan et al. 2007; Seiki and Nakajima 2014; Sheffield et al. 2015). Other studies have shown, however, that when a deep convective cloud is exposed to higher concentrations of CCN, more of the cloud's liquid water reaches the mixed-phase region and freezes, and the additional latent heating induced by enhanced freezing processes is the primary factor driving the increased latent heating and intensified updrafts (e.g., Rosenfeld et al. 2008; Li et al. 2008; van den Heever et al. 2011; Fan et al. 2012a). Furthermore, other studies have shown that when exposed to higher concentrations of CCN, some deep convective updrafts remain unchanged or weaken (e.g., Tao et al. 2007; Fan et al. 2009; Lebo and Seinfeld 2011), contradictory to the invigoration concepts described above. For example, increased condensate mass can form within updrafts that are exposed to higher concentrations of CCN and can weaken updraft vertical velocities (e.g.,

Storer and van den Heever 2013). Even for one of the most established concepts on the interactions of aerosol particles with deep convective clouds, the results appear to be muddled due to the complex kinematic and microphysics processes and feedbacks in deep convection.

These seemingly conflicting results have been attributed to the many differences between the various studies. For example, the type of deep convective cloud system under consideration can alter the effect that aerosol particles have within deep convective updrafts (e.g., Seifert and Beheng 2006b; Khain et al. 2008; van den Heever et al. 2011). Supercells that are primarily driven by dynamical forcings have been shown to have lesser impacts from varying CCN concentrations than other types of deep convection (e.g., Grant and van den Heever 2015). For the same type of convection, however, the updraft magnitude response to increased CCN concentrations have been shown to be sensitive to the environmental conditions in which the clouds form. Case study simulations of mesoscale convective systems in environments with different relative humidity (Khain et al. 2005; Fan et al. 2007; Tao et al. 2007) and shear conditions (Marinescu et al. 2017; Chen et al. 2020) have shown different responses to the updraft magnitude for similar perturbations in CCN concentrations. Idealized simulations, in which these environmental parameters can be more systematically varied and assessed, have also demonstrated that the response in deep convective updraft magnitudes to increased CCN concentrations is sensitive to boundary layer moisture (e.g., Fan et al. 2007), convective available potential energy (CAPE; Lee et al. 2008; Storer et al. 2010), and wind shear (Lee et al. 2008; Fan et al. 2009).

In addition to different deep convective cloud types and atmospheric conditions, modeling studies on the effects of CCN on deep convective clouds have also used a diverse set of models with varying physical parameterizations and dynamical cores. As compared to those

studies that have explored aerosol-cloud interactions with just one model, relatively few studies have explored the impacts of CCN in deep convective updrafts using a range of different models. These few studies have typically utilized the same dynamical model and substituted different microphysical parameterizations to assess the dependency of the CCN-induced deep convective updraft response to the microphysical parameterization. Some of these studies use the same kinematic fields for each simulation in order to better isolate the specific microphysical processes that drive different results between the parameterizations (e.g., piggybacking approach (in Grabowski 2015; Grabowski and Morrison 2017; or kinematic driver approach in Hill et al. 2015) but consequentially cannot examine CCN-induced impacts on the cloud microphysical-dynamical feedback processes. Other studies perform multiple simulations with the same numerical model, changing only the microphysical parameterization at each simulation's initialization and allowing each simulation to evolve individually (e.g., Seifert et al. 2006; Khain et al. 2009). These latter studies primarily compared aerosol effects on deep convection with bulk and bin microphysical schemes (e.g., Seifert et al. 2006; Khain et al. 2009; Khain and Lynn 2009; Lebo et al. 2012; Fan et al. 2012b), which fundamentally differ in how they represent hydrometeor size distributions. (For a comprehensive comparison of bulk and bin microphysical parameterizations, see Khain et al. 2015.) These studies found both consistencies (Seifert et al. 2006; Khain et al. 2009) and inconsistencies (Khain and Lynn 2009; Lebo et al. 2011; Lebo et al. 2012; Fan et al. 2012b) in the deep convective updraft response to increased CCN concentrations, and some of these differences were attributed to use of saturation adjustment (Khain and Lynn 2009; Lebo et al. 2012) and the representation of aerosol nucleation sinks (Fan et al. 2012b).

These complex interaction between CCN concentrations and deep convection motivates the need for systematic multi-model comparisons to provide better insights into the range of aerosol-impacted deep convective cloud responses from different models. Such an effort has been completed through multi-institutional collaborations via the coordinated efforts of the Aerosol-Cloud-Precipitation-Climate initiative (ACPC). ACPC was first developed in 2007 and is an international working group focused on aerosol-cloud interactions (Rosenfeld et al. 2014; www.acpcinitiative.org). This group is focused on reducing the uncertainties associated with aerosol-cloud interactions and has recently organized a model intercomparison project (MIP) in order to assess the robustness of deep convective cloud responses to increased CCN concentrations in a wide range of models (van den Heever et al. 2018).

The research reported here is focused on the results obtained from the ACPC MIP, whereby seven different models from different institutions simulated the same case study of scattered deep convective clouds near Houston, Texas. Simulating the same case study forces all the models to produce similar types of clouds in comparable environments, while still allowing the models to freely evolve and produce their own realizations of the event, including the critical feedbacks between cloud dynamical and microphysical processes. A recent case study MIP was completed to assess the robustness of the impacts of aerosol particles on arctic stratocumulus clouds (Stevens et al. 2018). The ACPC MIP represents the first time that a model intercomparison study has been used to study the effects of CCN on deep convective clouds. While the model responses in many cloud characteristics and processes (e.g., precipitation, anvils, cold pools) to varying CCN concentrations will be highlighted in a complementary study (van den Heever et al. 2020), the goals of the current study are 1) to quantify the range of responses in deep convective updraft velocities to increased CCN concentrations amongst a suite

of state-of-the-art models and 2) to present and physically explain the consistent and inconsistent updraft trends amongst these models.

4.2 ACPC Model Intercomparison Project (MIP)

a. Case study simulations

The ACPC MIP simulations are based on a case of scattered convective clouds that developed near Houston, Texas on 19-20 June 2013. Figure 4.1 shows several snapshots of the radar reflectivity during this event from the Houston NEXRAD radar (KHGX). In the late morning hours, there were weak, scattered, isolated convective clouds along a trailing front that extended zonally across the southeastern United States, into southern Louisiana and eastern Texas. With increased insolation in the late morning and early afternoon hours, the convection associated with this trailing front became more intense. Together with the deepening boundary

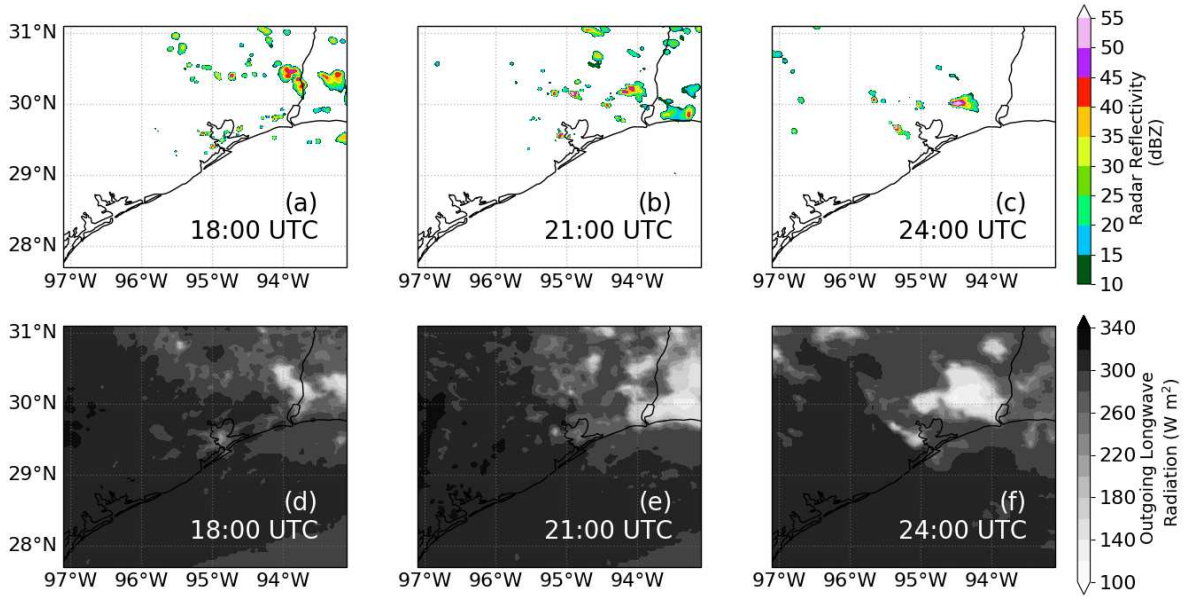

Figure 4.1. Evolution of KHGX radar reflectivity at approximately (a) 1800 UTC, (b) 2100 UTC, (c) 2400 UTC, centered around Houston, Texas. Radar reflectivity is gridded and shown at ~3.0 km AGL. Panels (d-f) show the evolution of outgoing longwave radiation from the NOAA GOES satellite at the same times as in (a-c).

layer and a sea breeze, widespread scattered convective clouds were generated throughout the region surrounding Houston. Isolated convective clouds continued to initiate, develop and dissipate for several hours, with a few cells becoming intense, reaching the tropopause and creating anvils.

To reproduce the scattered nature of convection that was associated with this event, simulations were conducted using atmospheric conditions representative of this case study. To assist in comparisons between the models, all modelling teams tried to adhere as closely as possible to a set of previously tested simulation specifications (Table 4.1; van den Heever et al. 2018). Simulations utilized three nested domains in order to capture the synoptic-scale influences (e.g., trailing front), while still resolving the deep convective clouds that formed. The focus of all of the analyses was on the innermost grid (Figure 4.2a), which had 500 m horizontal grid spacing and covered an area of approximately 62,500 km2. The simulations were conducted for 27 hours

Table 4.1. ACPC MIP simulation specifications, as defined in the ACPC Deep Convective Cloud Roadmap (van den Heever et al. 2018).

Model configuration	**Description**
Simulation period	1200 UTC 19 June 2013 to 1500 UTC 20 June 2013
Total simulation hours	27
Initialization and boundary data	NCEP Global Data Assimilation System (GDAS)/FNL
Number of model domains	3, one-way nesting only (no interactive nests)
Horizontal grid spacing of each domain	4.5km, 1.5km, 500m
Number of horizontal grid points in each nest (Approximate size in km of each domain)	4.5 km domain: 400 x 400 grid points (~1800 x 1800 km), 1.5 km domain: 547 x 547 grid points (~820 x 820 km), 500 m domain: 500 x 500 grid points (~250 x 250 km)
Vertical levels	95, stretched from approximately 50 m near the surface to 300 m around 4 km AGL
Model top	Approx. 22km / 50hPa
Center latitude / longitude	29.4719 N / 95.0792 W (same for all domains)
Model time steps	4.5 km domain: 6 s 1.5 km domain: 3 s 500 m domain: 3 s
Convection parameterization	No convection or cumulus scheme in any of the 3 domains

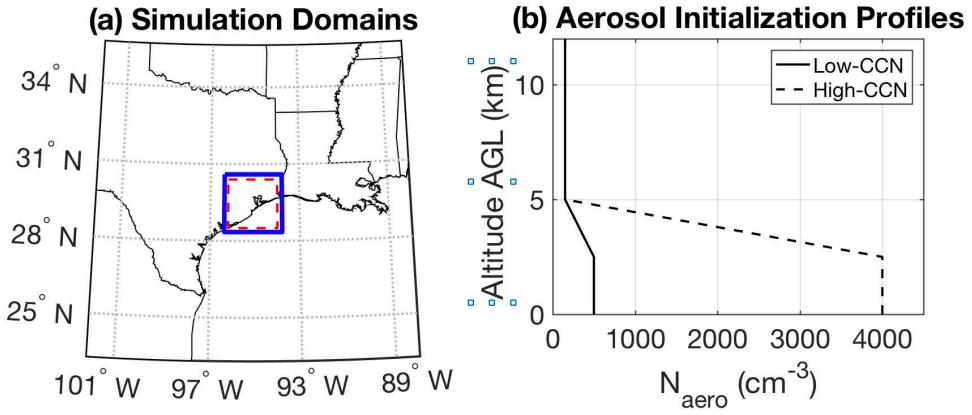

Figure 4.2. (a) ACPC Simulation Grid 2, with nested domain, Grid 3, shown in blue. All analysis computed within a subset of Grid 3, (red dashed line) in order to avoid boundary impacted model grid cells. (b) Horizontally homogeneous aerosol initialization profiles for the Low-CCN and High-CCN simulations.

to capture the impacts of the CCN concentrations on the entire diurnal cycle. The model output was saved at a high frequency (every 5 minutes) during the 12-hour period (1600 UTC – 0400 UTC) when deep convective clouds were present in the observations and simulations. This 12-hour period will also be the focus of the analyses presented here. While all the participants in the ACPC MIP attempted to follow the specifications in Table 1, some models were not equipped to adhere with all the specifications. These details of each model and the major discrepancies between them are discussed in the next sections and are displayed in Appendix 3.

b. Aerosol initialization

For each participating model, two simulations were conducted with relatively high and low initial CCN concentrations (Figure 4.2b). These vertical profiles were based on both satellite-based CCN estimates near Houston on 19 June 2013 via the methodology described in Rosenfeld et al. (2012), as well as aerosol observations in the boundary layer and free troposphere from aircraft during the Deriving Information on Surface conditions from Column and Vertically Resolved Observations Relevant to Air Quality (DISCOVER-AQ) field

campaign, which had operations near Houston, Texas in September 2013 (DISCOVER-AQ Science Team). In addition to the aerosol number concentration profiles, uniform aerosol number size distributions were also specified using a log-normal distribution with a geometric mean diameter of 100 nm, a geometric standard deviation of 1.8, and a uniform hygroscopicity parameter of 0.2. These additional aerosol distribution characteristics were also based on data from DISCOVER-AQ. While aerosol number concentrations were initialized in a horizontally homogenous manner across all the model domains at the beginning of each simulation, the aerosol field was allowed to evolve in each model through processes such as advection, diffusion, activation and wet deposition, if the model had that capability (e.g., Figure 4.3). Furthermore, aerosol particles were restricted from interacting with radiation in order to isolate the microphysical effects of increased aerosol concentrations on convective clouds. The manner in which each model parameterized ice nucleation was also kept constant from the low to high CCN simulations, and these parameterization details are provided in Appendix 3.

c. Models

Seven models participated in the ACPC MIP (Table 4.2). Several important differences between these models are highlighted here, with additional details provided in Appendix 3. Firstly, six of the models utilized two-moment (2M) bulk microphysical parameterizations, except for WRF-SBM which used a spectral bin microphysics scheme (SBM; Khain et al. 2004; Shpund et al. 2019). While the other six models utilized 2M bulk schemes, these schemes have varying levels of sophistication in their representations of microphysics processes. For example, three models either prognose or diagnose supersaturation (RAMS, NU-WRF, WRF-SBM), while the other models all utilize saturation adjustment, whereby any supersaturation that develops is

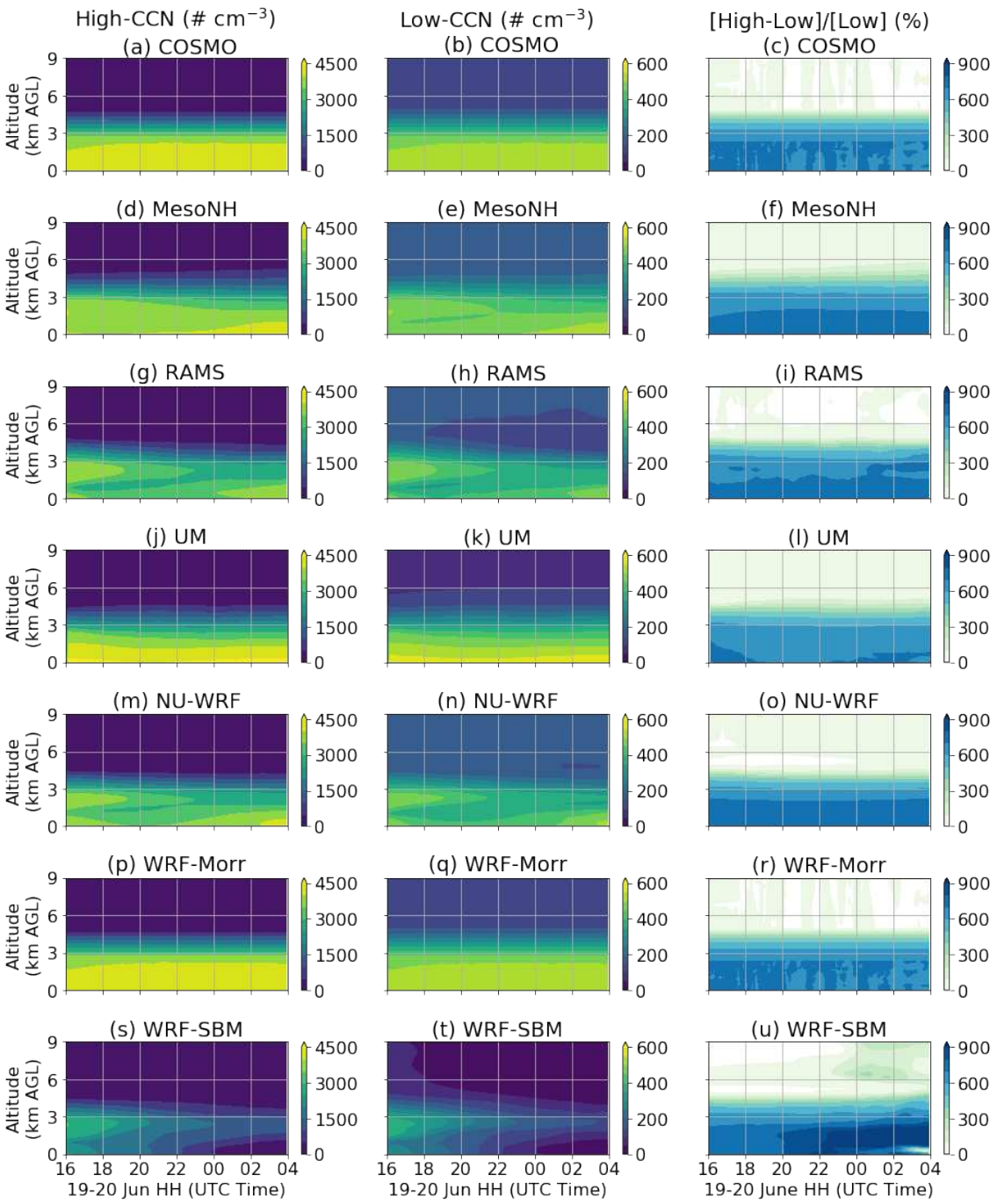

Figure 4.3. Evolution of domain-mean aerosol concentrations in the High-CCN simulation (left column), Low-CCN (center column), and the percent difference of High-CCN from Low-CCN (right column) for all the models. Note the difference in scales between the High-CCN and Low-CCN columns.

eliminated at each time step via condensation onto already formed hydrometeors. The use of saturation adjustment in microphysical schemes has been shown to weaken the response of deep

convective updrafts to varying CCN concentrations (e.g., Khain and Lynn 2009; Lebo et al. 2012).

Table 4.2. Participating models in the ACPC MIP.

Model	Abbreviation	Primary Reference(s)	Institution
Consortium for Small-scale Modeling v5.1	COSMO	Schattler et al., 2016	Karlsruhe Institute of Technology
MesoNH Model v5.4.1	MesoNH	Lac et al., 2018	Meteo-France
Regional Atmospheric Modeling System v6.2.09	RAMS	Cotton et al., 2003; Saleeby and van den Heever, 2013	Colorado State University
Unified Model v.10.8	UM	Walters et al., 2017	University of Leeds
NASA Unified Weather Research and Forecasting (WRF) Model, v3.9.1	NU-WRF	Skamarock et al., 2008;	NASA Goddard Institute of Space Studies
WRF, v3.7.1, with Morrison Microphysics	WRF-Morr	Skamarock et al., 2008	University of Oxford
WRF, v4.0.3, with Hebrew University Cloud Model Bin Microphysics	WRF-SBM	Skamarock et al., 2008	Pacific Northwest National Laboratory

All of the models represent aerosol activation, although via different formulations (see Appendix 3 for the details). Two models (COSMO and WRF-Morr) have fixed aerosol profiles, while the other five models allow aerosol particles to be tracked and advected by the wind. The latter five models, however, have differences in terms of their aerosol sources and sinks (e.g., aerosol regeneration via evaporation and sublimation, activation sinks, wet and dry deposition). These aerosol sinks and sources can have impacts on interpreting aerosol effects in deep convective clouds (e.g., Siefert et al. 2006; Fan et al. 2012b). Because of the differences in aerosol processes, each model's ACPC MIP simulations have aerosol concentrations that evolve differently (Figure 3, left and middle columns). However, the relative differences between the High-CCN and Low-CCN simulations amongst the models are generally quite similar (Figure 4.3, right column). Six of the seven models' high-CCN simulations have, on average, between

7.0-7.5 times more particles than the low-CCN simulations in the boundary layer (0-1km AGL). The WRF-SBM simulations (Fig 4.3s-u) had more significant sinks of aerosol concentrations than the other models, which resulted in larger differences in aerosol concentrations between the High-CCN and Low-CCN simulations, as compared to the other models.

Two of the ACPC MIP participants (UM and MesoNH) were unable to ingest the GDAS-FNL data, and therefore, simulated the event with the ERA-Interim reanalysis and ECMWF real-time forecasting system data, respectively. Despite the different initialization data, the MesoNH model produced very similar environmental conditions to the other models that initialized with the GDAS-FNL data, while the UM simulations had slightly warmer and drier boundary layers but similar wind shear conditions (Figure 4.4a-c). While the COSMO model was initialized with the GDAS-FNL data, this initialization resulted in significantly warmer and moister boundary layers compared to the other models. Despite these differences between the models, differences in the environmental conditions between the High-CCN and Low-CCN simulations were generally small and had consistent trends amongst the models (Figure 4.4d-f). For example,

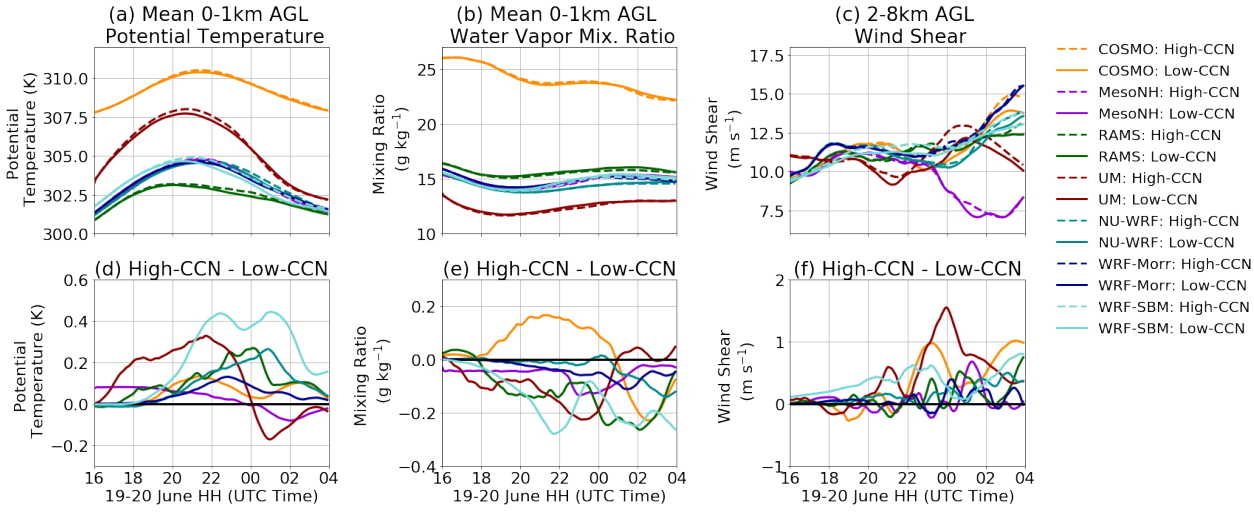

Figure 4.4. Evolution of (a) boundary layer, below cloud base (0-1 km AGL) potential temperature, (b) boundary layer, below cloud base water vapor mixing ratio, and (c) 2-8 km layer wind shear. (d-f) depict the differences between the High-CCN and Low-CCN simulations for the variables in (a-c), respectively.

generally, the High-CCN simulations were marginally warmer and drier, and resulted in slightly stronger wind shear than the Low-CCN simulations, with the warmer and drier boundary layer conditions in the High-CCN simulations being likely due to less widespread precipitation, a consistent signal in all the models. These differences in the environmental conditions between the models were typically less than 0.3 K, 0.2 g kg-1 and 1 m s-1 for the average boundary layer potential temperature, boundary layer water vapor mixing ratios, and 2-8 km wind shear, respectively.

While the preceding paragraphs have focused on comparisons of the model and simulation characteristics that have been shown to modulate the impacts of aerosol particles on deep convective cloud updrafts in previous research, it is important to note that each model is also integrated with various other physical parameterizations (e.g., surface, radiation and turbulence) that might impact the model solution. These additional model details are provided in Appendix 3. Due to the many differences in the models, it is difficult to attribute the variability in the CCN effects to specific microphysical and/or aerosol parameterizations and processes; rather, the goal of this study is to quantify the spread in the CCN effects on convective updrafts in the standard model configurations of the ACPC MIP models and to present the consistent and inconsistent trends.

Despite these model differences, all the models produce scattered deep convective clouds near Houston, Texas in both the High-CCN and Low-CCN simulations during the 12-hour period (Figure 4.5). In this study, deep convective updrafts are determined as follows. All simulation data are screened to only include columns where 75% of the grid points between 3 and 10 km AGL have total condensate mixing ratios greater than 0.1 g kg-1 and vertical velocities greater than 3 m s-1. Any other grid points within these columns that have total condensate mixing ratios

greater than 0.1 g kg-1 are also included in the analysis in order to include the updraft boundaries that may not meet the vertical velocity threshold but are still part of the updraft. Several additional thresholds were also considered, tested and found to produce qualitatively similar results. While there are differences in the timing and longevity of the periods when deep

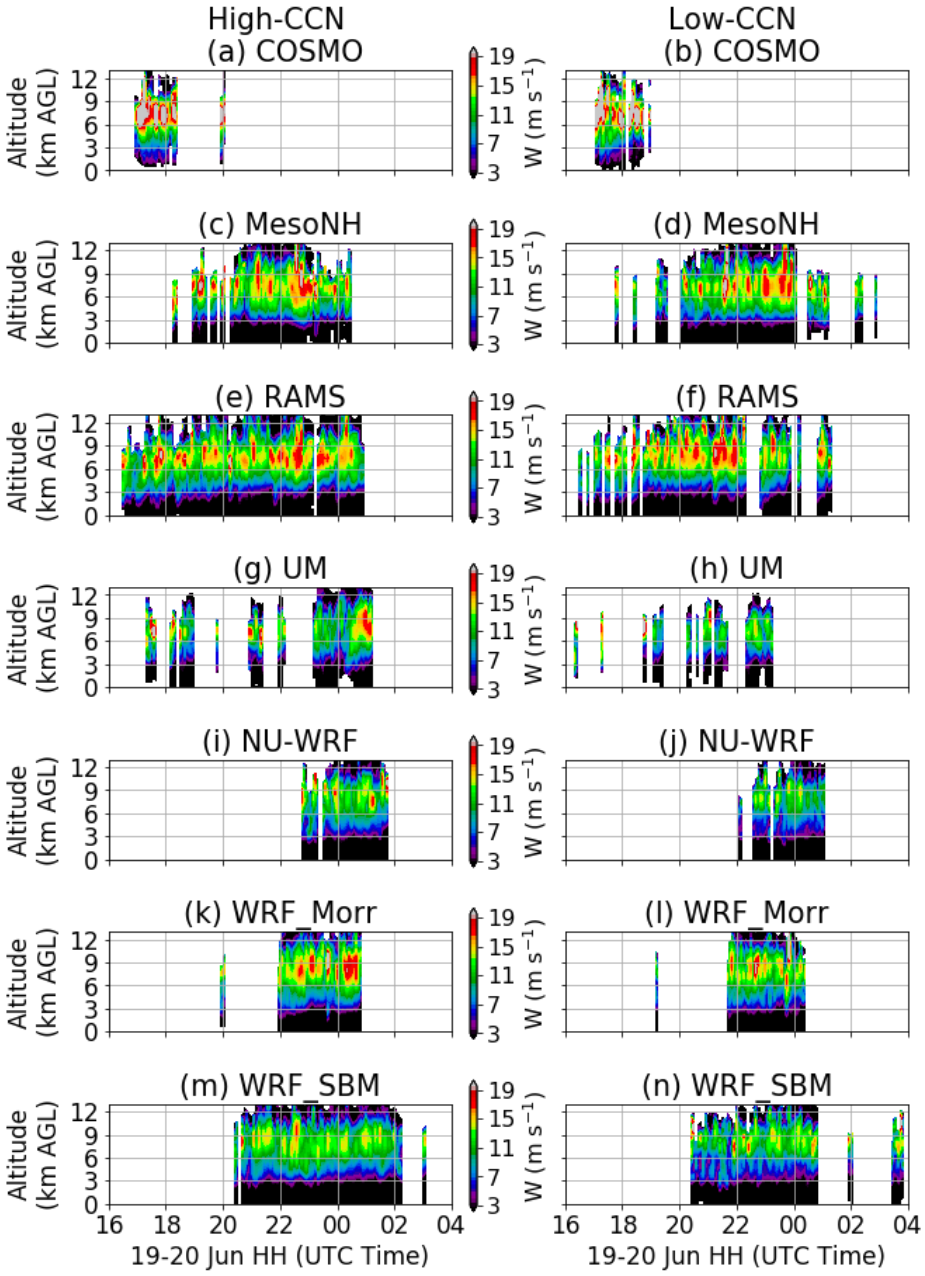

Figure 4.5. Temporal evolution of mean updraft velocities for deep convective columns, as defined in the text. The left column represents the High-CCN simulations, while the right column represents the Low-CCN simulations.

convective clouds are present amongst the models, the convective cloud periods are similar in the High-CCN and Low-CCN simulations for each individual model, meaning that varying CCN concentrations in each model does not affect the initiation and lifecycle of deep convection as much as the differences in the model parameterizations and initialization datasets. Of note, the COSMO model produces much less convection than the other models, which is likely due to its different environmental conditions. As such, due to the lower sample size of deep convective updrafts in COSMO, the analyses between its High-CCN and Low-CCN simulations may be less statistically robust. Using these identified deep convective cloud updrafts, their differences under the High-CCN and Low-CCN conditions will now be assessed.

4.3 CCN effects on the deep convective updrafts

a. Frequency

In order to assess the variations in the amount and vertical distribution of the deep convective updrafts in the High-CCN and Low-CCN simulations, contour frequency by altitude diagrams (CFADs) are used (Figure 4.6). All of the High-CCN simulations have a higher frequency of the most extreme updraft vertical velocities, particularly from ~2-7 km AGL, than the Low-CCN simulations. Also, six of the seven models simulate more frequent deep convective updrafts for most of the updraft magnitudes in the High-CCN simulations compared to the Low-CCN simulations (Figure 4.6o-u), although the magnitude of this response was variable amongst the models. For example, the WRF-SBM and UM models have a total of 3-3.5 times more convective updrafts (of the same magnitudes) in their High-CCN simulations, while the other models show more moderate responses of 1.1-1.5 times. These CCN-induced changes in deep convective updraft amounts are likely due to the reduced cloud droplet collision-

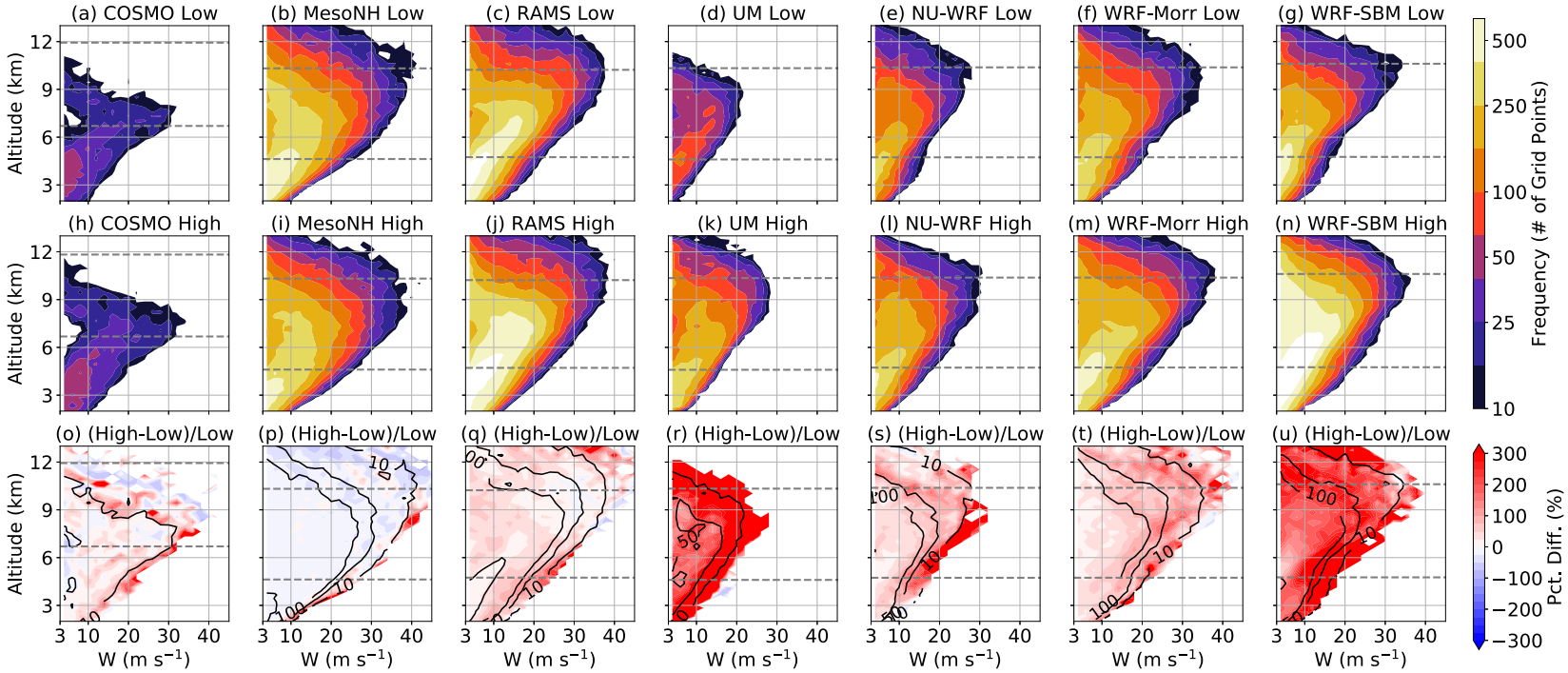

Figure 4.6. Counter frequency by altitude diagrams (CFADs) of vertical velocities within the deep convective updrafts, as defined in the text. Panels (a-g) represent the Low-CCN simulations, panels (h-n) represent the High-CCN simulations, and panels (o-u) represent the percentage difference of the High-CCN from the Low-CCN simulations. The black contours in (o-u) are the frequency counts from the Low-CCN simulations for each model, respectively and are plotted for reference. CFADs are binned at 2 m s^{-1} intervals, starting at 3 m s^{-1}. The gray dashed lines represent the altitudes where the base state temperatures are 0°C and the -38°C , respectively.

coalescence and warm-rain precipitation in the High-CCN simulations, which allows more clouds to become deeper (e.g., Sheffield et al. 2015) and meet the deep convective updraft criteria.

b. Intensity

The mean vertical velocity profile within the deep convective updrafts, as well as the percentage difference between the High-CCN and Low-CCN profiles, are shown in Figure 4.7. Firstly, the mean profiles for all the model simulations have similar shapes, peaking between 7 and 9 km AGL, suggesting that comparable updrafts magnitudes and structures are being assessed, both between the models and between the High-CCN and Low-CCN simulations (Figure 4.7a). All the models produce stronger updrafts (5-15% in 5 of the 7 models) between 3

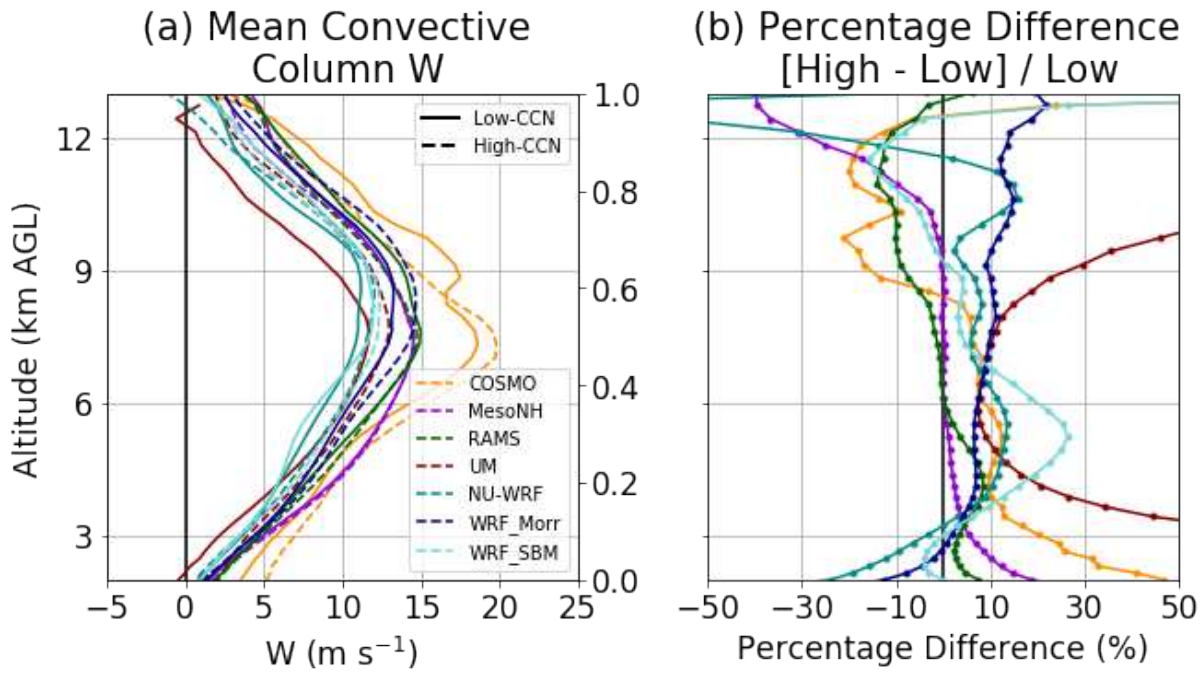

Figure 4.7. (a) Profiles of mean vertical velocities over deep convective updrafts in all the simulations. The solid lines represent the Low-CCN simulations, and the dashed lines represent the High-CCN simulations. (b) Vertical profiles of the percent difference in the High-CCN simulations' mean vertical velocities from the Low-CCN simulations' mean vertical velocities, as show in (a).

and 5 km AGL in the High-CCN simulations compared with their Low-CCN counterparts (Figure 4.7b). The WRF-SBM has the most extreme response (up to 28% stronger updrafts at 5 km AGL), which may be related to the larger differences in the WRF-SBM aerosol concentrations between the High-CCN and Low-CCN simulations (Figure 4.3). The signal of more intense updrafts in the High-CCN simulations wanes in the majority of the models above 4-5 km AGL, but still remains neutral to weakly positive (0-10% stronger) in all the models through ~8 km AGL, near where the peak vertical velocities are achieved. Above 8-9 km AGL, the models' results diverge, with 4 models showing weaker updrafts and 3 models having stronger updrafts in the High-CCN simulations.

To better understand the trends in the mean deep convective updraft magnitudes, normalized CFADs are also calculated (Figure 4.8), which eliminate the CFADs' dependence on absolute number and thus can be used to more easily compare the shapes of the vertical velocity distributions at each altitude. The shift to more frequent occurrences of the most intense updrafts and less frequent occurrences of the weaker updrafts in the High-CCN simulations from ~2-7 km AGL, as was noted in Figure 4.6, becomes even more evident in Figure 4.8o-u. The three models (UM, NU-WRF, WRF-Morr; Figure 4.8r-t) that demonstrate this shift throughout the depth of the convective updrafts also have stronger mean updrafts above 8 km AGL in the High-CCN simulations (Figure 4.7b). The other four models (COSMO, MesoNH, RAMS, WRF-SBM), which have weaker mean updrafts above 8 km AGL in the High-CCN simulations (Figure 4.7b), depict a more irregular signal in the normalized CFAD differences in the upper tropospheric levels (Figure 4.8o-q,u). To better understand the physical processes that are associated with these updraft responses to the varying CCN concentrations, the terms of the vertical velocity tendency equation are assessed.

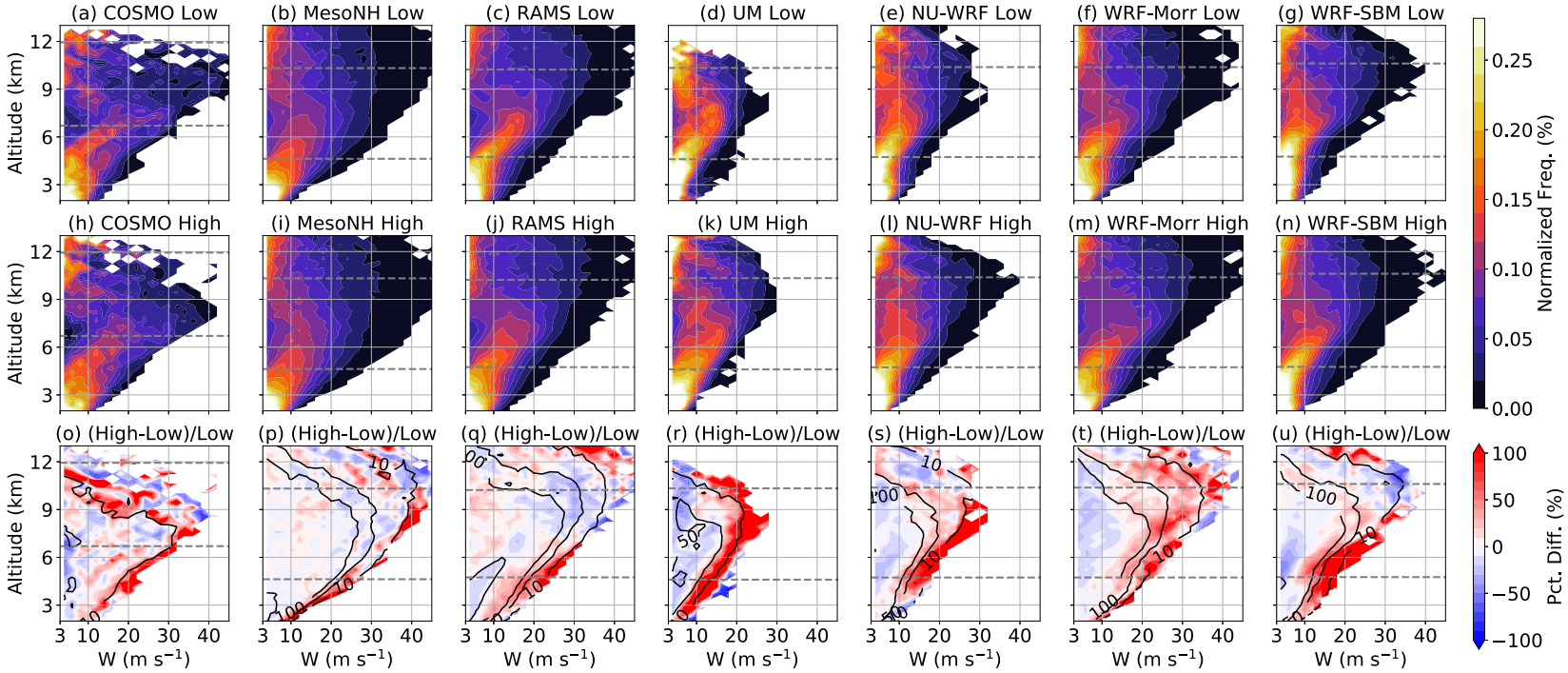

Figure 4.8. Normalized CFADs. Same as Figure 6, except that the CFAD value at each altitude are normalized for the total number of grid points at that altitude.

4.4 Vertical velocity tendency equation and terms

Each model utilizes different prognostic variables and approximations to predict how the vertical velocity (*w*) changes with time during the model integration. Because each model's representation and calculation of the vertical momentum equation are different, we use a basic form of the vertical momentum equation (Eq. 4.1) and approximate the various terms for each model's native grid and standard variable outputs.

$$\frac{\partial w}{\partial t} = \underbrace{\underbrace{\underbrace{g\frac{\theta'}{\theta_0}}_{B_{TH}} + \underbrace{g r_v' \frac{(1-\varepsilon)}{\varepsilon}}_{B_{WV}} + \underbrace{-g r_c}_{B_{CL}}}_{B_{net}} + \underbrace{-\frac{1}{\rho}\frac{\partial p'}{\partial z}}_{VPPG} + \underbrace{-w\frac{\partial w}{\partial z}}_{VADV} + \underbrace{-u\frac{\partial w}{\partial x} - v\frac{\partial w}{\partial y}}_{HADV}} \qquad (4.1)$$

In Eq. 4.1, the term on the left-hand side is the local time derivate of *w*, which represents how *w* changes with each model time step at each grid point. On the right-hand side (RHS), the first three terms represent the buoyancy (B) acceleration terms. The first RHS term is the buoyancy acceleration associated with changes in temperature, where θ' is the perturbation potential temperature, θ_0 is the base state potential temperature, and g is the gravitational acceleration of 9.8065 m s^{-1}. The second RHS term is the buoyancy acceleration associated with changes in the amounts of water vapor in the air, where r_v' is the perturbation water vapor mixing ratio, and ε is the ratio of dry air to water vapor gas constants (~0.622). The third RHS term is the buoyancy acceleration associated with the amount of water condensate mass, where r_c is the total condensate mixing ratio. These three terms, when summed, represent the net buoyancy acceleration (B_{net}) and have been the primary focus of most assessments of aerosol effects on deep convective updrafts (e.g., Khain et al. 2005; Rosenfeld et al. 2008; Lebo and Seinfeld 2011; Storer and van den Heever 2012).

The fourth RHS term is the vertical perturbation pressure gradient (VPPG) acceleration, where ρ is the air density, and $\frac{\partial p'}{\partial z}$ is the vertical gradient in the perturbation pressure. The fifth

RHS term is the acceleration due to vertical advection (VADV), where $\frac{\partial w}{\partial z}$ is the vertical gradient in *w*. Finally, the last two terms on the RHS of Eq. 4.1 represent the acceleration due to horizontal advection (HADV), where u and v are the zonal and meridional wind components, and $\frac{\partial w}{\partial x}$ and $\frac{\partial w}{\partial y}$ are the horizontal gradients in *w*. Typically, Eq. 4.1 would also include a diffusion term, but because of the larger discrepancies on how diffusion is represented in these models, the diffusion term is not considered in this study.

Some of the terms in Eq. 4.1 require a perturbation and/or base state variable. This perturbation value is calculated by subtracting a time-varying, altitude-dependent base state value from the full variable value. A base state profile was calculated for each simulation as an average value based on the non-cloudy grid points (total condensate < 0.1 g kg^{-1}) at the varying model altitudes. Additional details on the calculation of these terms and the base state profiles are provided in Appendix 4.

To test these approximations for the various terms, a brief closure assessment was conducted. For one of the models (RAMS), the model data were outputted for three consecutive model times (the time step is 3 s), such that an accurate approximation of $\frac{\partial w}{\partial t}$ could be made using a centered-in-time difference. Each of the terms from Eq. 4.1 was calculated for the middle of the three times, based on the approach described in the preceding paragraph. Figure 4.9a-g shows these various term calculations for a horizontal slice through a deep convective updraft at 7.6 km AGL. The terms have varying signs and distributions within the updraft. The sum of the terms (RHS of Eq 4.1; Figure 4.9h) is compared to the $\frac{\partial w}{\partial t}$, which is calculated from the *w* field in the model (Figure 4.9i). The residual from this comparison (Figure 4.9j) is much smaller than the sum of the terms (Figure 4.9h) and most of the individual terms (Figure 4.9a-g). The largest

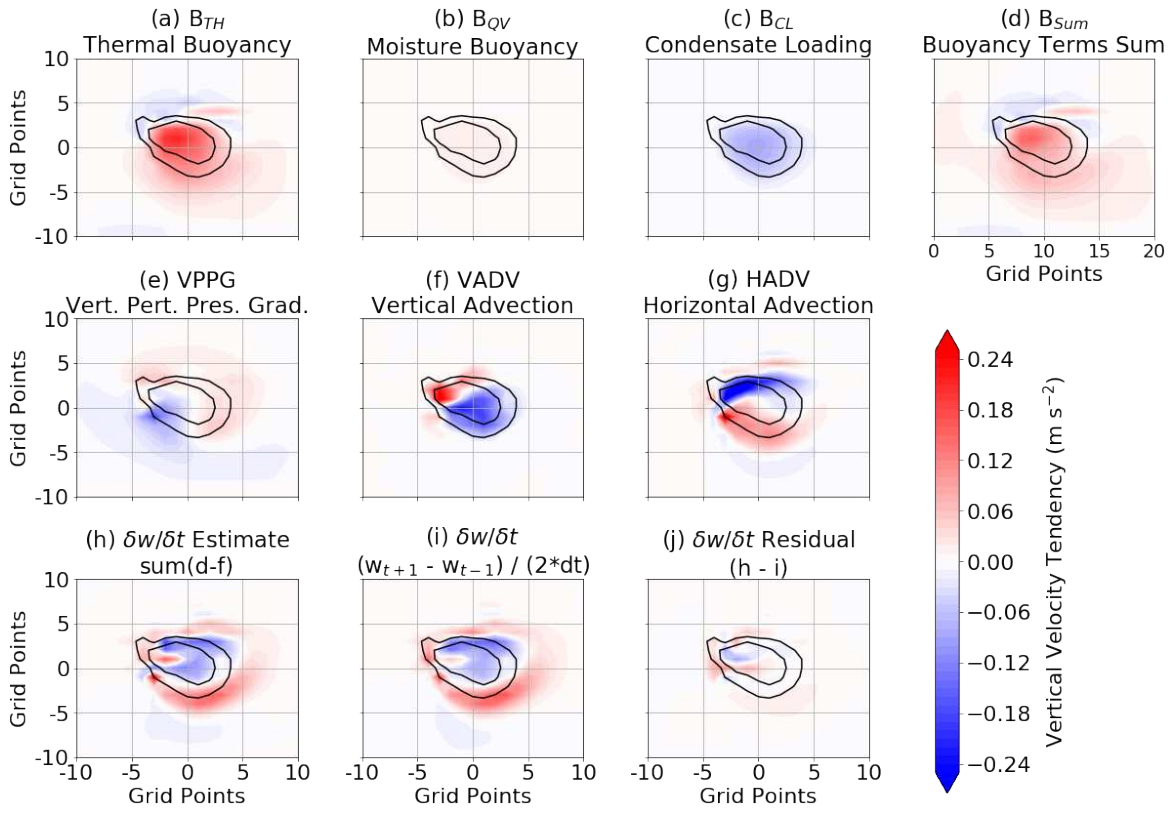

Figure 4.9. Horizontal slice at 7.6 km AGL through a deep convective cloud from the RAMS Low-CCN simulation at 21:00:03 UTC. Panels (a-g) represent the vertical velocity tendency terms in Eq. 1., using the approach defined in the text. Panel (h) is the sum of these terms, which represents an estimate of $\frac{\partial w}{\partial t}$. Panel (i) is the $\frac{\partial w}{\partial t}$, estimated using centered-in-time differencing from the model *w* from the timesteps directly before and after 21:00:03 UTC. (j) is the residual in $\frac{\partial w}{\partial t}$ (h minus i). The black contours represent vertical velocities of 5 and 15 m s^{-1}.

residual values are present along the strongest horizontal gradients in *w* (Figure 4.9j), which was likely related to the exclusion of the diffusion term which would have the strongest impacts in these high-gradient regions. Although Figure 4.9 only depicts one horizontal slice through one convective updraft in one of the models, this closure was calculated for all the cloudy updrafts at this time with the RAMS model output and produced similar results. This closure exercise therefore demonstrates that the terms of the vertical velocity tendency equation (Eq. 4.1) can be accurately calculated in this manner using these simulation data. In the following sections, we

compare these terms in the High-CCN and Low-CCN simulations for all the models in order to explain the trends in the mean updrafts.

a. Thermal buoyancy (B_{TH})

Figure 4.10 depicts the mean thermal buoyancy term for the deep convective updrafts averaged for each model vertical level and for 2 m s^{-1} intervals of *w* (the same bins as the CFADs in Figures 4.6 and 4.8). Since all of the terms in Eq. 4.1 are either directly or indirectly dependent on the magnitude of *w*, this analysis allows for the comparison of the High-CCN and Low-CCN simulations at the same values of *w.*

The thermal buoyancy term (B_{TH}) is positive for almost all convective updraft regions (Figure 4.10a-n), except for the convective updraft tops (above ~10 km AGL) where evaporation and / or sublimation may be resulting in cooler temperatures with respect to the environmental base state. The most intense accelerations due to thermal buoyancy are generally found between 6 and 11 km AGL, in the mixed-phase regions of the clouds. When comparing the High-CCN and Low-CCN simulation updrafts (Figure 4.10o-u), several patterns emerge. First, between ~2 and 3 km AGL, three models (COSMO, RAMS, WRF-SBM) depict weaker B_{TH} in the High-CCN simulations, two of which (RAMS, WRF-SBM) do not use saturation adjustment schemes. However from ~3-5 km AGL, most models show larger, positive B_{TH} in the High-CCN simulation, which is associated with more condensation and latent heat release onto the greater number concentrations of cloud droplets. This signal is most likely associated with stronger mean updrafts in the High-CCN simulations amongst all the models at these altitudes (Figure 4.7b). Directly above this region of stronger $B_{TH,}$ there is a deep layer (2-5 km) of weaker B_{TH} near and above the 0°C level in the High-CCN simulations, consistent with weaker condensation

rates and latent heat release. In other words, the convective updrafts in the High-CCN simulations are colder than those in the Low-CCN simulations with respect to their respective environments near and above the freezing level, a trend that is evident in all models. The altitude and magnitude of this signal reversal also corresponds to the waning of the differences in the mean updrafts between the High-CCN and Low-CCN simulations (Figure 4.7). At higher altitudes (8-12 km AGL), this signal is generally reversed again in most of the models, with the High-CCN simulations having larger, positive thermal buoyancy accelerations.

b. Water vapor buoyancy (B_{WV})

Because water vapor is lighter than dry air, regions of air with greater amounts of water vapor compared to the base state are more buoyant and lead to positive accelerations. The B_{WV} term is positive throughout the updrafts, meaning that these deep convective updrafts have greater water vapor amounts as compared to the base state, with the most intense values in the lower troposphere (Figure 4.11a-n). The magnitude of this term and its difference between the High-CCN and Low-CCN simulations is significantly lower than the thermal buoyancy term, and thus the B_{WV} term plays a lesser role in explaining the trends in updrafts magnitudes. The B_{WV} term does, however, assist in explaining the physical processes associated with the thermal buoyancy term. In Figure 4.11o-u, there is a several-km deep layer of weaker B_{WV} (e.g., drier updrafts) in the High-CCN simulations, which begins anywhere between 2 and 5 km AGL, depending on the model. These regions of weaker B_{WV} in the High-CCN simulations generally overlap and are slightly offset to lower altitudes when compared to the regions of weaker thermal buoyancy (Figure 4.10o-u). Because this analysis is focused on deep convective updrafts, these processes at lower altitudes are precursors to processes at their adjacent higher altitudes. In the

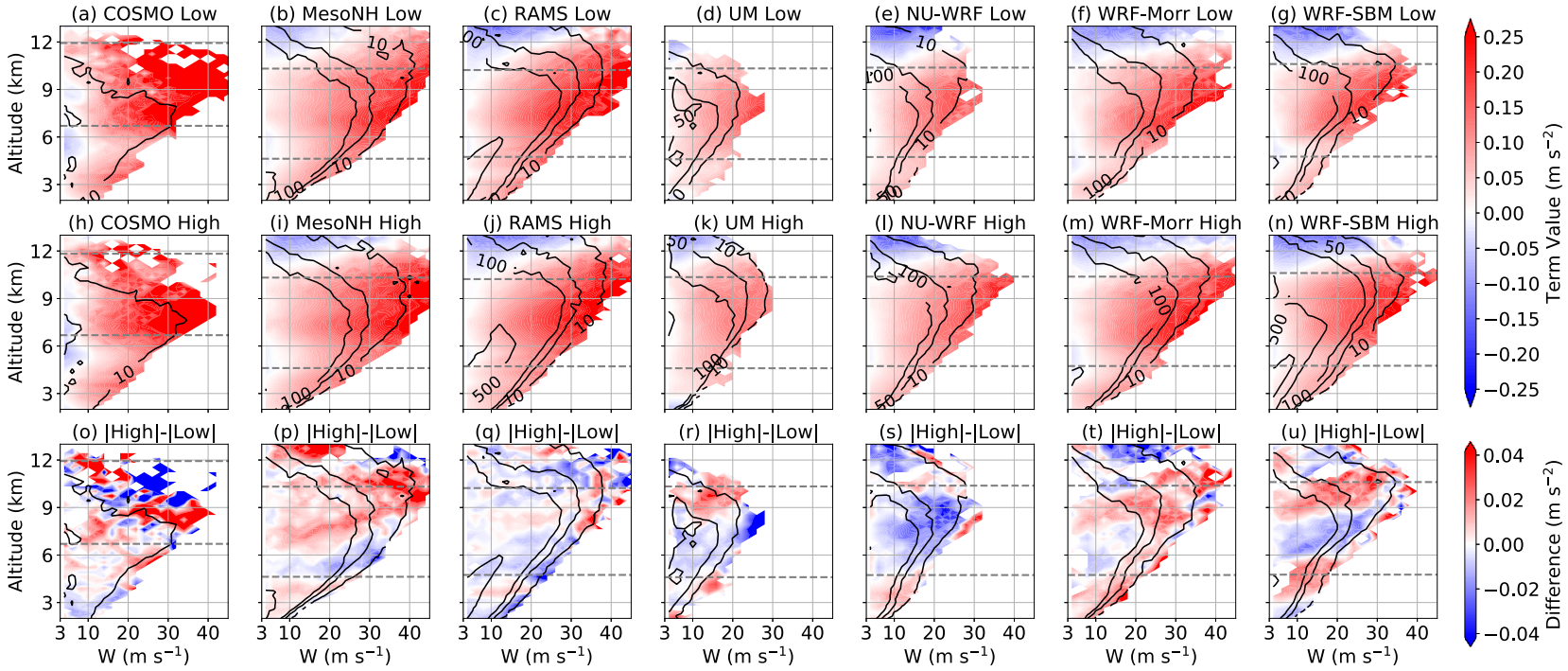

Figure 4.10. Average thermal buoyancy (B_{TH}) term for the Low-CCN simulations (top row) and for the High-CCN simulations (middle row). Values averaged over deep convective updrafts, as defined in the text, and subset by altitude and *w* using 2 m s^{-1} increments. Black contours represent the number of grid points used for the Low-CCN and High-CCN simulations respectively. The bottom row shows the difference in the absolute values between the High-CCN and Low-CCN results. The black contours in the bottom row represent the values from the Low-CCN simulations. The dashed, gray lines represent the altitudes where the mean temperatures are 0ºC and -38ºC. Note that in the bottom row, data are only shown for regions where data were present and had the same sign in both the Low-CCN and High-CCN simulations, where such comparisons are sensible.

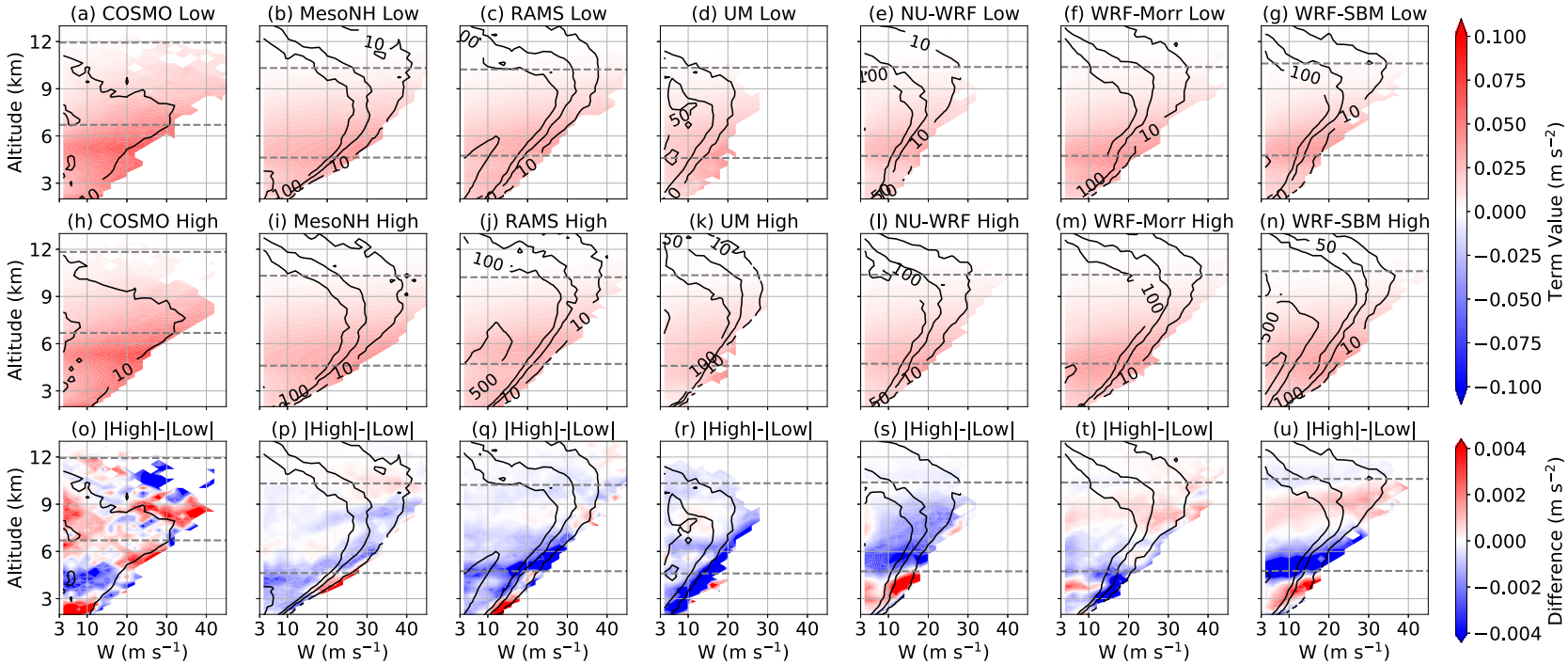

Figure 4.11. Same as Figure 4.10, but for moisture buoyancy (B_{WV}). Note the change in colorbar scale from Figure 4.10.

High-CCN simulations, enhanced condensation that drives the larger positive thermal buoyancy in first few kilometers above cloud based (~2-5 km AGL, Figure 4.10o-u) robs the updraft of its water vapor and results in drier updrafts in the altitudes above this level (Figure 4.11o-u). Therefore, near and above the 0°C level (~4-8 km AGL), the High-CCN simulations have lower water vapor amounts, and thus weaker condensation rates and weaker thermal buoyancy than the Low-CCN simulations at these altitudes. This mechanism seems to have an oscillatory nature, with higher water vapor amounts and more positive thermal buoyancy in the High-CCN simulations above 8 km AGL being evident in some of the models (particularly WRF-Morr and WRF-SBM). This reversal may also be related to the freezing processes. While this relationship between water vapor and thermal buoyancy is likely the dominant process at play in describing the trends in thermal buoyancy accelerations and the associated mean updraft trends below ~8 km AGL, we cannot rule out the impacts of entrainment on altering the water vapor and thermal buoyancy in these simulations.

c. Condensate loading buoyancy (B_{CL})

Opposing the positive thermal and moisture buoyancy terms within the updraft, the condensate loading buoyancy term (B_{CL}) is negative throughout the updraft and increases in magnitude with height (Figure 4.12a-n). Below the 0°C level, most of the models depict weaker condensate loading in the High-CCN simulation, meaning that there is less condensate in the High-CCN updrafts at these levels. This is a result of reduced amounts of liquid water mass (primarily rain) in these lower updraft levels. Above the 0°C level (~5 km AGL), five of the 5 models show a clear increase in condensate loading in the High-CCN simulations, as the lofted amounts of liquid water mass increase.

Despite these relatively consistent signals in condensate loading amongst the models, the condensate loading appears to play a lesser role than the thermal buoyancy in these simulations in terms of the differences between the High-CCN and Low-CCN simulations. Figure 4.13 shows the sum of the all three buoyancy terms (B_{net}), and it is clear that the primary differences between the High-CCN and Low-CCN simulations (Figure 4.13o-u) resemble the thermal buoyancy term responses (Figure 4.10o-u) better than the condensate loading term responses (Figure 4.12o-u). Therefore, in these simulations, updraft thermal buoyancy is more important than the updraft condensate loading in terms of explaining changes in *w* between the High-CCN and Low-CCN simulations. We compared this result to several recent studies that have also explicitly assessed the different terms of the vertical velocity tendency equation. The ACPC MIP results are similar to those of a midlatitude squall line case study (Tao and Li 2016) but differ from idealized, tropical, oceanic deep convective clouds (Storer and van den Heever 2012), which typically have weaker updrafts than those in midlatitude convection. This comparison between these studies provides further evidence that aerosol effects on updrafts are dependent on environmental conditions and type of convective cloud system.

While the buoyancy terms can be used to explain the majority of the mean updraft trends below 8 km AGL, they do not explain the diverging trends above 8 km AGL. As such, the next three sections focus on the VPPG, VADV and HADV terms in Eq. 4.1, which do assist in explaining these trends and have all received much less focus in prior research conducted on the CCN impacts on deep convective clouds.

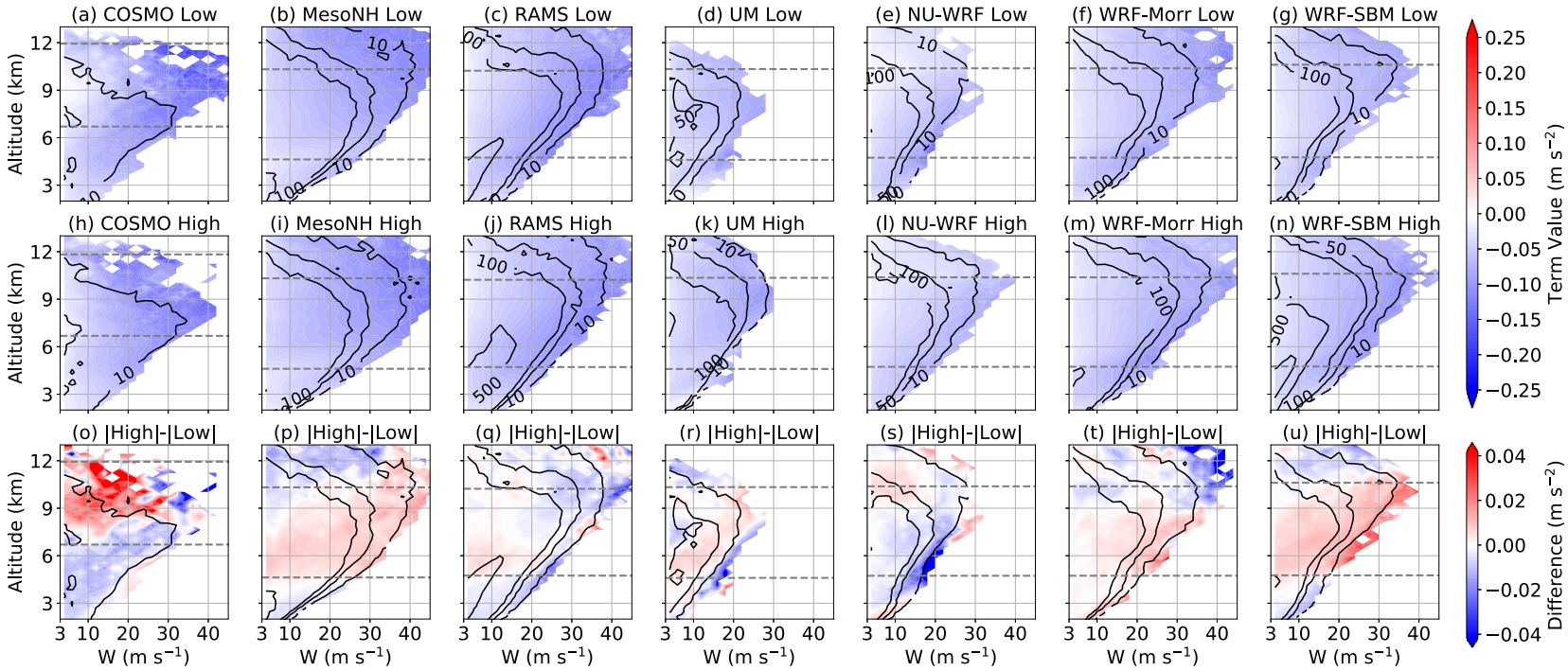

Figure 4.12. Same as Figure 4.10, but for condensate loading (B_{CL}).

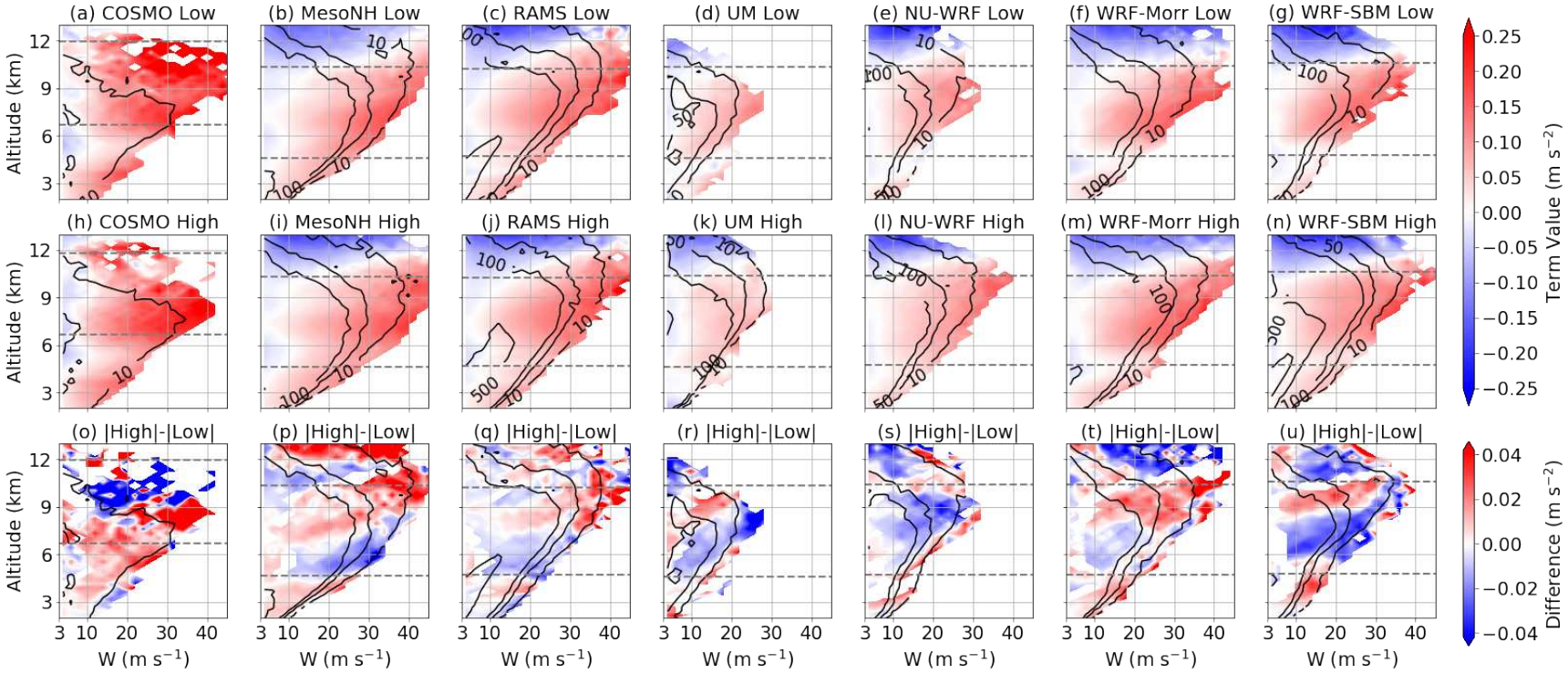

Figure 4.13. Same as Figure 4.10, but for the sum of the buoyancy terms – thermal buoyancy, moisture buoyancy and condensate loading (B_{NET}, B_{TH}+B_{WV}+B_{CL}).

d. Vertical perturbation pressure gradient (VPPG)

The VPPG term is generally weakly positive below ~6 km AGL, more strongly negative above ~6 km AGL in all of the Low-CCN and High-CCN simulations (Figure 4.14a-n). Importantly, it also has a similar magnitude to the B_{TH} and B_{CL} terms. This term has both buoyant and dynamic components (e.g., Klemp 1987). In the mixed-phase regions of the updrafts in these simulations, this term acts to oppose the net buoyancy (Figure 4.13a-n), which demonstrates a significant contribution from the buoyant component to the total VPPG term in these regions. As such, in many locations throughout the profiles, the VPPG differences between the High-CCN and Low-CCN simulations (Figure 4.14o-u) offsets the High – Low CCN differences in the net buoyancy term. However, these interactions between the VPPG and buoyancy terms vary amongst the models, and the relative contributions of these terms assist in explaining the diverging mean updraft response above 8 km AGL amongst the models.

Figure 4.15 shows the sum of the buoyancy and VPPG accelerations (B+VPPG). When assessing the differences between the High-CCN and Low-CCN simulations, four models have deep layers of weaker accelerations due to the B+VPPG term in the High-CCN simulations between 5 and 9 km AGL (MesoNH, RAMS, UM, WRF-SBM), three of which (MesoNH, RAMS, WRF-SBM) also have weaker mean updrafts above 8-9 km AGL in the High-CCN simulations (Figure 4.7). Alternatively, the NU-WRF and WRF-Morr models, which have similar patterns to the other models when only considering the net buoyancy, have a much noisier response to increased CCN concentrations in this 5-9 km AGL layer, as compared to the other models. These two models also have stronger updrafts above 8 km AGL. This result demonstrates that the VPPG term is important in terms of affecting the mean updraft response to varying CCN concentrations. This result is consistent with a recent study by Tao and Li (2016),

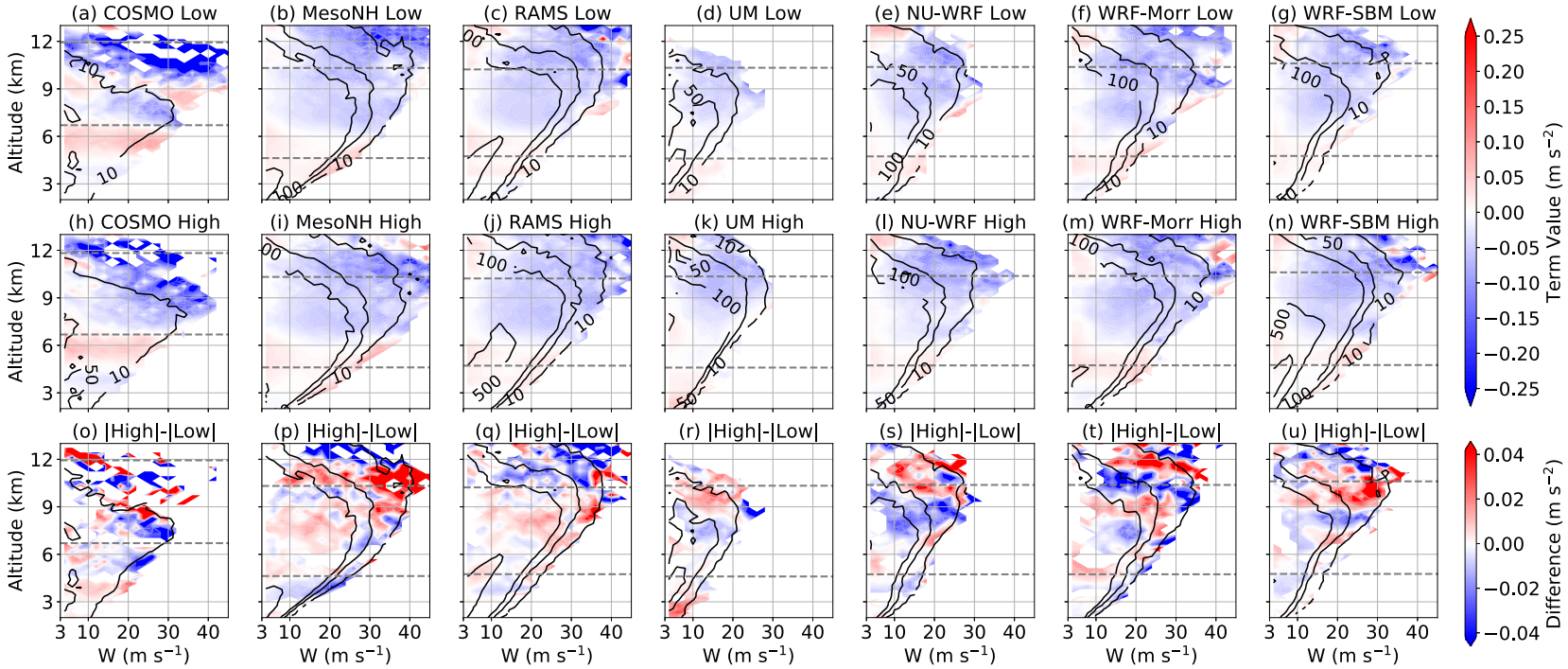

Figure 4.14. Same as Figure 4.10, but for the vertical perturbation pressure gradient (VPPG).

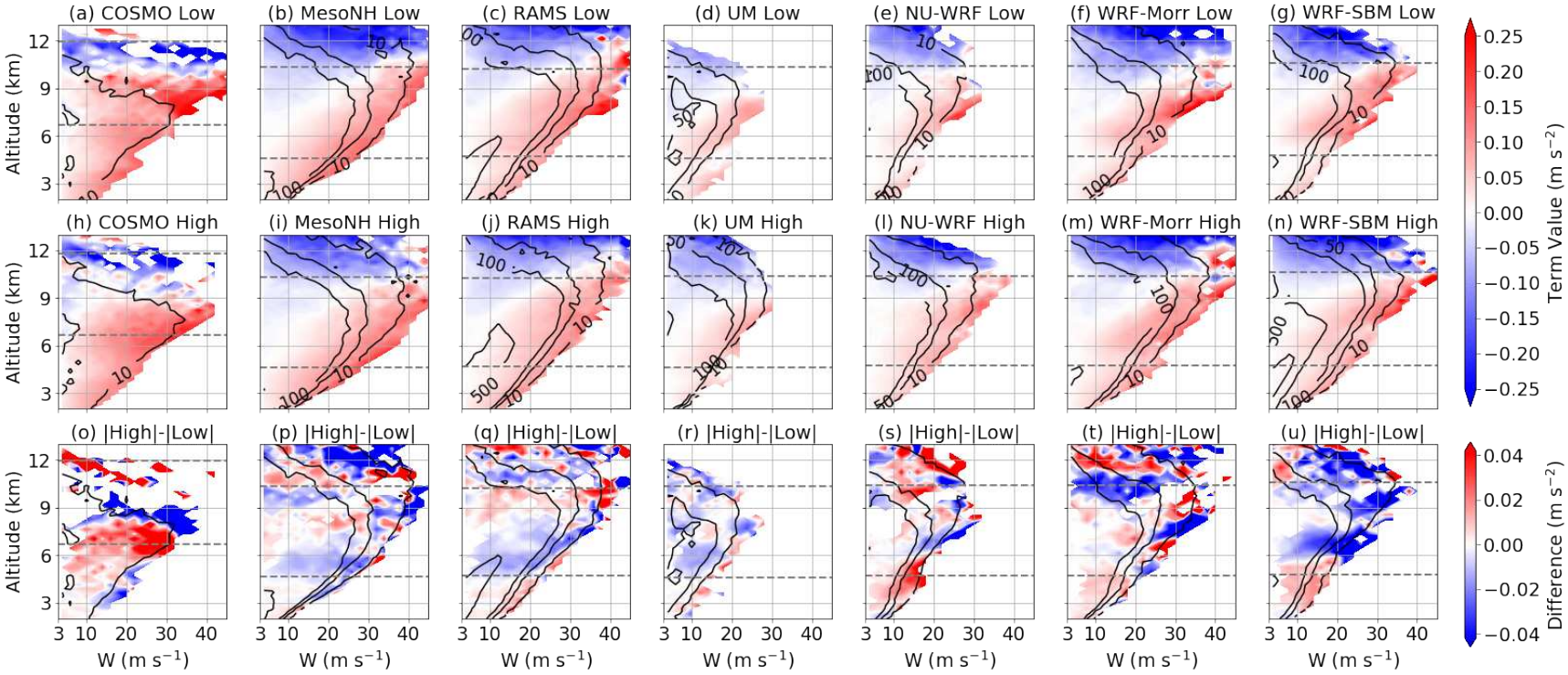

Figure 4.15. Same as Figure 4.10, but for the sum of the buoyancy terms and the vertical perturbation pressure gradient (B+VPPG).

which also concluded that the VPPG term needs to be considered when assessing aerosol impacts on deep convective clouds.

e. Advection terms

For completion, the analyses are shown for accelerations due to horizontal advection (HADV) and vertical advection (VADV) in Figures 4.16 and 4.17, respectively. The horizontal advection term (Figure 4.16) has negative values below and positive values above ~10 km AGL in both the Low-CCN and High-CCN simulations in all of the models and is generally weaker than most of the other terms. This is due to the counteraction of both positive and negative HADV accelerations, which are caused by the opposite gradients in w on the upwind and downwind sides of the updraft, respectively. Therefore, while locally this term can play a very significant role (see Figure 4.9) within the updraft when assessing the mean updraft response, this HADV term has a limited overall impact, except for the extreme upper levels of the updrafts.

In the mean updrafts, the accelerations associated with vertical advection (Figure 4.17) are much stronger than the accelerations associated with horizontal advection, a situation that is true for all of the models. The vertical advection term is negative below and positive above the altitude of the maximum updraft, where $\frac{\partial w}{\partial z}$ is positive and negative, respectively, in both the High- and Low-CCN cases. This term neutralizes the sum of the buoyancy and VPPG terms (Figure 4.15). This is due to the fact that the full lifecycle of updrafts is being assessed in this study, which captures both decaying and intensifying stages. Therefore, in the mean, $\frac{\partial w}{\partial t}$ will be close to zero, and thus, the VADV term will act to balance the sum of the other terms. While these advection terms are locally strong and are essential for closing the vertical velocity tendency equation, their interpretations in this analysis framework are extraneous.

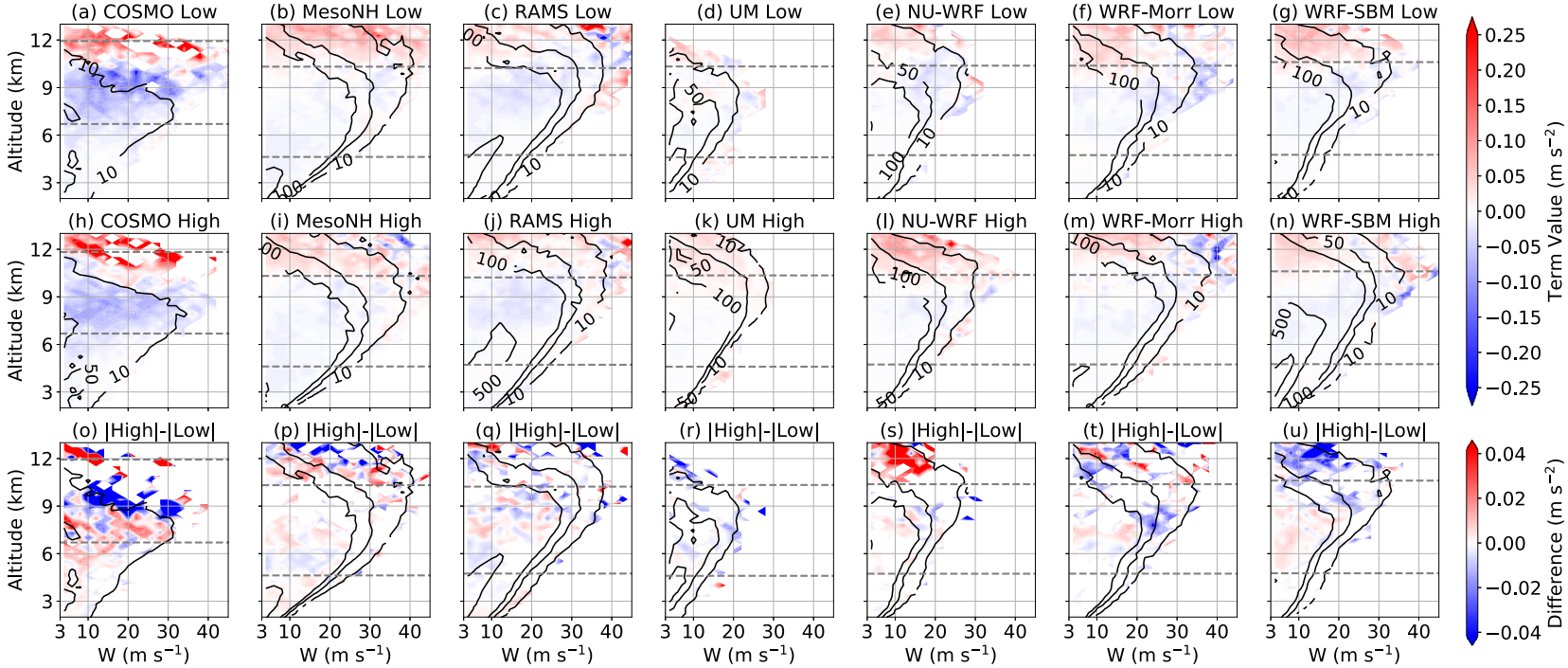

Figure 4.16. Same as Figure 4.10, but for the accelerations due to horizontal advection (HADV).

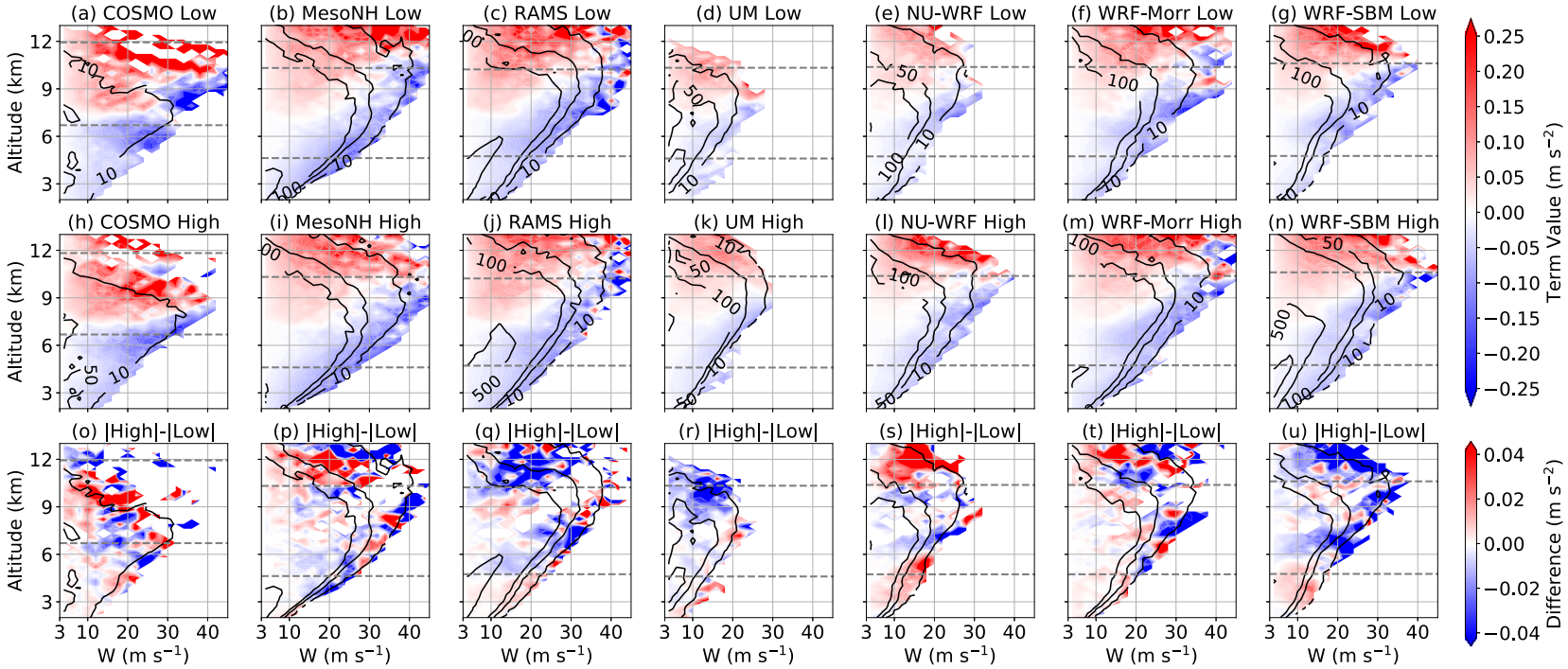

Figure 4.17. Same as Figure 4.10, but for accelerations due to vertical advection (VADV).

4.5 Conclusions

As part of the ACPC initiative, a MIP was organized and completed in order to assess the consistency of CCN impacts on deep convective clouds amongst seven state-of-the-art cloud-resolving models. The ACPC MIP represents the first time that an international, coordinated intercomparison study has been used to determine the robustness of simulated aerosol impacts on deep convective clouds. Seven models were used to simulate the same case study of isolated deep convective clouds near Houston, Texas with both relatively high and low initial CCN concentrations. Despite the many differences between the models and simulations (e.g., physical parameterizations, initial conditions), all the models produced deep convective clouds around Houston during the 12-hour period when convective clouds were observed for this case. Deep convective cloud updrafts were identified and compared between the High-CCN and Low-CCN simulations with the ultimate goal of determining the range of responses amongst the models in updraft amounts and intensity due to varying CCN concentrations. The terms of the vertical velocity tendency equation were also calculated and compared in order to attribute physical processes to the aerosol-induced updraft responses.

There were several consistent trends amongst the majority of models. Six of the seven models produced more frequent deep convective updrafts in the High-CCN simulations. All of the models produced stronger updrafts from 3-5 km AGL in the High-CCN simulations, which was due to enhanced condensational latent heating. Above 5 km AGL, the mean updraft differences between the High-CCN and Low-CCN simulations in most models waned. This was found to be due to the drying of the updrafts that resulted from the enhanced condensation and associated water vapor loss in the regions below. Because of this waning effect, all of the models either had no differences or slightly stronger mean updrafts in the High-CCN simulations

between ~5-8 km AGL. The condensate loading buoyancy term had similar signals in 5 of the 7 models, with enhanced condensate loading above the freezing level in the High-CCN simulations; however, all the models revealed that differences in condensate loading accelerations between the High-CCN and Low-CCN simulations were much smaller in magnitude than the differences in thermal buoyancy accelerations, and therefore, less impactful on the updraft responses to varying CCN concentrations.

Above 8 km AGL, the mean updraft response diverged in the models, with some models producing stronger updrafts and others weaker updrafts. To best explain this result, we had to consider the vertical pressure perturbation gradient (VPPG) term. Generally, while this term offsets the net buoyancy term, the relative magnitudes of the VPPG and buoyancy terms at the upper levels varied amongst the models, which resulted in the high variability of the mean updraft responses (both stronger and weaker updrafts in High-CCN conditions) at these upper levels. This result confirms the importance of assessing the VPPG term in aerosol-impact studies (Tao and Li 2016) and demonstrates the complex interactions associated with aerosol effects in the upper levels of deep convective updrafts.

While this study focused on mean updrafts over a 12-hour period, many studies have shown that the most significant and consistent CCN effects are at the initial stages of cloud development and that feedbacks to cold pools, convective anvils and the environment may modulate CCN effects at later times in a cloud's lifecycle (e.g., van den Heever et al. 2006; Tao et al. 2007). To assess the consistency of the aerosol impacts on cloud evolution and lifecycles in these ACPC MIP data, individual clouds should be identified and tracked. Recent software (Tracking and Object-Based Analysis of Clouds; tobac) has been developed for this purpose and tested with some of the ACPC MIP simulation data (Heikenfeld et al. 2019). Through tracking

individual clouds in this dataset, the robustness of aerosol impacts on the evolution of clouds for the ACPC MIP could be assessed.

In this study, each model was allowed to freely evolve through its model integration. While this better represents reality and how these models would typically operate, methods that fully constrain the dynamics (e.g., Grabowski 2015; Hill et al. 2015) would help address the question as to which processes in the various model parameterization are causing differences in the model responses. While this has been studied with a few model microphysical parameterizations, a more comprehensive model intercomparison study under such a framework would also be useful endeavor.

Lastly, while research focused on model comparisons is useful in determining the consistency of model responses, comprehensive observations of aerosol effects on deep convective clouds are needed to validate the complex mechanisms and responses proposed in modeling studies. This ACPC MIP assisted in motivating the Tracking Aerosol Convection Interactions ExpeRiment (TRACER, Jensen et al. 2018), which will take place in Houston, Texas in 2021-2022. The data from this field campaign will be very useful to assess the mechanisms proposed in this study.

CHAPTER 5: DISSERTATION CONCLUSIONS

5.1 Summary of studies

Uncertainties remain in the understanding and the model representation of processes governing aerosol-cloud interactions, particularly in deep convective clouds. Continued, innovative research in both modeling and observational areas will be needed in order to make advancements. In this dissertation, three studies related to aerosol particles, deep convective updrafts, and their interactions have been presented. The focus of the first two studies was on novel observations of aerosol particles and deep convective updrafts, respectively. In the third study, a comprehensive analysis of aerosol impacts within deep convective updrafts was performed in the framework of a model intercomparison study.

In Chapter 2, long-term observations of aerosol particle size distributions from the United States Department of Energy's Atmospheric Radiation Measurement's SGP site were utilized. Using the comprehensive aerosol observing platform available at the SGP site, the available aerosol size distribution data were harmonized and augmented to glean more information, particularly about the smallest particles (i.e., particles with diameters less than 30 nm). Unlike most intensive, in situ observations, which are typically only available during field campaigns that occur on the time scales of weeks and months, the five-year dataset that was analyzed in this study allowed for robust statistical analyses that fully described the aerosol particle size distributions and their temporal variability at a rural, continental, North American site. Seasonal size distributions were quantified and made available for future modeling studies that require representative aerosol size distributions in order to reproduce realistic aerosol-related processes. Analyses of these data's power spectra demonstrated that the smallest particles have consistent

diurnal cycles in every season, and therefore, these particles could play a more significant role in cloud processes than had previously been suggested. These smallest particles had their highest concentrations (on the order of 10^3-10^4 cm^{-3}) in the early afternoon and evening hours, and these cycles were more prevalent when afternoon and evening boundary layers were deeper. These long-term data corroborate recent field campaign results at the SGP site whereby new particle formation was initially observed in the free troposphere, and these newly-formed, small particles then mix down to the surface (Chen et al. 2019). This 5-year dataset also showed that particles with diameters between 140 and 800 nm had consistent diurnal cycles, which had their peak number concentrations overnight and were driven by organic and nitrate aerosol mass concentrations. Weaker cyclic signals were present for longer time scales (several day and week-long cycles). It was hypothesized that these cycles were related to the temporal variability of synoptic weather patterns, which follow similar cycles in this region.

While Chapter 2 was focused on surface in situ observations, Chapter 3 elevated the discourse to in situ observations above the surface, specifically within deep convective updrafts. Due to the hazardous sampling conditions, in situ observations within deep convective updrafts are scarce, and many of the current estimates of vertical velocities within deep convective updrafts are based on multi-Doppler analyses from ground-based radars and modeling studies, both of which have hard-to-characterize uncertainties. In Chapter 3, in situ observations from targeted radiosonde launches into the updrafts of supercellular deep convection during C^3LOUD-Ex (van den Heever et al. 2020) were presented. This field campaign occurred in 2016 – 2017 in Colorado, Wyoming and Nebraska. Updraft vertical velocities of up to 51 m s^{-1} were estimated from these radiosonde observations for the moderately unstable atmospheric conditions that were observed during C^3LOUD-Ex, suggesting that the vertical velocities within supercell updrafts in

more unstable regions (e.g., the U.S. southern Great Plains) are likely to be even higher than those observed during C^3LOUD-Ex. Radar data were used to provide important contextual information about the locations and conditions that were being sampled by the radiosondes. These radiosonde-based estimates of vertical velocities were also briefly compared to other methods that are often used to estimate the vertical velocities within deep convective updrafts. Comparisons between the radiosonde-based vertical velocity estimates with those from radar-based, dual-Doppler analyses suggest that the vertical velocities estimated from the C^3LOUD-Ex radars may not be able to capture the localized, most intense vertical velocities that were observed by the radiosondes. This study also demonstrated the benefits of coordinating radar scans with in situ observations, which not only provides important context for the in situ observations within updrafts but also contributes complementary estimates of vertical velocities within deep convective storms.

In Chapter 4, data from a model intercomparison project (MIP) that focused on aerosol effects on deep convective clouds were utilized to assess the range of responses in deep convective updrafts from increased CCN concentrations from seven state-of-the-art cloud-resolving models (van den Heever et al. 2018; www.acpcinitiative.org). This comparison study was organized within the Aerosol-Cloud-Precipitation-Climate Initiative, an international working group that is supported by the International Geosphere–Biosphere Programme (IGBP) and the World Climate Research Programme (WCRP) and focuses on reducing the uncertainties associated with aerosol-cloud interactions (ACPC Initiative; Rosenfeld et al. 2014). Seven modeling research groups participated in the ACPC MIP, and their models had many differences, including a wide range of physical parameterizations. For example, one of the seven models used spectral bin microphysics, while the rest of the models used two-moment microphysical

schemes. Furthermore, several models utilized supersaturation adjustment schemes, while the other models either diagnosed or prognosed supersaturation. All the models were used to simulate the same case study of isolated, scattered deep convective clouds near Houston, Texas with both high and low CCN concentrations within the boundary layer, the initial amounts of which were based on local observations. While the model simulations differed in terms of the timing, intensity, and frequency of convective clouds, all the simulations produced scattered deep convective clouds in the afternoon and evening hours.

The characteristics of these convective updrafts in the high-CCN and low-CCN conditions were compared for each model. Despite the significant differences in the microphysical, aerosol, land surface, radiation and turbulence parameterizations within these seven models, there were many consistent results. Six of the seven models produced more frequent convective updraft columns in high-CCN conditions throughout the simulation. In terms of the magnitude of convective updraft vertical velocities, in the simulations with relatively high CCN concentrations, all models produced stronger updraft vertical velocities (range of 5-25%) in the lower and middle tropospheric levels. However, in the upper levels of the updrafts (above ~8 km AGL), the models' responses to the high-CCN conditions diverged, with four models producing weaker updrafts and three models producing stronger updrafts. The terms of the vertical velocity tendency equation were analyzed to understand the processes causing these consistent and inconsistent signals. In all the models, the thermal buoyancy term was the dominant term in the lower and middle troposphere, while the condensate loading term played a secondary role in terms of differences between the high-CCN and low-CCN simulations. However, in the upper levels (above ~8 km AGL), the pressure gradient term, which has often been neglected in aerosol impact studies, played a significant role and helped to explain the

divergence in the mean updraft velocities amongst the models at these altitudes. The ACPC MIP is the first of its kind to examine the aerosol indirect effects on deep convective clouds (van den Heever et al. 2020), and its results have helped motivate the TRACER field campaign, which will take place in Houston, Texas in 2021-2022 (Jensen et al. 2019).

5.2 Implications of this research and future work

Building from the results presented in this dissertation, several additional research investigations could be pursued toward further advancements in the understanding of aerosol-cloud interactions within deep convective clouds. The SGP aerosol observations presented in Chapter 2 showed that throughout the year, there were consistent diurnal cycles in the concentrations of the smallest particles (particles with diameters < 30 nm) that peaked in the early afternoon and evening hours. Interestingly, this diurnal cycle is concurrent with the diurnal cycle of deep convective clouds over land (e.g., Soden et al. 2000), and therefore, it is possible that these high concentrations of small particles could have large impacts on deep convective clouds. It is unclear, however, whether deep convective clouds can produce the supersaturations needed for these small aerosol particles to form cloud droplets. For example, an aerosol particle with a diameter of 10 nm, which can sometimes be composed of ammonium sulfate (e.g., Hodshire et al. 2019), which has a hygroscopicity parameter of ~0.6 (e.g., Petters and Kreidenweis 2007), would require a supersaturation of over 5.0% (recall Figure 1.2 in the Introduction). Less hygroscopic substances can also be found in these small particles (e.g., Hodshire et al. 2019), which would require even larger supersaturations.

However, due to the inability to observe supersaturation values throughout deep convective clouds with in situ or remotely-sensed observations, models have been the primary

tools that have been used to estimate these supersaturation values. Idealized models, such as parcel models, have been most often used due to their simplicity and Lagrangian framework, which allow them to simulate processes at high spatial and temporal resolutions and produce accurate solutions. However, many parcel models do not represent the full spectrum of relevant processes with deep convective clouds (e.g., ice processes, collision coalescence, and precipitation scavenging), have not attempted to simulate very intense updraft conditions, and have prescribed vertical velocities, which do not allow for feedback processes (e.g., Reutter et al. 2009; Ghan et al. 2011). For example, results from Chapter 3 of this dissertation demonstrated that vertical velocities within deep convective clouds can reach 50 m s^{-1}, much larger than the 20 m s^{-1} tested in Reutter et al. (2009). A recent modeling study using a Eulerian cloud-resolving model suggested that deep convective updrafts can create high supersaturations that can nucleate these small aerosol particles (Fan et al. 2019). While cloud-resolving models, such as that used in Fan et al. (2019) include many of the complex cloud processes that are often neglected in parcel models, these complex models are limited by computational constraints and cannot represent the fine scales that can be represented in Lagrangian frameworks and that may be needed to reproduce realistic supersaturations (e.g., Morrison and Grabowski 2008). For example, the simulations in Fan et al. (2019) utilized a 3-s model time step and horizontal grid spacings of 500 m. As such, additional simulations that can better capture both the complexity of cloud processes and the localized updraft conditions with high temporal and spatial resolution are needed to better assess the amount of supersaturation that can develop in deep convective clouds and thus whether small aerosol particles can serve as CCN.

In Chapter 3, a comparison of supercell updraft vertical velocity estimates from the radiosonde data and from the radar-based, dual-Doppler analyses from the C^3LOUD-Ex field

campaign was presented. This comparison demonstrated that for those locations where the radiosonde observed the most intense vertical velocities, the dual-Doppler analyses generally produced vertical velocity estimates that were 15-20 m s^{-1} lower than the radiosonde-based estimates. The errors in the dual-Doppler analyses, however, were not assessed in this dissertation, and it is therefore difficult to determine how much of these differences were due to systematic biases between the two observational platforms as opposed to errors within the analyses. Observation system simulation experiments (OSSEs) have been shown to be a powerful tool towards determining the errors associated with multi-Doppler analyses in deep convective clouds (e.g., Potvin et al. 2012; Oue et al. 2019), but require producing realistic, case study simulations of the clouds of interest, including accurate representations of the structure, intensity and location of the convective clouds. One of the C^3LOUD-Ex cases presented in Chapter 3 has been recently simulated (van den Heever et al. 2020), and utilizing these simulation data in an OSSE framework would provide additional insights into the magnitude of the errors associated with dual-Doppler analyses of supercell updrafts, particularly with respect to the C^3LOUD-Ex results.

In Chapter 4, statistics from the ACPC MIP were used to gain insights into the range of responses in deep convective updrafts to increased CCN concentrations within different cloud-resolving models. While this study showed both consistencies and inconsistencies in the mean updraft responses throughout the duration of the convective event, it did not consider the evolution of individual clouds and updrafts and how this evolution may have changed with the varying CCN conditions. The concept that high concentrations of CCN would prolong the lifetime of warm-phased clouds with weak vertical motions due to suppressing precipitation processes was first suggested by Albrecht (1989), but it is unclear whether this concept holds for

deep convective clouds due to the more complicated processes and feedbacks present in deep convective clouds. To study the impacts of varying aerosol concentrations on the evolution of clouds, individual clouds must be identified and tracked within these simulation data. Recently advancements have been made in developing such tracking tools. For example, the *tobac* (Tracking and Object-Based Analysis of Clouds) software package has been developed and tested with both simulation and observational data from the ACPC model intercomparison study and made available via open-source platforms (Heikenfeld et al. 2019). An example of the cloud tracks from one of the ACPC MIP simulations is shown in Figure 5.1. With this tool or other similar tools, this extensive simulation dataset that has been created as part of the intermodal comparison study could be used to answer many additional questions including:

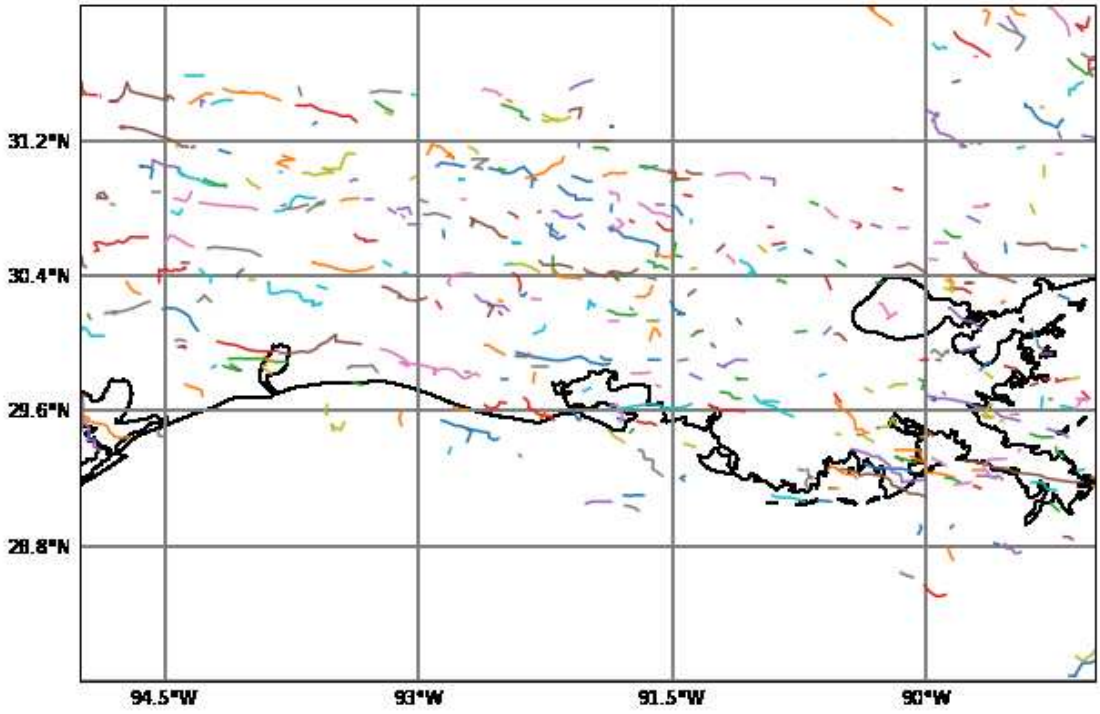

Figure 5.1. Tracks of convective clouds that were identified and tracked within one of the ACPC MIP simulations using tobac v1.2 (Heikenfeld et al. 2019). Figure provided by Max Heikenfeld.

1) What is the range of responses to increased CCN concentrations amongst the cloud-resolving models, in terms of cloud and updraft lifetimes?
2) When during the cloud lifetime are the most intense updrafts present, how does this change under the different CCN conditions, and how does the CCN response vary amongst the various models?
3) Similarly, when during the cloud lifetime is the most intense surface precipitation achieved, how does this change under the different CCN conditions, and how does the CCN response vary amongst the various models?

The results from the ACPC MIP dataset could provide both confidence in the robust signals that are simulated by the majority of models and guidance to where additional research is needed based on those inconsistent responses to the varying CCN concentrations.

While simulation data, such as those presented in Chapter 4, can answer many questions, particularly about the robustness of simulated responses to varying aerosol concentrations within a wide range of models, observations of aerosol-cloud interactions in deep convective clouds are also needed. The ACPC MIP assisted in motivating TRACER, a field campaign focused on deep convective cloud processes, including aerosol-cloud interactions (Jensen et al. 2019). TRACER will utilize a network of radars and other observational platforms to track individual convective clouds, similar to the tracking described above for the simulation data, and to develop 4-dimensional (i.e., three spatial dimensions and time) observational datasets of the evolution of individual clouds and their environments. The observations collected during TRACER will provide a unique dataset that is expected to either corroborate or contradict many of the model-based concepts of aerosol-cloud interactions within deep convective clouds and to ultimately reduce the uncertainties associated with the understanding of these processes.

REFERENCES

Abdul-Razzak, H., and S. J. Ghan (2000), A parameterization of aerosol activation: 2. Multiple aerosol types, *J. Geophys. Res.*, *105*(D5), 6837, doi:10.1029/1999JD901161.

Achenbach, E. (1972), Experiments on the flow past spheres at very high Reynolds numbers, *J. Fluid Mech.*, *54*(3), 565–575, doi:10.1017/S0022112072000874.

Albrecht, B. A. (1989), Aerosols, Cloud Microphysics, and Fractional Cloudiness, *Science (80-.).*, *245*(4923), 1227–1230, doi:10.1126/science.245.4923.1227.

Andreae, M. O., D. Rosenfeld, P. Artaxo, A. A. Costa, G. P. Frank, K. M. Longo, and M. A. F. Silva-Dias (2004), Smoking Rain Clouds over the Amazon, *Science (80-.).*, *303*(5662), 1337–1342, doi:10.1126/science.1092779.

Andrews, E., P. J. Sheridan, and J. A. Ogren (2011), Seasonal differences in the vertical profiles of aerosol optical properties over rural Oklahoma, *Atmos. Chem. Phys.*, *11*(20), 10661–10676, doi:10.5194/acp-11-10661-2011.

Andrews, E., P. J. Sheridan, J. A. Ogren, and R. Ferrare (2004), In situ aerosol profiles over the Southern Great Plains cloud and radiation test bed site: 1. Aerosol optical properties, *J. Geophys. Res. Atmos.*, *109*(D6), n/a-n/a, doi:10.1029/2003JD004025.

Armijo, L. (1969), A Theory for the Determination of Wind and Precipitation Velocities with Doppler Radars, *J. Atmos. Sci.*, *26*(3), 570–573, doi:10.1175/1520-0469(1969)026<0570:ATFTDO>2.0.CO;2.

Balakrishnan, N., and D. S. Zrnic (1990), Use of Polarization to Characterize Precipitation and Discriminate Large Hail, *J. Atmos. Sci.*, 47, 1525–1540, doi:10.1175/1520-0469(1990)047<1525:UOPTCP>2.0.CO;2..

Barnes, S. L. (1970), Some Aspects of a Severe, Right-Moving Thunderstorm Deduced from Mesonetwork Rawinsonde Observations, *J. Atmos. Sci.*, *27*(4), 634–648, doi:10.1175/1520-0469(1970)027<0634:SAOASR>2.0.CO;2.

Bell, M. M., M. T. Montgomery, and K. A. Emanuel (2012), Air–Sea Enthalpy and Momentum Exchange at Major Hurricane Wind Speeds Observed during CBLAST, *J. Atmos. Sci.*, *69*(11), 3197–3222, doi:10.1175/JAS-D-11-0276.1.

Best, M. J. et al. (2011), The Joint UK Land Environment Simulator (JULES), model description – Part 1: Energy and water fluxes, *Geosci. Model Dev.*, *4*(3), 677–699, doi:10.5194/gmd-4-677-2011.

Bluestein, H. B., E. W. McCaul, G. P. Byrd, and G. R. Woodall (1988), Mobile Sounding Observations of a Tornadic Storm near the Dryline: The Canadian, Texas Storm of 7 May 1986, *Mon. Weather Rev.*, *116*(9), 1790–1804, doi:10.1175/1520-0493(1988)116<1790:MSOOAT>2.0.CO;2.

Bluestein, H. B., E. W. McCaul, G. P. Byrd, G. R. Woodall, G. Martin, S. Keighton, and L. C. Showell (1989), Mobile Sounding Observations of a Thunderstorm near the Dryline: The Gruver, Texas Storm Complex of 25 May 1987, *Mon. Weather Rev.*, *117*(1), 244–250, doi:10.1175/1520-0493(1989)117<0244:MSOOAT>2.0.CO;2.

Bousquet, O., P. Tabary, and J. Parent du Châtelet (2008), Operational Multiple-Doppler Wind Retrieval Inferred from Long-Range Radial Velocity Measurements, *J. Appl. Meteorol. Climatol.*, *47*(11), 2929–2945, doi:10.1175/2008JAMC1878.1.

Browning, K. A., and F. H. Ludlam (1962), Airflow in convective storms, *Q. J. R. Meteorol. Soc.*, *88*(376), 117–135, doi:10.1002/qj.49708837602.

Browning, K. A., and G. B. Foote (1976), Airflow and hail growth in supercell storms and some implications for hail suppression, *Q. J. R. Meteorol. Soc.*, *102*(433), 499–533, doi:10.1002/qj.49710243303.

Brunkow, D., V. N. Bringi, P. C. Kennedy, S. A. Rutledge, V. Chandrasekar, E. A. Mueller, and R. K. Bowie (2000), A description of the CSU-CHILL National Radar Facility, *J. Atmos. Ocean. Technol.*, *17*(12), 1596–1608, doi:10.1175/1520-0426(2000)017<1596:ADOTCC>2.0.CO;2.

Bryan, G. H. (2008): getcape. https://www2.mmm.ucar.edu/people/bryan/Code/getcape.F(Accessed July 1, 2019).

Chen, F., and J. Dudhia (2001), Coupling an Advanced Land Surface–Hydrology Model with the Penn State–NCAR MM5 Modeling System. Part I: Model Implementation and Sensitivity, *Mon. Weather Rev.*, *129*(4), 569–585, doi:10.1175/1520-0493(2001)129<0569:CAALSH>2.0.CO;2.

Chen, H., A. L. Hodshire, J. Ortega, J. Greenberg, P. H. McMurry, A. G. Carlton, J. R. Pierce, D. R. Hanson, and J. N. Smith (2018), Vertically resolved concentration and liquid water content of atmospheric nanoparticles at the US DOE Southern Great Plains site, *Atmos. Chem. Phys.*, *18*(1), 311–326, doi:10.5194/acp-18-311-2018.

Chisholm, A. J. (1973), Alberta Hailstorms Part I: Radar Case Studies and Airflow Models, in *Alberta Hailstorms*, vol. 53, pp. 1–36, American Meteorological Society, Boston, MA.

Clark, D. B. et al. (2011), The Joint UK Land Environment Simulator (JULES), model description – Part 2: Carbon fluxes and vegetation dynamics, *Geosci. Model Dev.*, *4*(3), 701–722, doi:10.5194/gmd-4-701-2011.

Collins, D. (2010), Tandem Differential Mobility Analyzer/ Aerodynamic Particular Sizer (APS) Handbook,

Collis, S., A. Protat, and K.-S. Chung (2010), The Effect of Radial Velocity Gridding Artifacts on Variationally Retrieved Vertical Velocities, *J. Atmos. Ocean. Technol.*, *27*(7), 1239–1246, doi:10.1175/2010JTECHA1402.1.

Cooper, W. A. (1986), Ice Initiation in Natural Clouds, Meteorol. Monogr., 43, 29–32, doi:10.1175/0065-9401-21.43.29.

Cotton, W. R. et al. (2003), RAMS 2001: Current status and future directions, *Meteorol. Atmos. Phys.*, *82*(1), 5–29, doi:10.1007/s00703-001-0584-9.

Cuxart, J., P. Bougeault, and J. L. Redelsperger (2000), A turbulence scheme allowing for mesoscale and large-eddy simulations, Q. J. R. Meteorol. Soc., 126(562), 1–30, doi:10.1002/qj.49712656202.

Dahl, N. A., A. Shapiro, C. K. Potvin, A. Theisen, J. G. Gebauer, A. D. Schenkman, and M. Xue (2019), High-Resolution, Rapid-Scan Dual-Doppler Retrievals of Vertical Velocity in a Simulated Supercell, *J. Atmos. Ocean. Technol.*, *36*(8), 1477–1500, doi:10.1175/jtech-d-18-0211.1.

Dal Maso, M. (2005), Formation and Growth of Fresh Atmospheric Aerosols Eight Years of Aerosol Size Distribution Data From SMEAR, *Boreal Environ. Res.*, *10*(October 2005), 323–336.

Davies-Jones, R. P. (1974), Discussion of Measurements inside High-Speed Thunderstorm Updrafts, *J. Appl. Meteorol.*, *13*(6), 710–717, doi:10.1175/1520-0450(1974)013<0710:DOMIHS>2.0.CO;2.

Davies-Jones, R. P., and J. H. Henderson (1975), Updraft properties deduced statistically from Rawin soundings, *Pure Appl. Geophys. PAGEOPH*, *113*(1), 787–801, doi:10.1007/BF01592959.

Delene, D. J., and J. A. Ogren (2002), Variability of Aerosol Optical Properties at Four North American Surface Monitoring Sites, *J. Atmos. Sci.*, *59*(6), 1135–1150, doi:10.1175/1520-0469(2002)059<1135:VOAOPA>2.0.CO;2.

Delle Monache, L., K. D. Perry, R. T. Cederwall, and J. A. Ogren (2004), In situ aerosol profiles over the Southern Great Plains cloud and radiation test bed site : 2 . Effects of mixing height on aerosol properties, , *109*, 1–9, doi:10.1029/2003JD004024.

DeMott, P. J., A. J. Prenni, X. Liu, S. M. Kreidenweis, M. D. Petters, C. H. Twohy, M. S. Richardson, T. Eidhammer, and D. C. Rogers (2010), Predicting global atmospheric ice nuclei distributions and their impacts on climate, *Proc. Natl. Acad. Sci.*, *107*(25), 11217–11222, doi:10.1073/pnas.0910818107.

DiGangi, E. A., D. R. MacGorman, C. L. Ziegler, D. Betten, M. Biggerstaff, M. Bowlan, and C. K. Potvin (2016), An overview of the 29 May 2012 Kingfisher supercell during DC3, *J. Geophys. Res*., 121, 14316–14343, doi:10.1002/2016JD025690.

DISCOVER-AQ Science Team, Hampton, VA, USA: NASA Atmospheric Science Data Center (ASDC), accessed 30 August 2017 at doi: 10.5067/Aircraft/DISCOVER-AQ/Aerosol-TraceGas

Dolan, B., and S. a. Rutledge (2010), Using CASA IP1 to Diagnose Kinematic and Microphysical Interactions in a Convective Storm, *Mon. Weather Rev.*, *138*(5), 1613–1634, doi:10.1175/2009MWR3016.1.

Edwards, J. M., and A. Slingo (1996), Studies with a flexible new radiation code. I: Choosing a configuration for a large-scale model, Q. J. R. Meteorol. Soc., 122(531), 689–719, doi:10.1256/smsqj.53106.

Fan, J., R. Zhang, G. Li, and W. K. Tao (2007), Effects of aerosols and relative humidity on cumulus clouds, J. Geophys. Res. Atmos., 112(14), 1–15, doi:10.1029/2006JD008136.

Fan, J., T. Yuan, J. M. Comstock, S. Ghan, A. Khain, L. R. Leung, Z. Li, V. J. Martins, and M. Ovchinnikov (2009), Dominant role by vertical wind shear in regulating aerosol effects on deep convective clouds, *J. Geophys. Res.*, *114*(D22), D22206, doi:10.1029/2009JD012352.

Fan, J., D. Rosenfeld, Y. Ding, L. R. Leung, and Z. Li (2012a), Potential aerosol indirect effects on atmospheric circulation and radiative forcing through deep convection, Geophys. Res. Lett. 39: Article No. L09806. doi:10.1029/2012GL051851

Fan, J., L. R. Leung, Z. Li, H. Morrison, H. Chen, Y. Zhou, Y. Qian, and Y. Wang (2012b), Aerosol impacts on clouds and precipitation in eastern China: Results from bin and bulk microphysics, *J. Geophys. Res. Atmos.*, *117*(D16), n/a–n/a, doi:10.1029/2011JD016537Fan, J., Y. Wang, D. Rosenfeld, and X. Liu (2016), Review of Aerosol–Cloud Interactions: Mechanisms, Significance, and Challenges, *J. Atmos. Sci.*, *73*(11), 4221–4252, doi:10.1175/JAS-D-16-0037.1.

Fan, J. et al. (2017), Cloud-resolving model intercomparison of an MC3E squall line case: Part I—Convective updrafts, *J. Geophys. Res. Atmos.*, *122*(17), 9351–9378, doi:10.1002/2017JD026622.

Fan, J. et al. (2019), Substantial convection and precipitation enhancements by ultrafine aerosol particles, *Science (80).*, *359*(6374), 411–418, doi:10.1126/science.aan8461.

Farley, R. E. (2005). "BalloonAscent: 3-D simulation tool for the ascent and float of high-altitude balloons." AIAA Aviation, Technology Integration and Operations Conf., American Institute of Aeronautics and Astronautics, Reston, VA, 1–15.

Foote, G. B., and J. C. Fankhauser (1973), Airflow and Moisture Budget Beneath a Northeast Colorado Hailstorm, *J. Appl. Meteorol.*, *12*(8), 1330–1353, doi:10.1175/1520-0450(1973)012<1330:aambba>2.0.co;2.

Fouquart, Y., and B. Bonnel (1980), Computations of Solar Heating of the Earth's Atmosphere—A New Parameterization., *Beitrage zur Phys. der Atmosphare*, (53), 35–62.

Fridlind, A. M. et al. (2004), Evidence for the predominance of mid-tropospheric aerosols as subtropical anvil cloud nuclei., *Science*, *304*(5671), 718–22, doi:10.1126/science.1094947.

Fridlind, A. M. et al. (2017), Derivation of aerosol profiles for MC3E convection studies and use in simulations of the 20 May squall line case, *Atmos. Chem. Phys.*, *17*(9), 5947–5972, doi:10.5194/acp-17-5947-2017.

Gal-Chen, T., and R. C. . Somerville (1975), On the use of a coordinate transformation for the solution of the Navier-Stokes equations, J. Comput. Phys., 17(2), 209–228, doi:10.1016/0021-9991(75)90037-6.

Gal-Chen, T. (1978), A Method for the Initialization of the Anelastic Equations: Implications for Matching Models with Observations, *Mon. Weather Rev.*, *106*(5), 587–606, doi:10.1175/1520-0493(1978)106<0587:amftio>2.0.co;2.

Gallice, A., F. G. Wienhold, C. R. Hoyle, F. Immler, and T. Peter (2011), Modeling the ascent of sounding balloons: Derivation of the vertical air motion, *Atmos. Meas. Tech.*, *4*(10), 2235–2253, doi:10.5194/amt-4-2235-2011.

Gao, J., M. Xue, A. Shapiro, and K. K. Droegemeier (1999), A variational method for the analysis of three-dimensional wind fields from two Doppler radars, *Mon. Weather Rev.*, *127*(9), 2128–2142, doi:10.1175/1520-0493(1999)127<2128:AVMFTA>2.0.CO;2.

Gasparini, R., D. R. Collins, E. Andrews, P. J. Sheridan, J. a. Ogren, and J. G. Hudson (2006), Coupling aerosol size distributions and size-resolved hygroscopicity to predict humidity-dependent optical properties and cloud condensation nuclei spectra, *J. Geophys. Res.*, *111*(D5), D05S13, doi:10.1029/2005JD006092.

Gebhart, K. a, S. M. Kreidenweis, and W. C. Malm (2001), Back-trajectory analyses of fine particulate matter measured at Big Bend National Park in the historical database and the 1996 scoping study, *Sci. Total Environ.*, *276*(1–3), 185–204, doi:10.1016/S0048-9697(01)00779-3.

Geerts, B. et al. (2018), Recommendations for in situ and remote sensing capabilities in atmospheric convection and turbulence, *Bull. Am. Meteorol. Soc.*, *99*(12), 2463–2470, doi:10.1175/BAMS-D-17-0310.1.

Ghan, S. J., H. Abdul-Razzak, A. Nenes, Y. Ming, X. Liu, M. Ovchinnikov, B. Shipway, N. Meskhidze, J. Xu, and X. Shi (2011), Droplet nucleation: Physically-based

parameterizations and comparative evaluation, *J. Adv. Model. Earth Syst.*, *3*(4), 1–34, doi:10.1029/2011MS000074.

Gilman, D. L., F. J. Fuglister, and J. M. Mitchell (1963), On the Power Spectrum of "Red Noise," *J. Atmos. Sci.*, *20*(2), 182–184, doi:10.1175/1520-0469(1963)020<0182:OTPSON>2.0.CO;2.

Grabowski, W. W. (2014), Extracting microphysical impacts in large-eddy simulations of shallow convection, *J. Atmos. Sci.*, *71*(12), 4493–4499, doi:10.1175/JAS-D-14-0231.1.

Grabowski, W. W. (2015), Untangling microphysical impacts on deep convection applying a novel modeling methodology, *J. Atmos. Sci.*, *72*(6), 2446–2464, doi:10.1175/JAS-D-14-0307.1.

Grabowski, W. W., and H. Morrison (2017), Modeling condensation in deep convection, *J. Atmos. Sci.*, *74*(7), 2247–2267, doi:10.1175/JAS-D-16-0255.1.

Grant, L. D., and S. C. Van Den Heever (2014), Aerosol-cloud-land surface interactions within tropical sea breeze convection, *J. Geophys. Res.*, *119*(13), 8340–8361, doi:10.1002/2014JD021912.

Grant, L. D., and S. C. van den Heever (2015), Cold pool and precipitation responses to aerosol loading: Modulation by dry layers, *J. Atmos. Sci.*, *72*(4), 1398–1408, doi:10.1175/JAS-D-14-0260.1.

Grosvenor, D. P., P. R. Field, A. A. Hill, and B. J. Shipway (2017), The relative importance of macrophysical and cloud albedo changes for aerosol-induced radiative effects in closed-cell stratocumulus: Insight from the modelling of a case study, Atmos. Chem. Phys., 17(8), 5155–5183, doi:10.5194/acp-17-5155-2017.

Hallar, A. G., D. H. Lowenthal, G. Chirokova, R. D. Borys, and C. Wiedinmyer (2011), Persistent daily new particle formation at a mountain-top location, *Atmos. Environ.*, *45*(24), 4111–4115, doi:10.1016/j.atmosenv.2011.04.044.

Halliwell, C. (2015), Subgrid turbulence scheme, Unified Model documentation paper 028, Met Office.

Hand, J. L., S. M. Kreidenweis, D. Eli Sherman, J. L. Collett, S. V. Hering, D. E. Day, and W. C. Malm (2002), Aerosol size distributions and visibility estimates during the Big Bend Regional Aerosol and Visibility Observational (BRAVO) study, *Atmos. Environ.*, *36*(32), 5043–5055, doi:10.1016/S1352-2310(02)00568-X.

Hansen, J., M. Sato, and R. Ruedy (1997), Radiative forcing and climate response, *J. Geophys. Res. Atmos.*, *102*(D6), 6831–6864, doi:10.1029/96JD03436.

Harrington, J. Y. (1997), The Effects of Radiative and Microphysical processes on simulated warm and transition season artic stratus, 289.

Heever, S. C. Van Den, A. M. F. Deep, and C. Cloud (2017), Aerosol-Cloud-Precipitation-Climate (ACPC) Initiative : Deep Convective Cloud Group Roadmap Updated : October 2017, , (October).

Heikenfeld, M., P. J. Marinescu, M. Christensen, D. Watson-Parris, F. Senf, S. C. Van Den Heever, and P. Stier (2019), Tobac 1.2: Towards a flexible framework for tracking and analysis of clouds in diverse datasets, *Geosci. Model Dev.*, *12*(11), 4551–4570, doi:10.5194/gmd-12-4551-2019.

Heise, E., B. Ritter, and R. Schrodin (2006), Consortium for Small- Scale Modelling: Technical report 9, , (July), 20.

Helmus, J. J., and S. M. Collis (2016), The Python ARM Radar Toolkit (Py-ART), a Library for Working with Weather Radar Data in the Python Programming Language, *J. Open Res. Softw.*, *4*, doi:10.5334/jors.119.

Heymsfield, A. J., and D. J. Musil (1982), Case study of a hailstorm in Colorado. Part II: particle growth processes at mid-levels deduced from in-situ measurements., *J. Atmos. Sci.*, *39*(12), 2847–2866, doi:10.1175/1520-0469(1982)039<2847:CSOAHI>2.0.CO;2.

Heymsfield, A. J., A. Bansemer, and C. H. Twohy (2007), Refinements to ice particle mass dimensional and terminal velocity relationships for ice clouds. Part I: Temperature dependence, *J. Atmos. Sci.*, *64*(4), 1047–1067, doi:10.1175/JAS3890.1.

Hill, A. A., B. J. Shipway, and I. A. Boutle (2015), How sensitive are aerosol-precipitation interactions to the warm rain representation?, *J. Adv. Model. Earth Syst.*, *7*(3), 987–1004, doi:10.1002/2014MS000422.

Hodshire, A. L. et al. (2016), Multiple new-particle growth pathways observed at the US DOE Southern Great Plains field site, *Atmos. Chem. Phys.*, *16*(14), 9321–9348, doi:10.5194/acp-16-9321-2016.

Hong, S. Y., Y. Noh, and J. Dudhia (2006), A new vertical diffusion package with an explicit treatment of entrainment processes, *Mon. Weather Rev.*, *134*(9), 2318–2341, doi:10.1175/MWR3199.1.

Hoose, C., and O. Möhler (2012), *Heterogeneous ice nucleation on atmospheric aerosols: A review of results from laboratory experiments*.

Iacono, M. J., J. S. Delamere, E. J. Mlawer, M. W. Shephard, S. A. Clough, and W. D. Collins (2008), Radiative forcing by long-lived greenhouse gases: Calculations with the AER radiative transfer models, *J. Geophys. Res. Atmos.*, *113*(13), 2–9, doi:10.1029/2008JD009944.

InterMet Systems, 2016: iMet-1-ABxn Data Sheet. Grand Rapids Michigan, 1 pp. 690 https://www.intermetsystems.com/ee/pdf/202060_iMet-1-ABxn_Data_161006.pdf..

Jefferson, A., D. Hageman, H. Morrow, F. Mei, and T. Watson (2017), Seven years of aerosol scattering hygroscopic growth measurements from SGP: Factors influencing water uptake, *J. Geophys. Res. Atmos.*, *122*(17), 9451–9466, doi:10.1002/2017JD026804.

Jensen, M. P. (2019), Tracking Aerosol Convection Interactions ExpeRiment (TRACER) Science Plan, *Doe Osti.Gov*, (June), doi:10.2172/1561242.

Khain, A. P., A. Pokrovsky, M. Pinsky, A. Seifert, and V. Phillips (2004), Simulation of Effects of Atmospheric Aerosols on Deep Turbulent Convective Clouds Using a Spectral Microphysics Mixed-Phase Cumulus Cloud Model. Part I: Model Description and Possible Applications, *J. Atmos. Sci.*, *61*(24), 2963–2982, doi:10.1175/JAS-3350.1.

Khain, A. P., D. Rosenfeld, and A. Pokrovsky (2005), Aerosol impact on the dynamics and microphysics of deep convective clouds, *Q. J. R. Meteorol. Soc.*, *131*(611), 2639–2663, doi:10.1256/qj.04.62.

Khain, A. P., N. BenMoshe, and A. Pokrovsky (2008), Factors Determining the Impact of Aerosols on Surface Precipitation from Clouds: An Attempt at Classification, *J. Atmos. Sci.*, *65*(6), 1721–1748, doi:10.1175/2007JAS2515.1.

Khain, A. P., L. R. Leung, B. Lynn, and S. Ghan (2009), Effects of aerosols on the dynamics and microphysics of squall lines simulated by spectral bin and bulk parameterization schemes, *J. Geophys. Res. Atmos.*, *114*(22), 1–21, doi:10.1029/2009JD011902.

Khain, A. P. et al. (2015), Representation of microphysical processes in cloud-resolving models: Spectral (bin) microphysics versus bulk parameterization, *Rev. Geophys.*, *53*(2), 247–322, doi:10.1002/2014RG000468.

Klemp, J. B., and R. B. Wilhelmson (1978), The Simulation of Three-Dimensional Convective Storm Dynamics, *J. Atmos. Sci.*, *35*(6), 1070–1096, doi:10.1175/1520-0469(1978)035<1070:TSOTDC>2.0.CO;2.

Klemp, J. B., R. B. Wilhelmson, and P. S. Ray (1981), Observed and numerically simulated structure of a mature supercell thunderstorm (Del City, Oklahoma)., *J. Atmos. Sci.*, *38*(8), 1558–1580, doi:10.1175/1520-0469(1981)038<1558:OANSSO>2.0.CO;2.

Köhler, H. (1936), The nucleus in and the growth of hygroscopic droplets, *Trans. Faraday Soc.*, *32*(1152), 1152–1161, doi:10.1039/TF9363201152.

Kropfli, R. A., and L. J. Miller (1976), Kinematic Structure and Flux Quantities in a Convective Storm From Dual-Doppler Radar Observations., *J. Atmos. Sci.*, *33*(3), 520–529, doi:10.1175/1520-0469(1976)033<0520:KSAFQI>2.0.CO;2.

Lac, C. et al. (2018), *Overview of the Meso-NH model version 5.4 and its applications*.

Langhans, W., J. Schmidli, and C. Schär (2012), Bulk convergence of cloud-resolving simulations of moist convection over complex terrain, *J. Atmos. Sci.*, 69(7), 2207–2228, doi:10.1175/JAS-D-11-0252.1.

Lanicci, J. M., and T. T. Warner (1991), A Synoptic Climatology of the Elevated Mixed-Layer Inversion over the Southern Great Plains in Spring. Part II: The Life Cycle of the Lid, *Weather Forecast.*, *6*(2), 198–213, doi:10.1175/1520-0434(1991)006<0198:ASCOTE>2.0.CO;2.

Lebo, Z. J., and J. H. Seinfeld (2011), Theoretical basis for convective invigoration due to increased aerosol concentration, *Atmos. Chem. Phys.*, *11*(11), 5407–5429, doi:10.5194/acp-11-5407-2011.

Lebo, Z. J., H. Morrison, and J. H. Seinfeld (2012), Are simulated aerosol-induced effects on deep convective clouds strongly dependent on saturation adjustment?, *Atmos. Chem. Phys.*, *12*(20), 9941–9964, doi:10.5194/acp-12-9941-2012.

Lebo, Z. J. (2014), The Sensitivity of a Numerically Simulated Idealized Squall Line to the Vertical Distribution of Aerosols, *J. Atmos. Sci.*, *71*(12), 4581–4596, doi:10.1175/JAS-D-14-0068.1.

Lee, S. S., L. J. Donner, V. T. J. Phillips, and Y. Ming (2008), The dependence of aerosol effects on clouds and precipitation on cloud-system organization, shear and stability, *J. Geophys. Res.*, *113*(D16), D16202, doi:10.1029/2007JD009224.

Lehmiller, G. S., H. B. Bluestein, P. J. Neiman, F. M. Ralph, and W. F. Feltz (2001), Wind structure in a supercell thunderstorm as measured by a UHF wind profiler, *Mon. Weather Rev.*, *129*(8), 1968–1986, doi:10.1175/1520-0493(2001)129<1968:WSIAST>2.0.CO;2.

Leith, C. E. (1973), The Standard Error of Time-Average Estimates of Climatic Means, *J. Appl. Meteorol.*, *12*(6), 1066–1069, doi:10.1175/1520-0450(1973)012<1066:TSEOTA>2.0.CO;2.

Li, G., Y. Wang, and R. Zhang (2008), Implementation of a two-moment bulk microphysics scheme to the WRF model to investigate aerosol-cloud interaction, *J. Geophys. Res. Atmos.*, *113*(15), 1–21, doi:10.1029/2007JD009361.

Liu, S., and X. Z. Liang (2010), Observed diurnal cycle climatology of planetary boundary layer height, *J. Clim.*, *23*(21), 5790–5809, doi:10.1175/2010JCLI3552.1.

Lock, A., Edwards, J., and Boutle, I. (2015): The parameterisation of boundary layer processes, Unified Model documentation paper 024, Met Office.

Loney, M. L., D. S. Zrnić, J. M. Straka, and A. V. Ryzhkov (2002), Enhanced polarimetric radar signatures above the melting level in a supercell storm, *J. Appl. Meteorol.*, *1*(V), 1179–1194, doi:10.1109/IGARSS.2002.1025018.

Luce, H., and H. Hashiguchi (2019), On the estimation of vertical air velocity and detection of atmospheric turbulence from the ascent rate of balloon soundings, , (September).

Mahish, M., A. Jefferson, and D. Collins (2017), Influence of common assumptions regarding aerosol composition and mixing state on predicted CCN concentration, *Atmos. Chem. Phys. Discuss.*, 1–22, doi:10.5194/acp-2017-516.

Marinescu, P. J., S. C. van den Heever, S. M. Saleeby, and S. M. Kreidenweis (2016), The microphysical contributions to and evolution of latent heating profiles in two MC3E MCSs, *J. Geophys. Res. Atmos.*, *121*(13), 7913–7935, doi:10.1002/2016JD024762.

Marinescu, P. J., S. C. van den Heever, S. M. Saleeby, S. M. Kreidenweis, and P. J. DeMott (2017), The Microphysical Roles of Lower-Tropospheric versus Midtropospheric Aerosol Particles in Mature-Stage MCS Precipitation, *J. Atmos. Sci.*, *74*(11), 3657–3678, doi:10.1175/JAS-D-16-0361.1.

Marinescu, P. J., E. J. T. Levin, D. Collins, S. M. Kreidenweis, and S. C. Van Den Heever (2019a), Quantifying aerosol size distributions and their temporal variability in the Southern Great Plains, USA, *Atmos. Chem. Phys.*, *19*(18), 11985–12006, doi:10.5194/acp-19-11985-2019.

Marinescu, P. J., Levin, E. J. T., Collins, D., and Kreidenweis, S. M. (2019b), SGP Merged Aerosol Size Distribution (CPC + SMPS + APS), U.S. Department of Energy ARM Data Center, Oak Ridge, Tennessee, USA, https://doi.org/10.5439/1511037.

Marinescu, P.J., P. C. Kennedy, M. M. Bell, A. J. Drager, L. D. Grant, S. W. Freeman, and S. C. van den Heever (2020a): Updraft Vertical Velocity Observations and Uncertainties in High Plains Supercells Using Radiosondes and Radars. In review at *Mon. Wea. Rev.*

Marinescu, P.J. and coauthors (2020b): The Impacts of Varying Cloud Condensation Nuclei on Deep Convective Cloud Updrafts -- A Multimodel Assessment. In preparation for J. Geophys. Res. Atmos.

Markowski, P. M., Y. P. Richardson, S. J. Richardson, and A. Petersson (2018), Aboveground thermodynamic observations in convective storms from balloonborne probes acting as pseudo-lagrangian drifters, *Bull. Am. Meteorol. Soc.*, *99*(4), 711–724, doi:10.1175/BAMS-D-17-0204.1.

Marshall, T. C., W. D. Rust, and M. Stolzenburg (1995), Electrical structure and updraft speeds in thunderstorms over the southern Great Plains, *J. Geophys. Res. Atmos.*, *100*(D1), 1001–1015, doi:10.1029/94JD02607.

Marshall, T. C., W. D. Rust, and M. Stolzenburg (1995), Electrical structure and updraft speeds in thunderstorms over the southern Great Plains, *J. Geophys. Res. Atmos.*, *100*(D1), 1001–1015, doi:10.1029/94JD02607.

Marwitz, J. D. (1972), The Structure and Motion of Severe Hailstorms. Part I: Supercell Storms, *J. Appl. Meteorol.*, *11*(1), 166–179, doi:10.1175/1520-0450(1972)011<0166:TSAMOS>2.0.CO;2.

Marwitz, J. D. (1973), Trajectories Within the Weak Echo Regions of Hailstorms, *J. Appl. Meteorol.*, *12*(7), 1174–1182, doi:10.1175/1520-0450(1973)012<1174:TWTWER>2.0.CO;2.

Marwitz, J. D., and E. X. Berry (1971), The Airflow Within the Weak Echo Region of an Alberta Hailstorm, *J. Appl. Meteorol.*, *10*(3), 487–492, doi:10.1175/1520-0450(1971)010<0487:TAWTWE>2.0.CO;2.

Maso, M. D. et al. (2007), Aerosol size distribution measurements at four Nordic field stations: identification, analysis and trajectory analysis of new particle formation bursts, *Tellus B Chem. Phys. Meteorol.*, *59*(3), 350–361, doi:10.1111/j.1600-0889.2007.00267.x.

Masson, V. et al. (2013), The SURFEXv7.2 land and ocean surface platform for coupled or offline simulation of earth surface variables and fluxes, *Geosci. Model Dev.*, *6*(4), 929–960, doi:10.5194/gmd-6-929-2013.

Matsui, T., S. Q. Zhang, S. E. Lang, W. K. Tao, C. Ichoku, and C. D. Peters-Lidard (2018), Impact of radiation frequency, precipitation radiative forcing, and radiation column aggregation on convection-permitting West African monsoon simulations, Clim. Dyn., 0(0), 1–21, doi:10.1007/s00382-018-4187-2.

McMurry, P. H., and S. K. Friedlander (1979), New particle formation in the presence of an aerosol, *Atmos. Environ.*, *13*(12), 1635–1651, doi:10.1016/0004-6981(79)90322-6.

Meyers, M. P., R. L. Walko, J. Y. Harrington, and W. R. Cotton (1997), New RAMS cloud microphysics parameterization. Part II: The two-moment scheme, *Atmos. Res.*, *45*(1), 3–39, doi:10.1016/S0169-8095(97)00018-5.

Meyers, M. P., P. J. DeMott, and W. R. Cotton (1992), New Primary Ice-Nucleation Parameterizations in an Explicit Cloud Model, *J. Appl. Meteorol.*, *31*, 708–721, doi:10.1175/1520-0450(1992)031<0708:NPINPI>2.0.CO;2.

Michalsky, J., F. Denn, C. Flynn, G. Hodges, P. Kiedron, A. Koontz, J. Schlemmer, and S. E. Schwartz (2010), Climatology of aerosol optical depth in north-central Oklahoma: 1992–2008, *J. Geophys. Res.*, *115*(D7), D07203, doi:10.1029/2009JD012197.

Miller, L. J. (1975), Internal airflow of a convective storm from dual-Doppler radar measurements, *Pure Appl. Geophys. PAGEOPH*, *113*(1), 765–785, doi:10.1007/BF01592958.

Miller, L. J., and F. S. M. (1998), *CEDRIC Custom Editing and Display of Reduced Information in Cartesian space*.

Miltenberger, A. K., P. R. Field, A. A. Hill, P. Rosenberg, B. J. Shipway, J. M. Wilkinson, R. Scovell, and A. M. Blyth (2018), Aerosol-cloud interactions in mixed-phase convective clouds - Part 1: Aerosol perturbations, *Atmos. Chem. Phys.*, *18*(5), 3119–3145, doi:10.5194/acp-18-3119-2018.

Morrison, H., J. A. Curry, and V. I. Khvorostyanov (2005), A New Double-Moment Microphysics Parameterization for Application in Cloud and Climate Models. Part I: Description, *J. Atmos. Sci.*, *62*(6), 1665–1677, doi:10.1175/JAS3446.1.

Morrison, H., and W. W. Grabowski (2011), Cloud-system resolving model simulations of aerosol indirect effects on tropical deep convection and its thermodynamic environment, *Atmos. Chem. Phys.*, *11*(20), 10503–10523, doi:10.5194/acp-11-10503-2011.

Morrison, H., and W. W. Grabowski (2007), Comparison of Bulk and Bin Warm-Rain Microphysics Models Using a Kinematic Framework, *J. Atmos. Sci.*, *64*(8), 2839–2861, doi:10.1175/JAS3980.

Morrison, H., and W. W. Grabowski (2008), Modeling supersaturation and subgrid-scale mixing with two-moment bulk warm microphysics, *J. Atmos. Sci.*, *65*(3), 792–812, doi:10.1175/2007JAS2374.1.

Morrison, H., and J. A. Milbrandt (2015), Parameterization of cloud microphysics based on the prediction of bulk ice particle properties. Part I: Scheme description and idealized tests, *J. Atmos. Sci.*, *72*(1), 287–311, doi:10.1175/JAS-D-14-0065.1.

Mullendore, G. L., D. R. Durran, and J. R. Holton (2005), Cross-tropopause tracer transport in midlatitude convection, *J. Geophys. Res. Atmos.*, *110*(D6), n/a-n/a, doi:10.1029/2004JD005059.

Musil, D. J., W. R. Sand, and R. A. Schleusener (1973), Analysis of Data from T-28 Aircraft Penetrations of a Colorado Hailstorm, *J. Appl. Meteorol.*, *12*(8), 1364–1370, doi:10.1175/1520-0450(1973)012<1364:aodfta>2.0.co;2.

Musil, D. J., A. J. Heymsfield, and P. L. Smith (1986), Microphysical Characteristics of a Well-Developed Weak Echo Region in a High Plains Supercell Thunderstorm, *J. Clim. Appl. Meteorol.*, *25*, 1037–1051, doi:10.1175/1520-0450(1986)025<1037:MCOAWD>2.0.CO;2.

Nagel, H. A., R. C. Beardsley, J. R. Holton, and R. E. Orville (n.d.), *TECHNICAL EDITOR*.

National Centers for Environmental Information (NCEI) (2016), NCDC Storm Events Database (Storm Data), 43-44, 839-840 pp. https://www.ncdc.noaa.gov/stormevents/.

National Centers for Environmental Information (NCEI) (2017), NCDC Storm Events Database (Storm Data), 39-40 pp. https://www.ncdc.noaa.gov/stormevents/.

Nelson, S. P. (1983), The influence of storm flow structure on hail growth., *J. Atmos. Sci.*, *40*(8), 1965–1983, doi:10.1175/1520-0469(1983)040<1965:TIOSFS>2.0.CO;2.

Nelson, S. P., and R. A. Brown (1987), Error Sources and Accuracy of Vertical Velocities Computed from Multiple-Doppler Radar Measurements in Deep Convective Storms, *J. Atmos. Ocean. Technol.*, *4*(1), 233–238, doi:10.1175/1520-0426(1987)004<0233:ESAAOV>2.0.CO;2.

Ng, N. L. et al. (2011), An Aerosol Chemical Speciation Monitor (ACSM) for routine monitoring of the composition and mass concentrations of ambient aerosol, *Aerosol Sci. Technol.*, *45*(7), 770–784, doi:10.1080/02786826.2011.560211.

Nieminen, T. et al. (2018), Global analysis of continental boundary layer new particle formation based on long-term measurements, *Atmos. Chem. Phys.*, *18*(19), 14737–14756, doi:10.5194/acp-18-14737-2018.

Nilsson, E. D., J. Paatero, and M. Boy (2001), Effects of air masses and synoptic weather on aerosol formation in the continental boundary layer, *Tellus, Ser. B Chem. Phys. Meteorol.*, *53*(4), 462–478, doi:10.3402/tellusb.v53i4.16619.

Noll, K. E., and M. J. Pilat (1971), Size distribution of atmospheric giant particles, *Atmos. Environ.*, *5*(7), 527–540, doi:10.1016/0004-6981(71)90063-1.

North, K. W., M. Oue, P. Kollias, S. E. Giangrande, S. M. Collis, and C. K. Potvin (2017), Vertical air motion retrievals in deep convective clouds using the ARM scanning radar network in Oklahoma during MC3E, *Atmos. Meas. Tech.*, *10*(8), 2785–2806, doi:10.5194/amt-10-2785-2017.

Nowlan, C. R. et al. (2016), Nitrogen dioxide observations from the Geostationary Trace gas and Aerosol Sensor Optimization (GeoTASO) airborne instrument: Retrieval algorithm and measurements during DISCOVER-AQ Texas 2013, *Atmos. Meas. Tech.*, *9*(6), 2647–2668, doi:10.5194/amt-9-2647-2016.

O'Dowd, C. et al. (1999), On the photochemical production of new particles in the coastal boundary layer, *Geophys. Res. Lett.*, *26*(12), 1707–1710, doi:10.1029/1999GL900335.

Ooyama, K. V. (2002): The cubic-spline transform method: Basic definitions and tests in a 1D single domain. Mon. Weather Rev., 130, 2392–2415, doi:10.1175/1520-0493(2002)130<2392:TCSTMB>2.0.CO;2.

Oue, M., P. Kollias, A. Shapiro, A. Tatarevic, and T. Matsui (2019), Investigation of observational error sources in multi-Doppler-radar three-dimensional variational vertical air motion retrievals, *Atmos. Meas. Tech.*, *12*(3), 1999–2018, doi:10.5194/amt-12-1999-2019.

Palmer, A. D. F. (1912), The Theory of Measurements. McGraw-Hill Book Company, New York, 739 95-104 pp.

Parworth, C., J. Fast, F. Mei, T. Shippert, C. Sivaraman, A. Tilp, T. Watson, and Q. Zhang (2015), Long-term measurements of submicrometer aerosol chemistry at the Southern Great Plains (SGP) using an Aerosol Chemical Speciation Monitor (ACSM), *Atmos. Environ.*, *106*, 43–55, doi:10.1016/j.atmosenv.2015.01.060.

Peppler, R. A. et al. (2000), ARM Southern Great Plains Site Observations of the Smoke Pall Associated with the 1998 Central American Fires, *Bull. Am. Meteorol. Soc.*, *81*(11), 2563–2591, doi:10.1175/1520-0477(2000)081<2563:ASGPSO>2.3.CO;2.

Peters, J. M., C. J. Nowotarski, and H. Morrison (2019), The Role of Vertical Wind Shear in Modulating Maximum Supercell Updraft Velocities, *J. Atmos. Sci.*, *76*(10), 3169–3189, doi:10.1175/jas-d-19-0096.1.

Petters, M. D., and S. M. Kreidenweis (2007), A single parameter representation of hygroscopic growth and cloud condensation nucleus activity, *Atmos. Chem. Phys.*, *7*(8), 1961–1971, doi:10.5194/acp-7-1961-2007.

Phillips, V. T. J., P. J. DeMott, and C. Andronache (2008), An empirical parameterization of heterogeneous ice nucleation for multiple chemical species of aerosol, *J. Atmos. Sci.*, *65*(9), 2757–2783, doi:10.1175/2007JAS2546.1.

Potvin, C. K., D. Betten, L. J. Wicker, K. L. Elmore, and M. I. Biggerstaff (2012), 3DVAR versus Traditional Dual-Doppler Wind Retrievals of a Simulated Supercell Thunderstorm, *Mon. Weather Rev.*, *140*(11), 3487–3494, doi:10.1175/MWR-D-12-00063.1.

Power, H. C., S. C. Sheridan, and J. C. Senkbeil (2006), Synoptic climatological influences on the spatial and temporal variability of aerosols over North America, *Int. J. Climatol.*, *26*(6), 723–741, doi:10.1002/joc.1277.

Purser, R. J., W. S. Wu, D. F. Parrish, and N. M. Roberts (2003): Numerical aspects of the application of recursive filters to variational statistical analysis. Part I: Spatially homogeneous and isotropic Gaussian covariances. *Mon. Weather Rev.*, 131, 1524–1535, doi:10.1175//1520-0493(2003)131<1524:NAOTAO>2.0.CO;2.

Qiu, Y., C. Zhao, J. Guo, and J. Li (2017), 8-Year ground-based observational analysis about the seasonal variation of the aerosol-cloud droplet effective radius relationship at SGP site, *Atmos. Environ.*, *164*, 139–146, doi:10.1016/j.atmosenv.2017.06.002.

Rasmussen, R. M., I. Geresdi, G. Thompson, K. Manning, and E. Karplus (2002), Freezing drizzle formation in stably stratified layer clouds: The role of radiative cooling of cloud droplets, cloud condensation nuclei, and ice initiation, *J. Atmos. Sci.*, *59*(4), 837–860, doi:10.1175/1520-0469(2002)059<0837:FDFISS>2.0.CO;2.

Ray, P. S., C. L. Ziegler, W. Bumgarner, and R. J. Serafin (1980), Single- and Multiple-Doppler Radar Observations of Tornadic Storms, *Mon. Weather Rev.*, *108*(10), 1607–1625, doi:10.1175/1520-0493(1980)108<1607:SAMDRO>2.0.CO;2.

Reutter, P., H. Su, J. Trentmann, M. Simmel, D. Rose, S. S. Gunthe, H. Wernli, M. O. Andreae, and U. Pöschl (2009), Aerosol- and updraft-limited regimes of cloud droplet formation: influence of particle number, size and hygroscopicity on the activation of cloud condensation nuclei (CCN), *Atmos. Chem. Phys.*, *9*(18), 7067–7080, doi:10.5194/acp-9-7067-2009.

Ryzhkov, A. V., M. R. Kumjian, S. M. Ganson, and P. Zhang (2013), Polarimetric radar characteristics of melting hail. part II: Practical implications. *J. Appl. Meteorol. Climatol.*, 52, 2871–2886, doi:10.1175/JAMC-D-13-074.1.

Rissman, T. A., T. M. VanReken, J. Wang, R. Gasparini, D. R. Collins, H. H. Jonsson, F. J. Brechtel, R. C. Flagan, and J. H. Seinfeld (2006), Characterization of ambient aerosol from measurements of cloud condensation nuclei during the 2003 Atmospheric Radiation Measurement Aerosol Intensive Observational Period at the Southern Great Plains site in Oklahoma, *J. Geophys. Res.*, *111*(D5), D05S11, doi:10.1029/2004JD005695.

Ritter, B., and J.-F. Geleyn (1992), A Comprehensive Radiation Scheme for Numerical Weather Prediction Models with Potential Applications in Climate Simulations, *Mon. Weather Rev.*, 120(2), 303–325, doi:10.1175/1520-0493(1992)120<0303:ACRSFN>2.0.CO;2.

Rogers, C. M., and K. P. Bowman (2001), Transport of smoke from the Central American fires of 1998, *J. Geophys. Res. Atmos.*, *106*(D22), 28357–28368, doi:10.1029/2000JD000187.

Rosenfeld, D., U. Lohmann, G. B. Raga, C. D. O'Dowd, M. Kulmala, S. Fuzzi, A. Reissell, and M. O. Andreae (2008), Flood or drought: how do aerosols affect precipitation?, *Science*, *321*(5894), 1309–13, doi:10.1126/science.1160606.

Rosenfeld, D., E. Williams, M. O. Andreae, E. Freud, U. Pöschl, and N. O. Rennó (2012), The scientific basis for a satellite mission to retrieve CCN concentrations and their impacts on convective clouds, *Atmos. Meas. Tech.*, *5*(8), 2039–2055, doi:10.5194/amt-5-2039-2012.

Rosenfeld, D. et al. (2014), Global observations of aerosol-cloud-precipitation-climate interactions, *Rev. Geophys.*, *52*(4), 750–808, doi:10.1002/2013RG000441.

Saide, P. E., G. Thompson, T. Eidhammer, A. M. da Silva, R. B. Pierce, and G. R. Carmichael (2016), Assessment of biomass burning smoke influence on environmental conditions for

multiyear tornado outbreaks by combining aerosol-aware microphysics and fire emission constraints, *J. Geophys. Res. Atmos.*, *121*(17), 10,294-10,311, doi:10.1002/2016JD025056.

Saleeby, S. M., S. C. van den Heever, P. J. Marinescu, S. M. Kreidenweis, and P. J. DeMott (2016), Aerosol effects on the anvil characteristics of mesoscale convective systems, *J. Geophys. Res. Atmos.*, *121*(18), 10,880-10,901, doi:10.1002/2016JD025082.

Saleeby, S. M., and W. R. Cotton (2004), A Large-Droplet Mode and Prognostic Number Concentration of Cloud Droplets in the Colorado State University Regional Atmospheric Modeling System (RAMS). Part I: Module Descriptions and Supercell Test Simulations, *J. Appl. Meteorol.*, *43*(1), 182–195, doi:10.1175/1520-0450(2004)043<0182:almapn>2.0.co;2.

Saleeby, S. M., and S. C. van den Heever (2013), Developments in the CSU-RAMS Aerosol Model: Emissions, Nucleation, Regeneration, Deposition, and Radiation, *J. Appl. Meteorol. Climatol.*, *52*(12), 2601–2622, doi:10.1175/JAMC-D-12-0312.1.

Schättler, U., Doms, G., and Schraff, C. (2016): A description of the nonhydrostatic regional COSMO-model, Part VII: User's Guide, Available online at http://www.cosmo-model.org/, [Accessed on 24 July 2019], 227 pp.

Schmale, J. et al. (2018), Long-term cloud condensation nuclei number concentration, particle number size distribution and chemical composition measurements at regionally representative observatories, *Atmos. Chem. Phys*, *185194*(August 2017), 2853–2881, doi:10.5194/acp-18-2853-2018.

Seifert, A., and K. D. Beheng (2006a), A two-moment cloud microphysics parameterization for mixed-phase clouds. Part 1: Model description, *Meteorol. Atmos. Phys.*, *92*(1–2), 45–66, doi:10.1007/s00703-005-0112-4.

Seifert, A., and K. D. Beheng (2006b), A two-moment cloud microphysics parameterization for mixed-phase clouds. Part 2: Maritime vs. continental deep convective storms, *Meteorol. Atmos. Phys.*, *92*(1–2), 67–82, doi:10.1007/s00703-005-0113-3.

Seifert, A., C. Köhler, and K. D. Beheng (2012), Aerosol-cloud-precipitation effects over Germany as simulated by a convective-scale numerical weather prediction model, *Atmos. Chem. Phys.*, *12*(2), 709–725, doi:10.5194/acp-12-709-2012.

Seifert, A., A. Khain, A. Pokrovsky, and K. D. Beheng (2006), A comparison of spectral bin and two-moment bulk mixed-phase cloud microphysics, *Atmos. Res.*, *80*(1), 46–66, doi:10.1016/j.atmosres.2005.06.009.

Seifert, A., C. Köhler, and K. D. Beheng (2012), Aerosol-cloud-precipitation effects over Germany as simulated by a convective-scale numerical weather prediction model, Atmos. Chem. Phys., 12(2), 709–725, doi:10.5194/acp-12-709-2012.

Seiki, T., and T. Nakajima (2014), Aerosol effects of the condensation process on a convective cloud simulation, *J. Atmos. Sci.*, *71*(2), 833–853, doi:10.1175/JAS-D-12-0195.1.

Sheffield, A. M., S. M. Saleeby, and S. C. Van den Heever (2015), Aerosol-induced mechanisms for cumulus congestus growth, *J. Geophys. Res.*, *120*(17), 8941–8952, doi:10.1002/2015JD023743.

Sheridan, P. J., D. J. Delene, and J. A. Ogren (2001), Four years of continuous surface aerosol measurements from the Department of Energy's Atmospheric Radiation Measurement Program Southern Great Plains Cloud and Radiation Testbed site, *J. Geophys. Res. Atmos.*, *106*(D18), 20735–20747, doi:10.1029/2001JD000785.

Sherman, J. P., P. J. Sheridan, J. A. Ogren, E. Andrews, D. Hageman, L. Schmeisser, A. Jefferson, and S. Sharma (2015), A multi-year study of lower tropospheric aerosol variability and systematic relationships from four North American regions, *Atmos. Chem. Phys.*, *15*(21), 12487–12517, doi:10.5194/acp-15-12487-2015.

Shipway, B. J., and A. A. Hill (2012), Diagnosis of systematic differences between multiple parametrizations of warm rain microphysics using a kinematic framework, *Q. J. R. Meteorol. Soc.*, *138*(669), 2196–2211, doi:10.1002/qj.1913.

Shipway, B. J. (2015), Revisiting Twomey's approximation for peak supersaturation, *Atmos. Chem. Phys.*, *15*(7), 3803–3814, doi:10.5194/acp-15-3803-2015.

Shpund, J., A. Khain, B. Lynn, J. Fan, B. Han, A. Ryzhkov, J. Snyder, J. Dudhia, and D. Gill (2019), Simulating a Mesoscale Convective System Using WRF with a New Spectral Bin Microphysics - Part 1: Hail vs Graupel, *J. Geophys. Res. Atmos.*, 1–30, doi:10.1029/2019JD030576.

Sisterson, D. L., R. A. Peppler, T. S. Cress, P. J. Lamb, and D. D. Turner (2016), The ARM Southern Great Plains (SGP) Site, *Meteorol. Monogr.*, *57*, 6.1-6.14, doi:10.1175/AMSMONOGRAPHS-D-16-0004.1.

Skamarock, W. C., J. B. Klemp, J. Dudhi, D. O. Gill, D. M. Barker, M. G. Duda, X.-Y. Huang, W. Wang, and J. G. Powers (2008), A Description of the Advanced Research WRF Version 3, *Tech. Rep.*, (June), 113, doi:10.5065/D6DZ069T.

Smagorinsky, J. (1963), GENERAL CIRCULATION EXPERIMENTS WITH THE PRIMITIVE EQUATIONS, *Mon. Weather Rev.*, *91*(3), 99–164, doi:10.1175/1520-0493(1963)091<0099:GCEWTP>2.3.CO;2.

Smith, J. N. and McMurry, P. H. (2015): New Particle Formation Study Final Campaign Report. Ed. by Robert Stafford, DOE ARM Climate Research Facility, DOE/SC-ARM-15-011.

Söder, J., M. Gerding, A. Schneider, A. Dörnbrack, H. Wilms, J. Wagner, and F. J. Lübken (2019), Evaluation of wake influence on high-resolution balloon-sonde measurements, *Atmos. Meas. Tech.*, *12*(8), 4191–4210, doi:10.5194/amt-12-4191-2019.

Son, K., J. Choi, W. P. Jeon, and H. Choi (2010), Effect of free-stream turbulence on the flow over a sphere, *Phys. Fluids*, *22*(4), 1–7, doi:10.1063/1.3371804.

Stevens, R. G. et al. (2018), A model intercomparison of CCN-limited tenuous clouds in the high Arctic, *Atmos. Chem. Phys.*, *18*(15), 11041–11071, doi:10.5194/acp-18-11041-2018.

Stratton, R., Willet, M., Derbyshire, S., Wong, R., and Whitall, M. (2015), Convection schemes, Unified Model documentation paper 027, Met Office.

Storer, R. L., S. C. van den Heever, and G. L. Stephens (2010), Modeling Aerosol Impacts on Convective Storms in Different Environments, *J. Atmos. Sci.*, *67*(12), 3904–3915, doi:10.1175/2010JAS3363.1.

Storer, R. L., and S. C. van den Heever (2012), Microphysical Processes Evident in Aerosol Forcing of Tropical Deep Convective Clouds, *J. Atmos. Sci.*, 120920104307002, doi:10.1175/JAS-D-12-076.1.

Tao, W.-K., X. Li, A. Khain, T. Matsui, S. Lang, and J. Simpson (2007), Role of atmospheric aerosol concentration on deep convective precipitation: Cloud-resolving model simulations, *J. Geophys. Res.*, *112*(D24), D24S18, doi:10.1029/2007JD008728.

Tao, W., J. Chen, Z. Li, C. Wang, and C. Zhang (2012), Impact of aerosols on convective clouds and precipitation, *Rev. Geophys.*, *50*(2), RG2001, doi:10.1029/2011RG000369.

Tao, W., and X. Li (2016), The relationship between latent heating, vertical velocity, and precipitation processes: The impact of aerosols on precipitation in organized deep convective systems, *J. Geophys. Res. Atmos.*, *121*(11), 6299–6320, doi:10.1002/2015JD024267.

Tessendorf, S. A., L. J. Miller, K. C. Wiens, and S. A. Rutledge (2005), The 29 June 2000 Supercell Observed during STEPS. Part I: Kinematics and Microphysics, *J. Atmos. Sci.*, *62*(12), 4127–4150, doi:10.1175/JAS3585.1.

Thompson, R. L., R. Edwards, J. A. Hart, K. L. Elmore, and P. Markowski (2003), Close proximity soundings within supercell environments obtained from the rapid update cycle, *Weather Forecast.*, *18*(6), 1243–1261, doi:10.1175/1520-0434(2003)018<1243:CPSWSE>2.0.CO;2.

Twomey, S., and P. Squires (1959), The Influence of Cloud Nucleus Population on the Microstructure and Stability of Convective Clouds, Tellus, 11(4), 408–411, doi:10.3402/tellusa.v11i4.9331.

Twomey, S. (1974), Pollution and the planetary albedo, *Atmos. Environ.*, *8*(12), 1251–1256, doi:10.1016/0004-6981(74)90004-3.

Twomey, S. (1977), The Influence of Pollution on the Shortwave Albedo of Clouds, *J. Atmos. Sci.*, *34*(7), 1149–1152, doi:10.1175/1520-0469(1977)034<1149:TIOPOT>2.0.CO;2.

USDA-NASS Oklahoma Field Office (2012), *Oklahoma Agricultural Statistics 2012*, Oklahoma City, OK.

Vali, G. (1996), Ice Nucleation — a review, in *Nucleation and Atmospheric Aerosols 1996*, pp. 271–279, Elsevier.

van den Heever, S. C., G. G. Carrió, W. R. Cotton, P. J. DeMott, and A. J. Prenni (2006), Impacts of Nucleating Aerosol on Florida Storms. Part I: Mesoscale Simulations, *J. Atmos. Sci.*, *63*(7), 1752–1775, doi:10.1175/JAS3713.1.

van den Heever, S. C., and W. R. Cotton (2007), Urban aerosol impacts on downwind convective storms, *J. Appl. Meteorol. Climatol.*, *46*(6), 828–850, doi:10.1175/JAM2492.1.

van den Heever, S. C., G. L. Stephens, and N. B. Wood (2011), Aerosol Indirect Effects on Tropical Convection Characteristics under Conditions of Radiative–Convective Equilibrium, *J. Atmos. Sci.*, *68*(4), 699–718, doi:10.1175/2010JAS3603.1.

van den Heever, S.C., and coauthors (2018): (ACPC) Initiative: Deep Convective Cloud Group Roadmap Updated: October 2017. http://acpcinitiative.org/Docs/ACPC_DCC_Roadmap_171019.pdf

van den Heever, S. C., L. D. Grant, S. W. Freeman, and P. J. Marinescu (2020), Diving into Cold Pools and Flying into Updrafts of Deep Convective Storms, in review at *Bull. Am. Meteor. Soc.*

Varble, A., E. J. Zipser, A. M. Fridlind, P. Zhu, A. S. Ackerman, J. Chaboureau, S. Collis, J. Fan, A. Hill, and B. Shipway (2014), Evaluation of cloud-resolving and limited area model intercomparison simulations using TWP-ICE observations: 1. Deep convective updraft properties, *J. Geophys. Res. Atmos.*, *119*(24), 13,891-13,918, doi:10.1002/2013JD021371.

Varble, A. (2018), Erroneous attribution of deep convective invigoration to aerosol concentration, *J. Atmos. Sci.*, *75*(4), 1351–1368, doi:10.1175/JAS-D-17-0217.1.

Vie, B., J. P. Pinty, S. Berthet, and M. Leriche (2016), LIMA (v1.0): A quasi two-moment microphysical scheme driven by a multimodal population of cloud condensation and ice freezing nuclei, *Geosci. Model Dev.*, *9*(2), 567–586, doi:10.5194/gmd-9-567-2016.

Vogel, B., H. Vogel, D. Ḧaumer, M. Bangert, K. Lundgren, R. Rinke, and T. Stanelle (2009), The comprehensive model system COSMO-ART Radiative impact of aerosol on the state of

the atmosphere on the regional scale, *Atmos. Chem. Phys.*, *9*(22), 8661–8680, doi:10.5194/acp-9-8661-2009.

Walko, R. L. et al. (2000), Coupled Atmosphere–Biophysics–Hydrology Models for Environmental Modeling, *J. Appl. Meteorol.*, *39*(6), 931–944, doi:10.1175/1520-0450(2000)039<0931:CABHMF>2.0.CO;2.

Walters, D. et al. (2017), The Met Office Unified Model Global Atmosphere 6.0/6.1 and JULES Global Land 6.0/6.1 configurations, *Geosci. Model Dev.*, *10*(4), 1487–1520, doi:10.5194/gmd-10-1487-2017.

Wang, C. (2005), A modeling study of the response of tropical deep convection to the increase of cloud condensation nuclei concentration: 1. Dynamics and microphysics, *J. Geophys. Res. Atmos.*, *110*(21), 1–16, doi:10.1029/2004JD005720.

Wang, J., S. C. Van Den Heever, and J. S. Reid (2009), A conceptual model for the link between Central American biomass burning aerosols and severe weather over the south central United States, *Environ. Res. Lett.*, *4*(1), doi:10.1088/1748-9326/4/1/015003.

Wang, J., J. Bian, W. O. Brown, H. Cole, V. Grubišić, and K. Young (2009), Vertical air motion from T-REX radiosonde and dropsonde data, *J. Atmos. Ocean. Technol.*, *26*(5), 928–942, doi:10.1175/2008JTECHA1240.1.

Waugh, S., and T. J. Schuur (2018), On the use of radiosondes in freezing precipitation, *J. Atmos. Ocean. Technol.*, *35*(3), 459–472, doi:10.1175/JTECH-D-17-0074.1.

Weingartner, E., S. Nyeki, and U. Baltensperger (1999), Seasonal and diurnal variation of aerosol size distributions (10 < D < 750 nm) at a high-alpine site (Jungfraujoch 3580 m asl), *J. Geophys. Res.*, *104*, 809–826, doi:10.1029/1999jd900170.

Weisman, M. L., and J. B. Klemp (1984), The structure and classification of numerically simulated convective storms in directionally varying wind shears., *Mon. Weather Rev.*, *112*(12), 2479–2498, doi:10.1175/1520-0493(1984)112<2479:TSACON>2.0.CO;2.

Welch, P. (1967), The use of fast Fourier transform for the estimation of power spectra: A method based on time averaging over short, modified periodograms, *IEEE Trans. Audio Electroacoust.*, *15*(2), 70–73, doi:10.1109/TAU.1967.1161901.

Yu, F. et al. (2015), Spring and summer contrast in new particle formation over nine forest areas in North America, , 13993–14003, doi:10.5194/acp-15-13993-2015.

APPENDIX 1: MERGED AEROSOL SIZE DISTRIBUTIONS

Five years (2009-2013) of data from three aerosol instruments at the ARM-SGP site were merged in order to create the aerosol size distribution dataset used in this study. One dataset was the aerosol size distribution data from the scanning mobility particle sizer (SMPS), part of the TDMA system, which were combined with size distribution data from the aerodynamic particle sizer (APS). The merged size distribution from those two instruments spanned the diameter (mobility) size range between ~12 nm and ~14 μm with 215 bins (Collins, 2010; ARM Climate Research Facility, 2010, 2015). The other dataset contained total aerosol number concentrations from a TSI 3010 condensation particle counter (CPC; ARM Climate Research Facility, 2007, 2011). Therefore, total aerosol number concentrations can be obtained from both the integrated SMPS+APS size distributions and the CPC measurements. Because there were very few particles larger than the upper limit of the SMPS+APS measurements and the CPC measured smaller particles than the SMPS+APS, concurrent CPC data were used to extend the SMPS+APS size distributions from ~12 nm down to 7 nm and to improve the representation of the aerosol size distribution at the smallest sizes, where the largest SMPS observation uncertainties exist. The details of the processing of these data are described here.

First, the CPC data were quality controlled. Data that were flagged by the ARM quality control as suspect or incorrect due to faulty instrumentation or operation were removed. Also, CPC data that were consistently lower than the concentrations from a collocated cloud condensation nuclei counter (single column, DMT Model 1) at the highest supersaturation available (typically ~1%) and CPC data with unrealistically small (< 200 cm^{-3}) or unrealistically large (> 100,000 cm^{-3}) aerosol number concentrations were removed. The quality-controlled

CPC data were then time-interpolated to the midpoint time of each SMPS+APS measurement period (~45 min). Then, the SMPS+APS data were quality controlled. Here, it is important to note that estimated corrections were made to the SMPS size distributions to account for potential particle losses due to diffusion in the inlet and system tubing. Corrections were not made to the APS size distribution data for possible particle losses within the inlet and system tubing, but it is expected that these losses are likely small for most of the APS size distribution. For example, experiments have shown approximately unit transmission efficiencies for particles with diameters up to 4 μm for the SGP inlet system. For larger sizes where low particle counts make it difficult to characterize transmission efficiencies experimentally, modeled transmission efficiencies predict significantly increasing biases for particles with diameters greater than ~10 μm (Bullard et al. 2017). During the quality-control process, suspect or incomplete SMPS+APS data were removed. Suspect or incomplete SMPS+APS data included instances when 1) the CPC data were unavailable or incorrect during a given SMPS+APS measurement period, 2) the integrated number concentration from the SMPS+APS was unrealistic, as noted above, 3) large portions of the SMPS+APS size distribution were missing, which occurred sporadically due to shifts in the instrument voltage, 4) there were unrealistic peaks in the size distribution, particularly at large particle sizes, and 5) there were peaks in integrated number concentrations in the first measurement after the daily calibration, which were likely due to contamination from residual particles from the atomized calibration aerosol. These checks resulted in the removal of ~25% of the SMPS+APS distributions, with the majority of data removal due to not having simultaneous CPC and SMPS+APS measurements. Despite this reduction in data quantity, over 31,700 size distributions remained, which equate to ~3 years of data during the 2009-2013 time period.

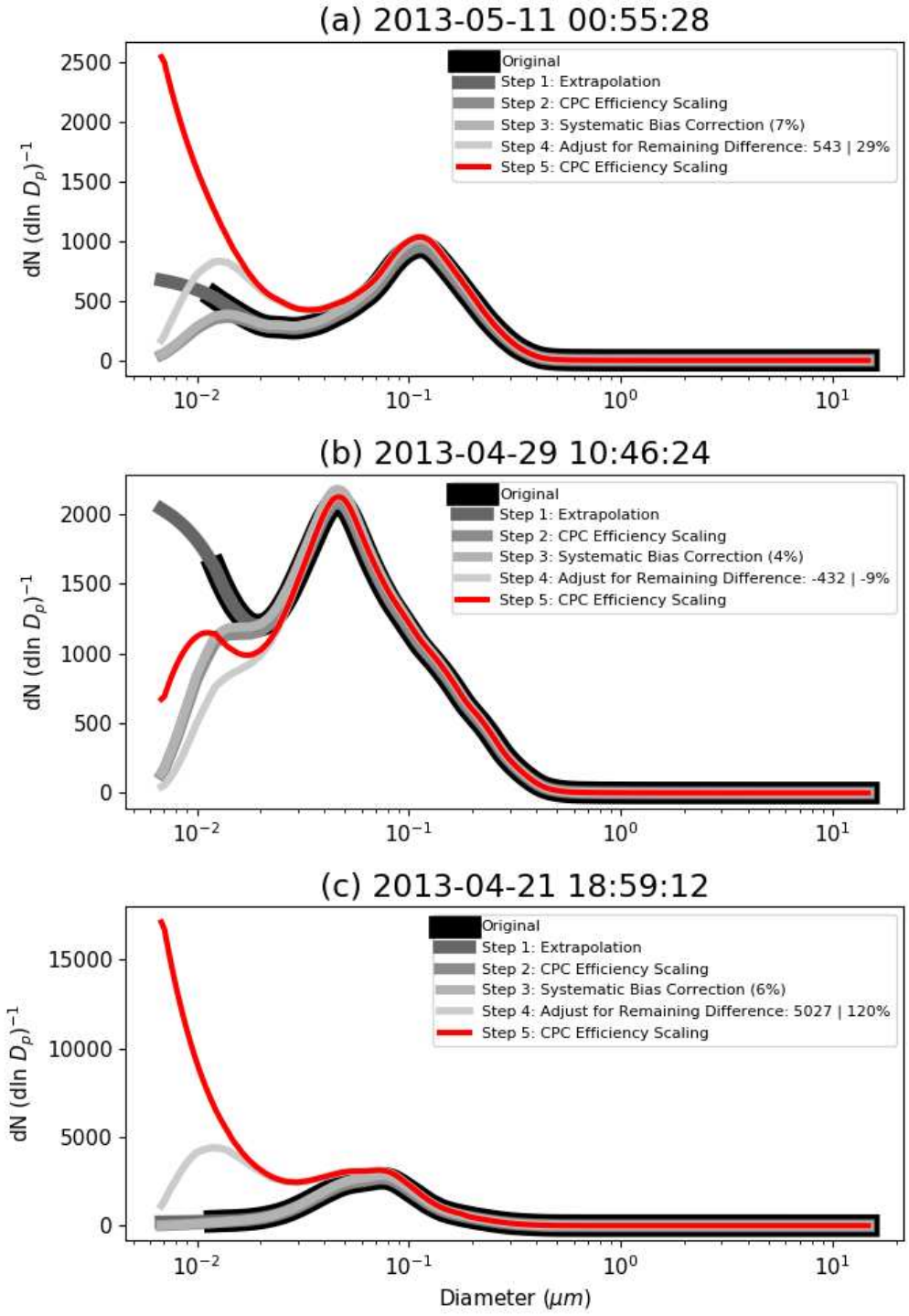

Figure A1.1. Three examples of the adjustments made to the original TDMA aerosol number size distributions and the final aerosol number size distribution post-adjustments (red).

In order to synthesize the quality-controlled CPC and SMPS+APS measurements into one merged dataset, five steps were taken (Figure A1.1). First, the SMPS+APS size distributions

were extrapolated from their smallest size bin (usually ~12 nm) down to 7 nm, the approximate smallest size for which the CPC observes a significant fraction of aerosol particles (~10%; Mertes et al. 1995). The five smallest available size bins in the SMPS+APS size distribution were fit with a polynomial of the functional form:

$$dN(D_p) = aD_p^2 + b, \quad \text{(A1.1)}$$

where a and b are coefficients and D_p is the particle size bin diameter in μm. The coefficients, a and b, were determined via least-squares regression for each SMPS+APS size distribution, and the resulting polynomial was used to extrapolate the size distribution down to 7 nm (Figure A1.1, Step 1). Several functional forms were tested for this extrapolation, and the form in Eq. A1.1 produced the best results. Since the CPC only detected a fraction of the particles less than 28 nm, we also applied the CPC detection efficiencies from Mertes et al. (1995) to scale down the extrapolated size distributions (Step 2 in Figure A1.1) in order to represent the size-resolved distribution that the CPC would observe. Therefore, the integrated number concentration from the resulting SMPS+APS size distribution represents an estimate of the same quantity reported by the CPC. The integrated number concentrations from the SMPS+APS size distributions after Step 2 were compared to the CPC total number concentrations. Since these two instruments were generally unmonitored during their deployments, a number of unreported issues (e.g., clogging or a leak in the air flow) may have caused the derived concentration measurements from either one of the instruments to drift for some extended periods of time. Therefore, in Step 3, the 2-week rolling median percentage difference between the two instruments was calculated for the entire time series and used to correct for any systematic drifts between the two instruments. This 2-week rolling median calculation excluded times between 1800 and 2400 UTC, when we would potentially expect large differences between the instruments due to new particle formation events

and growth. Because of the higher uncertainties associated with the SMPS+APS total integrated number concentrations, the SMPS+APS size distribution was always scaled up or down to the CPC concentrations. This scaling factor was typically within 50% (median value of 7.3% for the entire dataset), except for two periods (January-February 2009 and September-December 2013) when the median percentage differences were consistently greater than 50%.

After correcting for this systematic bias (Step 3), the remaining difference between the CPC and SMPS+APS total number concentrations was used to adjust the SMPS+APS number size distribution, such that the integrated number concentration from the SMPS+APS size distribution equaled the CPC value. This difference in the total number concentration was applied to the SMPS+APS size distribution using an exponential function, only for sizes below the diameter associated with the 95th percentile of the cumulative integrated number concentration (median value of ~200 nm), and taking into account the CPC detection efficiencies (**Error! Reference source not found.**). An exponential function was chosen because there were much larger uncertainties in the observed number concentrations and diameters of the smallest

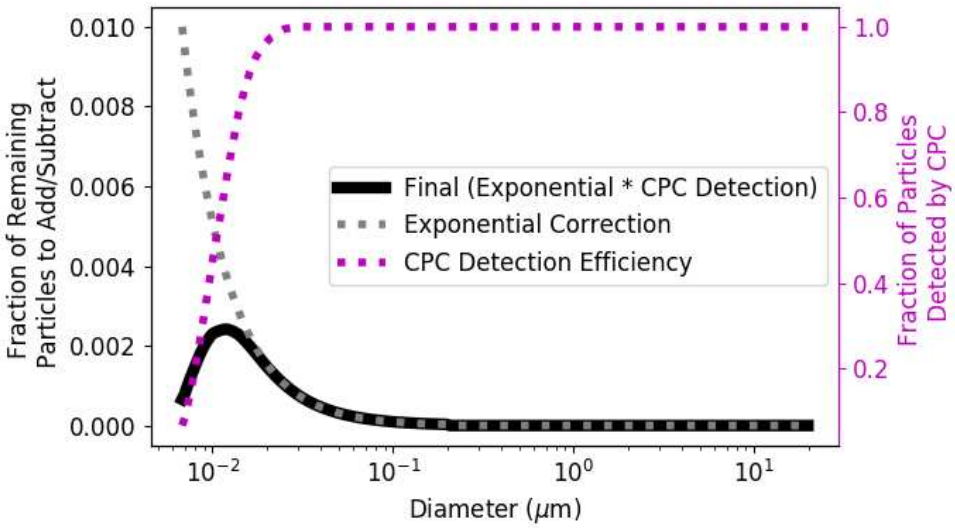

Figure A1.2. Fraction of particles to either add or remove from the size distribution during Step 4 of the adjustments (black), which was based on the multiplication of an exponential function (cyan) and CPC detection efficiencies (magenta, right axis).

particles in the size distribution and therefore, the need to correct particle counts was most likely associated with errors in the data for the smallest particle sizes. These uncertainties were associated with the possible loss of small particles within the inlet, sampling lines, and/or instrument due to evaporation or deposition to walls, the extrapolation of the SMPS+APS size distribution, uncertainties associated with the charging probabilities of the smaller particles in the SMPS+APS system, and small errors in the high voltage supplied in the SMPS, which can lead to substantial uncertainties in the sizing of the smallest particles observed. The aerosol size distribution above ~200 nm was not changed in this step. The final correction function (**Error! Reference source not found.**, black line) was applied in an iterative manner, nudging the size distribution up or down in order to match the integrated number from the SMPS+APS size distributions to the CPC total number concentration (Step 4). The resulting aerosol size distributions after Step 4 were scaled back up by the reciprocal of the CPC detection efficiencies (Step 5) to represent an estimate of the true aerosol particle size distribution and number concentration at each time.

To validate the adjustment algorithm described above, the original and adjusted size distributions were compared to data from the New Particle Formation Study (NPFS) (Smith and McMurray, 2015; NPFS, 2017). NPFS took place at the SGP site for ~6 weeks in April-May 2013, and during this study, measurements of aerosol particle size distributions were measured down to ~3 nm in the SGP Guest Facility, a few hundred meters away from the CPC and SMPS+APS measurements. We compared the integrated number concentrations for aerosol with diameters between 7 and 30 nm from the NPFS to the adjusted SMPS+APS size distributions during this period, since the majority of changes to the SMPS+APS size distributions occurred in this size range (e.g., Figure A1.2). By incorporating the CPC data via the steps described above, the

adjusted SMPS+APS distributions better captured the timing and magnitude of aerosol concentrations at these small particle sizes (Figure A1.3). The correlation coefficient for this comparison improved from 0.37 to 0.89 from the original data to the adjusted data. The SMPS+APS size distribution data above 30 nm remained relatively unchanged, since the majority of the adjustments were applied below 30 nm. This improvement of the SMPS+APS aerosol number size distribution data demonstrates the utility of having a suite of related aerosol instruments at the same site that can be compared and combined to provide a more comprehensive representation of aerosol characteristics

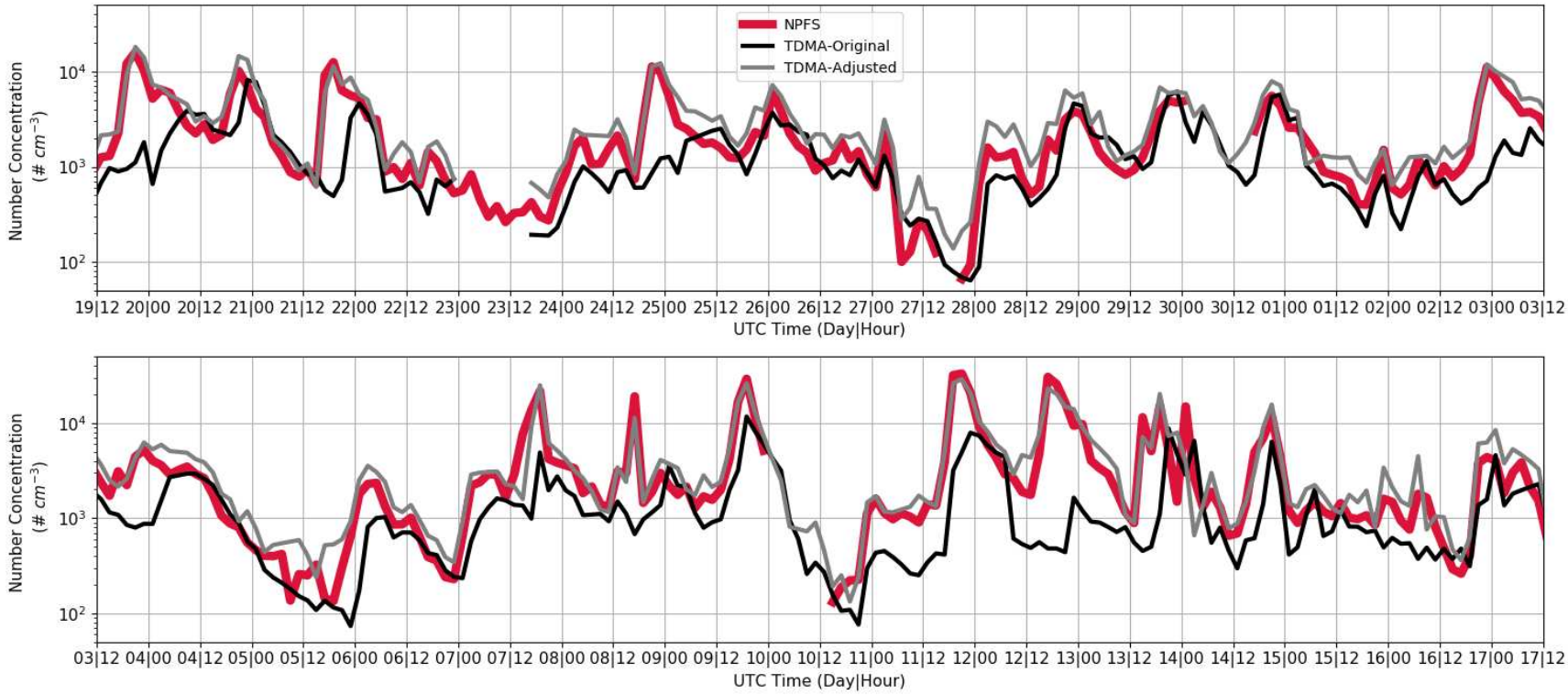

Figure A1.3. Time series of the integrated aerosol number concentrations between 7 and 30 nm in the New Particle Formation Study (red) and the SMPS+APS size distributions both before the adjustments (Original, black) and after the adjustments (Adjusted, grey). The dates included were 19 Apr. 2013 through 17 May 2013.

APPENDIX 2: ANALYSIS OF THE UNCERTAINTIES ASSOCIATED WITH DRAG FORCES ON THE C^{3}LOUD-EX UPDRAFT ESTIMATES

$\epsilon_{w,upd-drag}$ is the uncertainty in the w_{air} estimate arising from changes in the drag force on the radiosonde system within an updraft as compared to still air conditions. Because radiosonde systems typically reach their terminal velocity within a couple of seconds and are often close to terminal-velocity balance, we can use the formula for the terminal velocity and its dependence on the drag coefficient (C_D) to estimate the uncertainty.

The terminal velocity (v_T) of the radiosonde system can be determined as follows (following, e.g., Wang et al. 2009; Gallice et al. 2011):

$$v_T = \sqrt{\frac{2g(net\_free\_lift)}{\rho C_D A}} \tag{A2.1}$$

In Eq. A2.1, net free lift (units of kg), when multiplied by acceleration due to gravity g ~ 9.81 m s^{-2}, is the upward buoyant force acting on the radiosonde system. Net free lift is calculated as the difference of two quantities: (1) the mass measured when the helium-filled balloon is attached to a spring scale (typical value of 1.03 kg; range from 0.86 kg to 1.40 kg); and (2) the combined mass of the radiosonde and dereeler attached to the balloon (0.24 kg). These measurements were taken during the clear-sky, still-air launches described in Section 3.2a. The other variables in Eq. A2.1 include the ambient air density ρ, the drag coefficient C_D, and balloon cross-sectional area A. The helium inside the balloon is assumed to expand adiabatically as the balloon rises. The initial A of the balloon is approximately 1.33 m^2, obtained from the clear-sky, still-air launches. Based on prior laboratory studies using perfect spheres (Achenbach 1972; Son et al. 2010) and on radiosonde observations during relatively calm, nighttime conditions (Gallice et al. 2011), drag coefficients for tropospheric conditions generally fall between 0.2 and 0.5. The drag

coefficient within a supercell updraft may fall outside of this range, but we have no way of knowing whether this is the case due to the lack of observations. Using the known range of tropospheric drag coefficients from relatively calm conditions and using a range of tropospheric air densities, we can estimate the uncertainty of v_T, and thus w_{air}, due to variations in C_D based on Equation A2.1 (Fig. A2.1). The range of v_T as a function of air density (gold line) is at most 3.1 m s^{-1}, which occurs at the lowest density included (0.3 kg m^{-3} , representative of the upper troposphere). Therefore, we estimate that $\epsilon_{w,upd-drag}$ is ± 1.6 m s^{-1}, which is half of the maximum range (3.1 m s^{-1}).

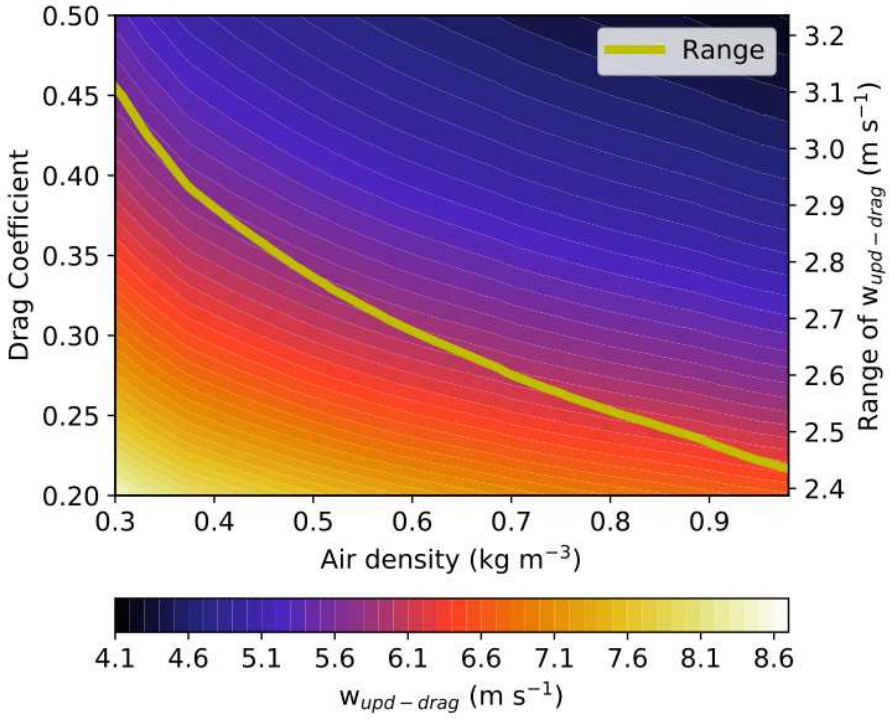

Figure A2.1. Terminal velocity calculations (m s^{-1}) for ascending C^3LOUD-Ex radiosondes with varying drag coefficients and densities (shaded, left axis) and the range (maximum minus minimum) of terminal velocities for each density.

APPENDIX 3: ACPC MIP MODEL DETAILS

We present the details and the associated references for the models that participated in the ACPC MIP and the parameterizations that they used for these simulations in Table A3.1.

Table A3.1. Details and references for the varying physical parameterizations and simulation differences between the models that participated in the ACPC MIP.

Model Abbreviation	Microphysics	Hydrometeors	Calculation of Hydrometeor Fall Speeds	Saturation Adjustment?	Aerosol Activation	Aerosol Processes	Heterogenous Ice Nucleation
COSMO	2M: Seifert and Beheng (2006a), Seifert et al. (2012)	c, r, g, h, s, i; (2M in all hydrometeors)	Number and mass weighted mean fall speeds, assuming different DSDs and power laws for different hydrometeors	Yes	Based on COSMO-ART3.1: Vogel et al. (2009)	N/A (domain-wide, temporally constant aerosol profile)	Phillips et al. (2008)
MesoNH	2M, LIMA: Vié et al. (2016)	c, r, g, s, i (2M in c, r, i)	Fall speed-diameter power law, different for each hydrometeor type	Yes	Based on the Köhler theory with a diagnostic of the maximum supersaturation.	Aerosol transport (resolved & sub-grid), activation, regeneration through droplets evaporation	Meyers et al. (1992)
RAMS	2M, RAMS: Meyers et al. (1997), Saleeby and Cotton (2004)	c, d, r, g, h, a, s, i (2M in all hydrometeors)	Fall speed of hydrometeors depends on size (smaller particles fall slower; larger particles fall faster)	No	Aerosol activation via bin parcel model look-up table: Saleeby and Cotton (2004)	Aerosol advection, dry deposition, wet deposition, regeneration from evaporated/sublimated hydrometeors: Saleeby et al. (2013)	DeMott (2010), particles greater than 500 nm
UM	2M, CASIM: Shipway and Hill, (2012), Hill et al. (2015), Grosvenor et al. (2017), Miltenberger et al. (2018)	c, r, g, s, i (2M in all hydrometeors)	Fall speed-diameter relation, different for each hydrometeor type (see Tab. 2, Miltenberger et al. 2018, except for graupel which is 500*pi/6)	Yes	Shipway (2015)	Aerosol transport (resolved & subgrid), considered in activation (but not depleted)	Meyers et al. (1992)
NU-WRF	2M, P3: Morrison and Milbrandt (2015)	c, r, ix1,; (2M in c, r, i; i has explicit rime ice mass and density, this is single ice version)	Droplet and rain drops depends on size, ice depends on mass dimension: Heymsfield et al. 2007, Morrison and Milbrandt 2015	No	Abdul-Razzak and Ghan (2000) using minimum supersaturation from Morrison and Grabowski (2008, their Eq. A10)	Aerosol transport (resolved & sub-grid)activation, removal by droplet coalescence, regeneration from droplet evaporation: Fridlind et al. (2017)	Cooper (1986)
WRF-Morr	2M Morrison: Morrison et al. (2005), Morrison et al. (2009)	c, r, h, s, i; (2M in all hydrometeors)	Droplet and rain drops depends on size, ice depends on mass dimension: Heymsfield et al. 2007	Yes	Abdul-Razzak and Ghan (2000)	N/A (domain-wide, temporally constant aerosol profile)	Cooper (1986), Rasmussen et al. (2002)
WRF-SBM	SBM: Khain et al. (2004), Shpund et al. (2019)	c, r, h, s, i; (explicitly calculates mass and number of particles in each bin)	Fall speed of hydrometeors depends on types and size	No	Based on the Köhler theory	Aerosol is prognostic with advection, activation, and regeneration considered: Shpund et al. (2019)	Deposition freezing: Meyers et al. (1992); Heterogenous and homogeneous drop freezing: Bigg (1953)

Table A3.1. Continued.

Model Abbreviation	Model version	Grid	Vertical Coordinate	Land Surface	Boundary Layer / Turbulence	Radiation	Init. / Boundary Conditions Dataset
COSMO	v5.1: Schättler et al. (2016)	Arakawa-C	Terrain-following height coordinate: Gal-Chen and Sommerville (1975)	TERRA: Heise et al. (2006)	3-D Smagorinsky-Lilly closure: Langhans et al. (2012)	Ritter and Geleyn (1992)	NCEP Global Data Assimilation System (GDAS)/FNL
MesoNH	v5.4.1: Lac et al. (2018)	Arakawa-C	Terrain-following height coordinate: Gal-Chen and Sommerville (1975)	SURFEX: Masson et al. (2013)	3D (1D in the low-res domain) turbulence scheme using a prognostic TKE and a mixing-length closure: Cuxart et al. (2000)	SW: Fouquart and Bonnel (1980); LW, RRTM: Iacono et al. (2008)	ECMWF real-time forecasting system
RAMS	v6.2.09: Cotton et al. (2003), Saleeby and van den Heever (2013)	Arakawa-C	Terrain-following sigma-Z coordinate	LEAF-3: Walko et al. (2000)	3D deformation K: Smagorinsky (1963)	Two-stream: Harrington (1997)	NCEP Global Data Assimilation System (GDAS)/FNL
UM	v.10.8: Walters et al. (2017)	Arakawa-C	Charney-Phillips grid, terrain-following close to surface	JULES: Best et al. (2011), Clark et al. (2011)	Blended boundary layer scheme: Lock et al.(2015) and a 3D Smagorinsky-type turbulence scheme: Halliwell (2015), Stratton et al. (2015)	SOCRATES: based on Edwards and Slingo (1996)	ERA interim reanalysis data at a resolution of 0.6 degrees
NU-WRF	WRF ARW v3.9.1: Skamarock et al. (2008)	Arakawa-C	Terrain-following eta pressure coordinate	Noah-MP land-surface model: Chen and Dudhia (2001)	MYNN 2.5 level TKE scheme	Goddard radiation 2017: Matsui et al. (2018)	NCEP Global Data Assimilation System (GDAS)/FNL
WRF-Morr	WRF ARW v3.7.1: Skamarock et al. (2008)	Arakawa-C	Terrain-following eta pressure coordinate	Noah-MP land-surface model: Chen and Dudhia (2001)	YSU: Hong et al. (2006)	RRTMG scheme, SW & LW: Iacono et al. (2008)	NCEP Global Data Assimilation System (GDAS)/FNL
WRF-SBM	WRF ARW v4.0.3: Skamarock et al. (2008)	Arakawa-C	Terrain-following eta pressure coordinate	Noah-MP land-surface model: Chen and Dudhia (2001)	YSU: Hong et al. (2006)	RRTMG scheme, SW & LW: Iacono et al. (2008)	NCEP Global Data Assimilation System (GDAS)/FNL

APPENDIX 4: ACPC MIP BASE STATE CALCULATIONS

The terms of Eq. 4.1 are calculated from each model's output on their native grids and at the center of each model grid box. In some instances, variables are interpolated by ½ of the model grid spacing in either the x, y, or z direction in order to calculate each term's value at the center of the grid box. Similarly, *w*, which is prognosed at the top and bottom faces of a model grid box, is interpolated to the center of each model grid box, such that the analyses presented in this study all occur at the center of each model grid box.

Because all the models calculate their base states differently, we make the same approximation for the base state for each model's data to allow for more comparable results. This base state is calculated as follows. At each model output time, all non-cloudy model grid points and their respective model altitudes are collected. A 5^{th} order polynomial function, with altitude being the independent variable, is then fitted to this data using least squares regression to estimate the base state. A 5^{th} order polynomial was used because it best captured the shape of the base state profiles from the range of functions that were tested.